Materials Research Center
Lehigh University

Fourth Interim Report

NANOSTRUCTURE AND DEFECT CHEMISTRY OF RELAXOR FERROELECTRICS

SPONSORED BY:

OFFICE OF NAVAL RESEARCH

Period: August 1, 1986 - July 31, 1988

PREPARED BY:

Professor M. P. Harmer

Professor D. M. Smyth

Materials Research Center #32

Lehigh University

Bethlehem, PA   18015

DTIC
ELECTE
APR 26 1989
S E D

89 3 29 003

SECURITY CLASSIFICATION OF THIS PAGE

REPORT DOCUMENTATION PAGE

1a. REPORT SECURITY CLASSIFICATION Unclassified	1b. RESTRICTIVE MARKINGS
2a. SECURITY CLASSIFICATION AUTHORITY	3. DISTRIBUTION/AVAILABILITY OF REPORT
2b. DECLASSIFICATION/DOWNGRADING SCHEDULE	

4. PERFORMING ORGANIZATION REPORT NUMBER(S)	5. MONITORING ORGANIZATION REPORT NUMBER(S)

6a. NAME OF PERFORMING ORGANIZATION Lehigh University	6b. OFFICE SYMBOL (If applicable)	7a. NAME OF MONITORING ORGANIZATION

6c. ADDRESS (City, State and ZIP Code) Materials Research Center #32 Bethlehem, PA 18015	7b. ADDRESS (City, State and ZIP Code)

8a. NAME OF FUNDING/SPONSORING ORGANIZATION Office of Naval Research	8b. OFFICE SYMBOL (If applicable)	9. PROCUREMENT INSTRUMENT IDENTIFICATION NUMBER

8c. ADDRESS (City, State and ZIP Code) Division of Materials Research Arlington, VA 22217	10. SOURCE OF FUNDING NOS.			
	PROGRAM ELEMENT NO.	PROJECT NO.	TASK NO.	WORK UNIT NO.

11. TITLE (Include Security Classification) Nanostructure and Defect Chemistry of Relaxor Ferroelectrics

12. PERSONAL AUTHOR(S)
Professors Martin P. Harmer and Donald M. Smyth

13a. TYPE OF REPORT Interim	13b. TIME COVERED FROM 8/1/86 TO 7/31/88	14. DATE OF REPORT (Yr., Mo., Day)	15. PAGE COUNT

16. SUPPLEMENTARY NOTATION

17.	COSATI CODES		18. SUBJECT TERMS (Continue on reverse if necessary and identify by block number)
FIELD	GROUP	SUB. GR.	

19. ABSTRACT (Continue on reverse if necessary and identify by block number)

This report describes an investigation of the microstructure, microchemistry, and dielectric properties of relaxor ferroelectrics and structurally related compounds. The emphasis has been on the use of transmission electron microscopy to correlate changes in the composition and processing conditions with changes in microstructure and properties. The report is in three parts that deal with 1) cation-ordering and microchemical domains in $Pb(Sc_{1/2}Ta_{1/2})O_3$ (PST), undoped and La/Na-doped $Pb(Mg_{1/3}Nb_{2/3})O_3$ (PMN) and $Ba(Zn_{1/3}Nb_{2/3})O_3$ (BZN), 2) micro-polar domains in normal ferroelectrics ($BaTiO_3$) and relaxor ferroelectrics (PMN:PT and PZN:PT), and 3) the effect of a pyrochlore second phase on the dielectric properties of PMN.

Lead Oxides, Magnesium, Niobium, Tantalum, Scandium, (Tungsten) Barium Titanates, Zinc.

20. DISTRIBUTION/AVAILABILITY OF ABSTRACT UNCLASSIFIED/UNLIMITED ☒ SAME AS RPT. ☐ DTIC USERS ☐	21. ABSTRACT SECURITY CLASSIFICATION Unclassified	
22a. NAME OF RESPONSIBLE INDIVIDUAL	22b. TELEPHONE NUMBER (Include Area Code)	22c. OFFICE SYMBOL

DD FORM 1473, 83 APR   EDITION OF 1 JAN 73 IS OBSOLETE.

SECURITY CLASSIFICATION OF THIS PAGE

TITLE: NANOSTRUCTURE AND DEFECT CHEMISTRY OF RELAXOR FERROELECTRICS

ABSTRACT

This report describes an investigation of the microstructure, microchemistry and dielectric properties of relaxor ferroelectrics and structurally related compounds. The emphasis has been on the use of transmission electron microscopy to correlate changes in the composition and processing conditions with changes in microstructure and properties. The report is in three parts that deal with 1) cation-ordering and microchemical domains in $Pb(Sc_{1/2}Ta_{1/2})O_3$ (PST), undoped and La/Na-doped $Pb(Mg_{1/3}Nb_{2/3})O_3$ (PMN) and $Ba(Zn_{1/3}Nb_{2/3})O_3$ (BZN), 2) micro-polar domains in normal ferroelectrics ($BaTiO_3$) and relaxor ferroelectrics (PMN:PT and PZN:PT), and 3) the effect of a pyrochlore second phase on the dielectric properties of PMN.
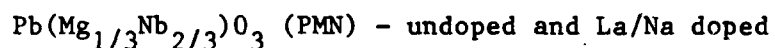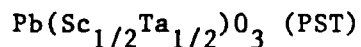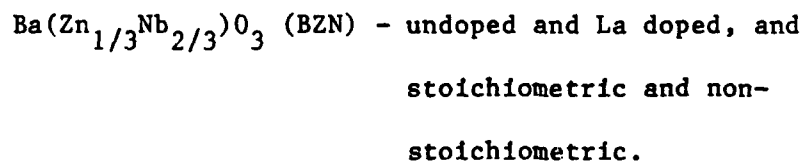
1

I. INTRODUCTION

This report, which represents Part II of a two part sequence, will deal primarily with research related to the structure and properties of relaxor ferroelectrics. The emphasis is on the use of transmission electron microscopy as a characterization tool and on the correlation between chemical composition and processing with changes in microstructure and dielectric properties. The report takes the form of three independent sections. A brief summary of each of the three sections is as follows:

1. Microchemical Domains and Ordering in Relaxor Ferroelectrics

This section describes the results of transmission electron microscopy studies of microchemical domains in the following two lead-based ferroelectric relaxor systems:

$Pb(Sc_{1/2}Ta_{1/2})O_3$ (PST)

$Pb(Mg_{1/3}Nb_{2/3})O_3$ (PMN) - undoped and La/Na doped

and the following none-lead based system:

$Ba(Zn_{1/3}Nb_{2/3})O_3$ (BZN) - undoped and La doped, and stoichiometric and non-stoichiometric.

In PST, we were the first to directly observe ordered microdomains by high resolution dark field imaging. The size range of the ordered domains was 10-400nm depending on the annealing treatment and whether the sample was single crystal or polycrystal. These results were in

general agreement with the size range predicted on the basis of x-ray measurements by Setter and Cross.

$Pb(Mg_{1/3}Nb_{2/3})O_3$ was found to exhibit short-range 1:1 ordering of the Mg^{2+} and Nb^{5+} ions on the B-site sublattice. In undoped PMN the ordered microdomains were 2-5nm in size, as observed by high resolution dark field imaging. The degree of ordering could not be controlled by heat treatment. A new ordering model was proposed in which compositional segregation of the B-site constituents occurs on a nanometer scale, with the ordered domains having a $Mg^{2+}:Nb^{5+}$ ratio closer to 1:1, thus requiring the disordered matrix to be correspondingly richer in Nb^{5+}.

In order to further illucidate the ordering mechanism, studies were conducted on La- and Na-doped compositions. Donor doping with La_2O_3 compensated for the charge imbalance resulting from the short range order, and thus enhanced the degree of ordering. Fully *ordered* structures were obtained with sufficiently high levels of La doping. Acceptor doping with Na_2O accentuated the charging problem, and hence suppressed the degree of ordering. Both the degree of B-site ordering in PMN, and the second phases present in its microstructure, could be precisely controlled and predicted on the basis of its starting chemical composition. It was proposed that the tendency to 1:1 order in $Pb(B_{1/3}Nb_{2/3})O_3$ relaxor ferroelectrics is directly related to the stability of the pyrochlore structure with respect to perovskite.

Microchemical ordering was more complex in $Ba(Zn_{1/3}Nb_{2/3})$ (BZN) in comparison to PMN. Stoichiometric BZN was found to contain a mixture of 1:1 and 1:2 short range ordered domains. The 1:1 type ordered domains were 2-4nm in size and did not grow under heat treatment, but could be made to grow by La-doping. However, the 1:2 type ordered domains did

grow during thermal annealing which was taken to suggest that the 1:2 ordered domains had the same chemical composition as the bulk (a major distinction between the 1:1 and 1:2 type ordered domains). The relative proportion of 1:1 versus 1:2 type ordering varied systematically as a function of the Zn/Nb ratio. Increasing the Zn/Nb ratio promoted the formation of the 1:1 type ordered phase, whereas decreasing the Zn/Nb ratio promoted the formation of the 1:2 type ordered phase. High temperature annealing caused Zn to be lost preferentially from the grain boundaries by diffusion and evaporation. The Zn deficiency in the grain boundaries promoted a 1:2 type ordering preferentially along the grain boundary region.

2. Ferroelectric Domains in Normal and Relaxor Ferroelectrics

Scanning electron microscopy (SEM) and/or transmission electron microscopy (TEM) has been used to characterize the domain configurations in the following systems:

$$BaTiO_3 - Ca/Nb \text{ doped}$$

$$Pb(Mg_{1/3}Nb_{2/3})O_3:PbTiO_3$$

$$Pb(Zn_{1/3}Nb_{2/3})O_3:PbTiO_3$$
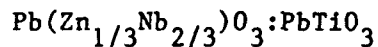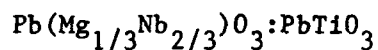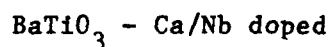
In the work on Ca- and Nb-doped $BaTiO_3$ we were able to confirm, for the first time, the existence of a new type of 90-degree domain boundary configuration. The newly identified 90-degree boundary is heavily distorted, carrying an electrostatic charge (i.e. it is not the usual head-meets-tail arrangement). The new boundary was identified by three independent methods, (1) SEM studies of domain etch patterns, (2) selected area electron diffraction by TEM, and (3) kikuchi pattern analysis across individual domains by TEM. We have also made direct

4

measurement of the width of a conventional 90-degree domain boundary in
BaTiO$_3$. Atomic resolution transmission electron microscopy was used to
directly observe the bending of the (100) planes across a 90-degree
boundary. The estimated width was several tens of unit cell lengths.

In pure PMN (single crystal and polycrystal) no ferroelectric domains
were observed at room temperature or -185°C. In PMN:10%PT (single
crystal and polycrystal) no domains were observed at room temperature,
however, faint domain walls were observed at -120°C and below. The
domain configurations observed were consistent with those expected for
rhombohedral symmetry. For PZN:10%PT (single crystal only) very narrow,
i.e. 10 nm wide, ferroelectric rhombohedral domains were visible at room
temperature and below. The smaller domain width observed in PZN:PT (10
nm) compared to that observed in BaTiO$_3$ (> 100 nm) can be explained in
terms of the difference in spontaneous strain at the phase transition.
In BaTiO$_3$, the spontaneous strain is much larger than that for PZN (or
PMN).

3. Effect of Powder Purity and Pyrochlore Phase on the Dielectric Properties of PMN

We have previously discovered two important facts about the
factors influencing the dielectric constant of PbMg$_{1/3}$Nb$_{2/3}$O$_3$ (PMN).
First we, have shown that the dielectric constant of PMN can be
increased dramatically by improving the purity of the starting powders.
Second, we have shown that pyrochlore usually forms as a descrete second
phase in the microstructure and, therefore, it should not (in small
quantities at least) have a devastating effect on the dielectric
constant of PMN.

5

The above results led us to study the effect of common background impurities (such as Al_2O_3 and ZrO_2) on the dielectric constant of PMN. Much to our surprise we found that very small additions (0.2 wt%) of Al_2O_3 and other common impurities such as ZrO_2, Ag and SiO_2 had a devastating effect on the dielectric constant of PMN. For example, 0.2 wt% Al_2O_3 was found to decrease the maximum value of the dielectric constant of PMN from 20,000 to 7,000. This is an important finding given that Al_2O_3 and ZrO_2 are often used as grinding balls in the manufacture of PMN powders, which makes them common contaminants. We are currently in the process of characterizing the microstructures of these materials to determine the cause of this troublesome effect.

AWARDS RELATED TO THIS RESEARCH

1. Ceramographic contest, American Ceramic Society, Pittsburgh, 1984.

    First prize, "Determination of Calcium Site Occupancy in $BaTiO_3$ by ALCHEMI", M. P. Harmer, H. Chan, and D. M. Smyth.

2. Ceramographic contest, American Ceramic Society, Cincinnati, 1985.

    Scanning Electron Microscopy: Second prize, "Ferroelectric Domain Configurations in $BaTiO_3$", Y. H. Hu, X. Wang, M. P. Harmer, and D. M. Smyth.

    Transmission Electron Microscopy: Third prize, "Ordered Microdomains in PST", H. M. Chan, M. P. Harmer, A. Bhalla, and L. E. Cross.

3. Rowland B. Snow award by the American Ceramic Society for the most outstanding ceramographic exhibit in 1986.

4. Ceramographic contest, American Ceramic Society, Chicago, 1986.

    First prize and best of show, "Ferroelectric Domain Boundaries in $BaTiO_3$", H. M. Chan, S. Horvath, M. P. Harmer.

    Second prize, "In-situ Observations of Ferroelectric Domain Motions in $BaTiO_3$", Z. Wang, H. M. Chan, M. P. Harmer.

    Third prize, "Wavy Grain Boundaries and Fracture Modes in $Sr_2Fe_2O_5$", E. Chang, Z. Wang, M. P. Harmer, and D. M. Smyth.

5. Ceramographic contest, American Ceramic Society, Pittsburgh, 1987.

    Scanning Electron Microscope: Third prize, "Octahedral Pyrochlore Grains in $Pb(Mg_{1/3}Mb_{2/3})O_3$"

RELATED PUBLICATIONS

1. M. P. Harmer, A. Bhalla, B. Fox, and L. E. Cross, "Electron Microscopy of Ordered Domains in Lead Scandium Tantalate $Pb(Sc_{0.5}Ta_{0.5})O_3$", Mat. Lett., 2(4a), 278 (1984).

2. N. Stenton and M. P. Harmer, "Electron Microscopy Studies of a $SrTiO_3$ Boundary Layer Material", Adv. in Ceramics, 7, 156 (1984).

3. H. Chan, M. P. Harmer, A. Bhalla, and L. E. Cross, "TEM of the Relaxor Material $Pb(Sc_{1/3}Ta_{1/2})O_3$", Jap. Journ. Appl. Phys., 24, Supplement 24-2, 550-552, 1985.

4. Y. H. Hu, H. M. Chan, X. Zhang, and M. P. Harmer, "Scanning Electron Microscopy and Transmission Electron Microscopy of Ferroelectric Domains in Doped $BaTiO_3$", J. Am. Ceram. Soc., 69, 594-602, 1986.

5. A. J. Gorton, J. Chen, H. M. Chan, D. M. Smyth, M. P. Harmer, and I. Burn, "Microstructure and Properties in PMN Ceramics - Influence of Powder Purity", Proc. Sixth IEEE Int. Symp. on Application of Ferroelectrics, pp. 150-152, 1986.

6. J. Chen, A. J. Gorton, H. M. Chan, and M. P. Harmer, "Effect of Powder Purity and Second Phases on the Dielectric Properties of Lead Magnesium Niobate Ceramics", J. Am. Ceram. Soc., 69, C-303, 1986.

7. H. M. Chan, S. F. Horvath, and M. P. Harmer, "HRTEM of Ferroelectric Domains in Nb-doped $BaTiO_3$", Bull. Am. Ceram. Soc., 65, 1134 (1986).

8. J. Chen, H. M. Chan, and M. P. Harmer, "Microstructure and Ordering in Undoped, Na-doped and La-doped $Pb(Mg_{1/3}Nb_{2/3})O_3$", accepted for publication in J. Ceram. Soc.

9. Z. Q. Zhuang, M. P. Harmer, D. M. Smyth, and R. E. Newnham, "The Effect of Octahedrally-Coordinated Calcium on the Ferroelectric Transition of $BaTiO_3$", Mat. Res. Bul., Vol. 22, pp. 1329-1335, 1987.

10. H. M. Chan and M. P. Harmer, "Microstructures of High Dielectric Constant Materials", in Ceramic Microstructures '86, Eds. J. Pask and A. G. Evans, Plenum, pp. 739-748, (1988).

8

RELATED PRESENTATIONS

1. May 5, 1985, "TEM of the Relaxor Material $Pb(Sc_{0.5}-Ta_{0.5})$", H. Chan, M. P. Harmer, A. Bhalla, and L. E. Cross, Annual meeting of Am. Ceram. Soc., Cincinnati, OH.

2. April, 1986, "Processing, Microstructure and Properties of the Relaxor Materials $Pb(Mg_{1/3}Nb_{2/3})$:$PbTiO_3$ and $Pb(Mg_{1/2}W_{1/2})O_3$:$PbTiO_3$", H. M. Chan, A. Gorton, C. Jie, D. M. Smyth, and M. P. Harmer nad I. Burn, E. I. DuPont, Wilmington, DE, Annual meeting of Am. Ceram. Soc., Chicago, IL.

3. April, 1986, "Transmission Electron Microscopy of Undoped and Mn-Doped Lead Magnesium Niobate:Lead Titanate, $Pb(Mg_{1/3}Nb_{2/3})O_3$:$PBTIO_3$ Relaxor Ferroelectrics", H. M. Chan and M. P. Harmer, Lehigh University and A. Bhalla and L. E. Cross, Pennsylvania State University, Annual meeting of Am. Ceram. Soc., Chicago, IL.

4. May, 1986, "Relaxor Ferroelectrics", M. P. Harmer, AMP Inc., Harrisburg, PA.

5. June, 1986, "Microstructure and Properties of PMN Ceramics-- Influence of Powder Purity", A. J. Gorton, J. Chen, H. M. Chan, D. M. Smyth, M. P. Harmer, and I. Burn, Int. Sym. on the Appl. of Ferroelectrics (ISAF), Lehigh University.

6. June, 1986, "Microstructure and Microchemistry of Relaxor Ferroelectrics", H. M. Chan and M. P. Harmer, Int. Sym. on the Appl. of Ferroelectrics (ISAF), Lehigh University.

7. June, 1986, "The Effect of Octahedrally-Coordinated Calcium on the Ferroelectric Transition in $BaTiO_2$", Z. Q. Zhuang, M. P. Harmer, D. M. Smyth, and R. E. Newnham, Int. Sym. on the Appl. of Ferroelectrics (ISAF), Lehigh University.

8. July, 1986, "Microstructures of High Dielectric Constant Materials", H. M. Chan and M. P. Harmer, Ceramic Microstructures '86, Berkeley, CA.

9. October, 1986, "Microstructure of Relaxor Ferroelectrics", M. P. Harmer, Pennsylvania State University, University Park, PA.

10. November, 1986, "Microstructure and Nanostructure of Relaxor Ferroelectrics", M. P. Harmer, U.S.-Japan Joint Seminar on Dielectric and Piezoelectric Ceramics, Toyama, Japan.

11. November, 1986, "Ferroelectric Ceramics as Seen with the Electron Microscope", M. P. Harmer, Fine Ceramics Association of Japan, Tokyo, Japan.

12. December 19, 1986, "Preparation, Microstructure and Properties of Relaxor Ferroelectrics", M. P. Harmer, E. I. DuPont, Wilmington, DE.

13. April, 1987, "Forced Ordering in Lanthanum-Doped Lead Magnesium Niobate", J. Chen, M. P. Harmer, and H. M. Chan, Annual meeting of Am. Ceram. Soc., Pittsburgh, PA.

14. April, 1987, "Order and Disorder in $Ba(Zn_{1/3}Nb_{2/3}O_3$", P. Peng, M. P. Harmer, and D. M. Smyth, a poster, 89th Annual meeting, Am. Ceram. Soc., Pittsburgh, PA.

15. July, 1987, "Microstructure and Properties of Relaxor Ferroelectrics", M. P. Harmer, IBM, Inc., Yorktown, NY

16. August, 1987, "Microstructure of Interfaces in Ceramic Dielectrics", M. P. Harmer, Gordon Research Conference on Solid State Studies, Plymouth, New Hampshire.

17. September, 1987, "Microstructure and Microchemistry of Relaxor Ferroelectrics", M. P. Harmer, U.S.-China Joint Seminar, Washington, D.C.

18. November, 1987, "Electron Microscopy of Ferroelectric Ceramics", M. P. Harmer, Columbia University.

19. March, 1988, "Microstrucutre of Relaxor Ferroelectrics", M. P. Harmer, CSIRO, Melbourne, Australia.

20. May 5, 1988, "Ferroelectric-Paraelectric Transition in $BaTiO_3$ Co-doped with Zn and Nb", P. Peng, M. P. Harmer, and D. M. Smyth, 90th Annual meeting, Am. Ceram. Soc., Cincinnati, OH.

21. June, 1988, "Microstructure and Microchemistry of Relaxor Ferroelectrics, M. P. Harmer, Xian Jiaotong Univ., Xian, China.

22. June, 1988, "Transmission Electron Microscopy of Relaxor Ferroelectrics", M. P. Harmer, Beijing Univ., China.

Section I

MICROCHEMICAL DOMAINS AND ORDERING IN RELAXOR FERROELECTRICS

Section II

FERROELECTRIC DOMAINS

Section III

SECOND PHASE DISTRIBUTION IN RELAXOR FERROELECTRICS

Section I

MICROCHEMICAL DOMAINS AND ORDERING IN RELAXOR FERROELECTRICS

ORDERING STRUCTURE AND DIELECTRIC PROPERTIES OF

UNDOPED AND La/Na DOPED Pb(Mg$_{1/3}$Nb$_{2/3}$)O$_3$[*]

Jie Chen, Helen M. Chan[#] and Martin P. Harmer[#]

Department of Materials Science & Engineering
Lehigh University, Bethlehem PA

ABSTRACT

Transmission electron microscopy was used to study the ordered domain structures in undoped and La/Na doped Pb(Mg$_{1/3}$Nb$_{2/3}$)O$_3$ (PMN), (where the compositions of the doped samples were specifically chosen so as to elucidate the ordering mechanism). The results showed that the Mg^{2+} ions and Nb^{5+} ions are short range ordered on the B-site sub-lattice in undoped PMN, with a domain size of 2 - 5 nm. This short-range ordering gives rise to B-site composition fluctuations occurring on a nanometer scale, and it is this compositional inhomogeneity which is believed to be responsible for the diffuse phase transition behavior. Donor doping with La$_2$O$_3$ can compensate for the local charge imbalance resulting from the short range order, and thus enhances the degree of ordering. Acceptor doping with Na$_2$O, however, increases the charge effect, and hence ordering is suppressed. The effect of Na-doping and La-doping on the dielectric properties of PMN is also discussed.

INTRODUCTION

The ferroelectric relaxor material lead magnesium niobate ($Pb(Mg_{1/3}Nb_{2/3})O_3$ or PMN) was first synthesized by Soviet workers in the late 1950's [1]. Since this time, PMN has been extensively studied due to its high dielectric constant, and high electrostrictive coefficient [2-6]. Relaxor ferroelectrics are characterized by diffuse phase transitions (DPT), i.e. they exhibit a broad Curie peak in the ferroelectric-paraelectric phase transition range. The positions of the maxima in the dielectric constant (and loss factor) curves versus temperature, are frequency dependent in the radio frequency range, and are shifted towards higher temperatures as the frequency is increased.

It has been suggested [7-9] that the lead-base materials which exhibit a diffuse phase transition can be viewed as having composition fluctuations on a microscopic scale. Because more than one type of ion can occupy the same crystallographic position, a random or near random distribution of ions gives rise to microvolumes (Kanzig regions), where each region has a slightly different Curie temperature for the ferroelectric-paraelectric phase transition. The degree of diffuseness would thus be expected to depend upon the randomness of the compositional fluctuations. This was confirmed by Setter et. al.[10,11], who observed that in $Pb(Sc_{1/2}Ta_{1/2})O_3$ (PST), the phase transition does indeed sharpen when B-site cation ordering is increased by thermal treatment. In addition, transmission electron microscopy (TEM)

2

studies by Harmer et al. [12] and Chan et. al. [13], confirmed the existence of ordered domains in both single crystal and polycrystalline PST.

At room temperature, PMN has the cubic perovskite structure (space group Pm3m, a = 4.04Å) [14,2]. Although X-ray results [2] have not revealed any evidence of long-range ordering of Mg^{2+} and Nb^{5+} ions on the octahedral sites, evidence for short-range ordering has been obtained by several workers [15-18], in the form of diffuse superlattice reflections observed using selected-area electron diffraction. Chan et. al. [17] were able to utilise these reflections to image ordered regions which were 2-5 nm in size. In addition, preliminary work by Chan et al. [17] and Chen et.al. [18], revealed that doping with La on the Pb sites can force ordering in the B-site sublattice of PMN. Very little is known, however, about the type of order which occurs, and the influence (if any), on the dielectric properties.

The purpose of the present work, therefore, was to carry out a detailed study of the ordering mechanism in undoped and doped PMN using transmission electron microscopy. To this end, the La and Na doped PMN compositions studied were specifically chosen so as to elucidate the ordering arrangement of the Mg^{2+} and Nb^{5+} ions. By relating the dielectric properties to the domain structures, it was hoped to gain a better understanding of the microstructure/relaxor property relationships in PMN.

EXPERIMENTAL PROCEDURE

A summary of the compositions of the samples studied is given in Table-1. These were prepared using the precalcine procedure developed by Swartz et. al. [19], utilising high purity grade powders of PbO, MgO, Nb_2O_5, La_2O_3 and Na_2CO_3[1]. Details of the powder preparation techniques have been described in earlier work [20]. However calcining and sintering conditions specific to the compositions studied are outlined below. The powders were calcined between 850°C and 950°C for 4hrs, and cold pressed pellets were subsequently fired for 2hrs at either 1200°C (PMN and PNMN), or 1300°C (PLMN, PLMN-K and PLNMN). Firing was carried out inside a covered alumina crucible, and the pellets were covered with powder of the same composition to minimize the lead loss during sintering. Final relative densities in the range of 96 - 98% were achieved for all samples except PLMN-30%La, and the grain sizes were in the range of 3-6μm.

Polished sections were analyzed on an electron microprobe[2] and examined by a powder diffractometer[3] using Cu K_α radiation. Thin foil TEM specimens were prepared by hand polishing the samples down to 30-40μm and ion-beam thinning using 6kV argon ions incident at 13°-15° to the foil plane. To prevent Pb and Na loss during the thinning, a liquid-N_2 cooled cold stage was used. The thin foil specimens were examined in a electron microscope equipped with an energy-dispersive X-ray analyzer[4]. Dielectric permittivity and loss tangent under a weak ac field were measured

at frequencies between 100-100kHz, using a HP-4274A automatic capacitance bridge.

RESULTS AND DISCUSSION

1 Degree of order

(1) Undoped PMN:

As can be seen from Fig. 1a, superlattice reflections of the type $(h/2 \ k/2 \ 1/2)_S$ (h,k,1 odd) were obtained, thus indicating a doubling of the PMN unit cell dimension on ordering. Fig. 1b shows a centered dark-field (CDF) micrograph taken using the $(1/2 \ 1/2 \ 1/2)_S$ reflection; the bright (2-5 nm) regions are ordered domains, whereas the dark regions are the disordered matrix. Identical CDF images were obtained when imaging by different variants of the $(1/2 \ 1/2 \ 1/2)_S$ family of reflections. Since the $(1/2 \ 0 \ 0)_S$ and $(1/2 \ 1/2 \ 0)_S$ reflections were essentially absent, it is inferred that the lattice type in ordered PMN is face-centred cubic. By analogy with PST, the above results indicate that the structure of ordered PMN is of the general form $A(B'_{1/2}B''_{1/2})O_3$ [22]. The two most likely ordering models consistent with this ordering scheme are as follows:

Model 1:   B'-- Mg^{2+} and Nb^{5+} (disordered, 2:1 ratio)
                 B"-- Nb^{5+}

5

This type of ordering is equivalent to the $(NH_4)_3FeF_6$-type structure, and has been reported to occur in $Ba(W_{1/3}Sc_{2/3})O_3$ [21,22]. In this model, the ordered PMN structure can be represented as $Pb[(Mg_{2/3}Nb_{1/3})_{1/2}Nb_{1/2}]O_3$; thus the B" sites are occupied exclusively by Nb^{5+} ions, and the B' sites are occupied by a random mixture of the remaining Mg^{2+} and Nb^{5+} ions. Because the average composition of the ordered regions is identical to that of the bulk PMN, no charge imbalance exists within the ordered regions. For this reason, growth of the ordered domains would be expected to occur readily during heat treatment. This, however, was not observed to be the case; so that even after thermal treatment at $900^{\circ}C$ for 30hrs, the domain structure of the sample was unchanged. It follows, therefore, that domain growth is strongly inhibited in undoped PMN.

MODEL 2:   B'-- Mg^{2+}

B"-- Nb^{5+}
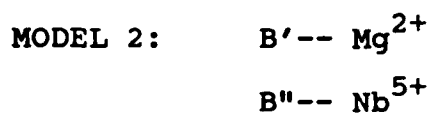
In this model, it is postulated that the Mg^{2+} and Nb^5 ions order in a 1:1 ratio on the B-site sublattice of PMN. This is directly analogous to the ordered PST structure as shown in Fig. 2. For this type of ordering, because the Mg/Nb ratio is 1:1 within the ordered domains, (as opposed to 1:2 for the average composition), strong charge effects will result, where the ordered regions will have a net negative charge with respect to the

6

matrix. This in turn, would be expected to severely inhibit domain growth, and indeed, this is what was observed. Since the ordered regions are Mg rich (relative to the average PMN composition), in order to preserve stoichiometry, the regions between the domains must be Nb rich. It follows that the ordered domains are in fact acceptor-type island regions (Mg/Nb>0.5), in a donor-type disordered matrix (Mg/Nb<0.5) (Fig. 3).

(2) La doped PMN (PLMN)

1) Mg/Nb ratio increased:

In order to further test which of the two models is correct, a series of samples was made up of the following compositions:

$$Pb_{1-x}La_x[Mg_{(1+x)/3}Nb_{(2-x)/3}]O_3 \qquad x = 0.05 - 0.30$$
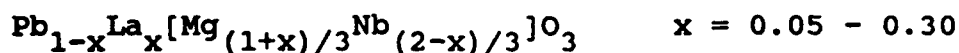
For these compositions, La^{3+} ions are substituted for Pb^{2+} ions on the A-site sublattice. Since La is trivalent whereas Pb is divalent, the La behaves as a donor dopant. In this series of samples, the compositions are adjusted so that compensation for the La is achieved by increasing the Mg:Nb ratio. Now let us consider how this will influence the ordering behavior. In the case of Model 1, since the Mg/Nb ratio in the ordered regions is the same as in the bulk, there is no charge imbalance resulting

7

from the ordering, thus La doping would not be expected to influence the degree of ordering. For Model 2 however, since the ordered regions are Mg rich, they can be considered to be acceptor doped. Thus donor doping with La would be expected to compensate the charge effects resulting from ordering, and hence favor an increased degree of order. As can be seen in the following discussion, enhanced ordering was indeed observed.

Transmission electron microscopy showed that the intensity of the $(1/2 \ 1/2 \ 1/2)_s$ superlattice reflection increased as the La^{3+} concentration increased, thus indicating an increased degree of order. In addition, centered dark field images revealed that the size of the ordered domains increased from 10-20nm to >500nm (see Fig. 4 and Table-2). (The wavy boundaries separating the ordered domains are anti-phase domain boundaries (APB's) [23].) Long range ordering was also confirmed by X-ray diffraction, with superlattice reflections becoming apparent for La concentration >10mol%. In accordance with the electron diffraction observations, the intensities of the superlattice peaks increased continuously with increasing La content (Fig. 5).

2) Mg/Nb ratio unchanged (PLMN-K):

$$Pb_{1-3x/2}La_x\square_{x/2}[Mg_{1/3}Nb_{2/3}]O_3 \qquad x = 0.03 - 0.20$$
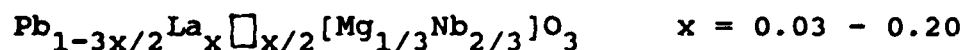
For this series of samples, the intention was to compensate for

the La doping by the introduction of lead vacancies, (a similar type of defect compensation scheme occurs in lead lanthanum zirconate-titanate (PLZT) ceramics [24]). Note that because of the presence of A-site vacancies, the A:B site occupancy ratio for these compositions is less than one.

Examination of the sintered microstructures using the TEM and electron microprobe revealed two types of second phase. These were identified as pyrochlore phase and magnesium niobate ($Mg_4Nb_2O_9$) (see Fig. 6). X-ray diffraction results showed that as the La concentration increased, the volume fraction of pyrochlore second phase increased also. In addition, the degree of order increased, as evidenced by the increasing intensity of the superlattice reflections. TEM revealed that the ordered domain structure of these specimens was identical to that of the PLMN compositions (where compensation was achieved by adjustment of the Mg/Nb ratio).

The explanation for this behavior is believed to be as follows. Firstly we can infer that lead vacancies are not a favorable defect species in this system, thus the system prefers to restore the A:B ratio by precipitating out magnesium niobate. Compensation for La^{3+} donor doping is subsequently achieved by adjusting the Mg/Nb ratio via formation of the pyrochlore phase, which is Nb rich.

In the 5 mol% La doped sample (PLMN-k, x = 0.05), isolated regions of coarse ordered domains were observed within the

short-range ordered regions (Fig.7). Chemical analysis using x-ray EDS showed that there was a higher La concentration and a higher Mg/Nb ratio in the more strongly ordered regions, compared with the short-range ordered matrix i.e.

$$\frac{[La]_{ordered}}{[La]_{matrix}} = 4.5 \qquad \frac{[Mg/Nb]_{ordered}}{[Mg/Nb]_{matrix}} = 1.27$$

These results, therefore, confirm on a local scale our general observations, namely that La doping together with an increase in the Mg:Nb ratio, enhances the degree of ordering.

(3) La and Na doped PMN (PLNMN)

$$Pb_{1-2x}La_xNa_x[Mg_{1/3}Nb_{2/3}]O_3 \qquad\qquad x = 0.1 - 0.2$$
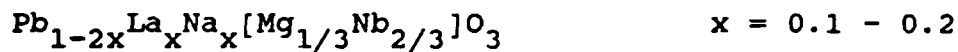
When both La and Na are doped into PMN such that the dopants both occupy the A-site, the La^{3+} and Na^+ are mutually compensating, thus the Mg:Nb ratio is maintained at 1:2. The resulting structure was very similar to that of undoped PMN shown in Fig. 1(a,b), i.e. the material showed short-range order, with a microdomain size of 2-5nm.

(4) Na doped PMN (PNMN)

10

$$Pb_{1-x}Na_x[Mg_{(1-x)/3}Nb_{(2+x)/3}]O_3 \qquad x = 0.05 - 0.1$$
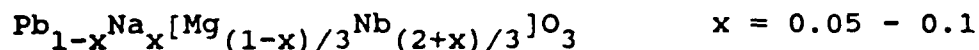
When PMN is Na-doped, the Na^+ ions occupy A-sites, hence Na acts as an acceptor dopant. It is thus necessary to compensate for the Na, and this was achieved by reducing the Mg:Nb ratio. It follows, therefore, that if model 2 is correct, sodium doping will increase the charge effects within the ordered domains (which are also acceptor-type), and thus decrease the degree of short-range ordering. For 5mol% Na doped PMN, $(1/2 \; 1/2 \; 1/2)_s$ reflections were still observed, but were significantly less intense relative to the corresponding superlattice reflections in undoped PMN. In 10mol% Na doped PMN, however, only very faint $(1/2 \; 1/2 \; 1/2)_s$ reflections were obtained, even after relatively long exposure times. The results confirm, therefore, that sodium doping does suppress ordering, which is again consistent with the predictions of model 2.

2 Dielectric Properties of Undoped and La/Na Doped PMN

The dielectric properties of PMN, PLMN and PNMN are shown in Fig. 8. The maximum value of the dielectric constant decreased rapidly with increasing La content, but the frequency dispersive behavior was still observed (Fig. 8, inset). Note also that La-doping decreases the Curie peak more strongly in comparison to Na-doping at the same dopant concentration. The dispersion data is summarized in Table-3, where ΔT_o is the temperature difference

11

separating the maxima in the dielectric constant plots measured at 100Hz and 100KHz respectively. It was found that the dispersion range first increases as the La concentration increases, and then decreases at the higher La contents. It has been shown that the dependence of the dielectric permittivity of DPT ferroelectrics above the Curie temperature differs from the Curie-Weiss Law, and instead obeys a quadratic law of the following form [6],

$$1/\varepsilon = 1/\varepsilon_m + (T-T_o)^2/(2\varepsilon_m \delta^2)$$

where ε is the dielectric constant, ε_m is the maximum value of ε, To is the temperature at which ε_m occurs, and δ is a parameter describing the diffuseness of the phase transition. Plotting $1/\varepsilon$ vs. $(T-T_o)^2$ shows that the low La and Na content PMN's (5% and 10%) still exhibit the quadratic dependence, but the higher La doped PMN's (PLMN-20%La and 30%La) and PLNMN show nonlinear relationships between $1/\varepsilon$ and $(T-T_o)^2$. Values of the parameter δ for the PLMN and PNMN are shown in Table-3. The value of δ for PMN was found to be 47°C, which is in agreement with the results of other workers [25,6].

As mentioned earlier, the dispersion range ΔT_o initially increases with increasing La content, but then decreases. Results from x-ray diffraction, however, have shown that the degree of ordering increases monotonically with increasing La content. Based on previous work on the PST system [11], which showed lesser

12

dispersion with greater B-site ordering, one might have expected the degree of dispersion (ΔT_o) to decrease steadily with increased B-site ordering in PLMN. The reason for the increase in ΔT_o from 5%La → 10%La is not clear. It could be related to possible local fluctuations in the La composition. This seems a plausible explanation, since (as can be seen from Fig. 8), the dielectric properties of PMN are very sensitive to La concentration. Another factor to consider is the A-site cation mixing present in PLMN which may also contribute towards a more diffuse phase transition. In $SrTiO_3$, bismuth substitutions on the A-sites have been shown to promote relaxor type behavior, i.e. $SrTiO_3$ doped more heavily with bismuth showed a more diffuse phase transition [26]. In the case of $SrTiO_3$ it was argued that bismuth influenced the basic mechanism of ferroelectricity and the same may be true for PLMN. However, the basic mechanism of ferroelectricity in relaxor materials is very complex and not properly understood. At higher La concentrations, it may be that the influence of B-site ordering predominates, hence the decrease in ΔT_o.

GENERAL

All the results obtained from the various doped PMN compositions are consistent with the following model. Namely that in lead magnesium niobate, the Mg^{2+} and Nb^{5+} ions are not randomly arranged on the B-site sublattice. Instead, it is believed that

13

these ions short-range order in a 1:1 ratio, giving rise to microdomains 2 - 5 nm in size. An important consequence of the ordered domains containing equal concentrations of Mg^{2+} and Nb^{5+}, is that the domains must be strongly charge imbalanced. Another way of considering this is that the ordered regions are Mg rich with respect to the average PMN composition, thus the disordered regions must be Nb rich. It is believed that it is these fine scale compositional inhomogeneities which are responsible for the DPT behavior in PMN. Long term annealing has no effect on the DPT behavior, since the domain growth is inhibited by electrostatic considerations.

What is not clear, however, is why $Pb(Mg_{1/3}Nb_{2/3})O_3$ favors a 1:1 short-range ordering, rather than a 1:2-type perfect ordering such as exhibited by $Ba(Mg_{1/3}Nb_{2/3})O_3$ and $Sr(Mg_{1/3}Nb_{2/3})O_3$. (This latter type of order can be described as a 1:2 ordered stacking arrangement of one B' occupied {111} type plane for every two B" occupied planes [22].) One possible explanation is that a smaller A-site ion size favors long range B-site ordering; hence the $Sr(B'_{1/3}B"_{2/3})O_3$ system shows a greater degree of ordering than the $Ba(B'_{1/3}B"_{2/3})O_3$ system [22]. The large polarizability of the lead ion may also influence ordering in lead-based systems, since 1:2 long range ordering has not been observed in any of these materials.

In addition, the relative size of the B' and B" ions is believed to play an important role. Thus a large size difference

in B' and B" ions favors ordering of the 1:1-type e.g. $Pb(Ni_{1/3}Nb_{2/3})O_3$ exhibits very faint superlattice reflections, hence the 1:1 ordering is much weaker than observed in PMN $(R_{Nb}<<R_{Ni}<R_{Mg}$ [27]). This dependence on the B'/B" size ratio is probably due to elastic energy considerations. Thus if a large size difference exists between the B' and B" ions, it is believed that the lattice strain is less for 1:1 ordering than for disordering or 1:2 ordering. The electrostatic energy, however, will increase on ordering, due to the charge imbalance between the ordered and disordered regions. Thus the observed nanometer scale ordering in these systems represents a balance between electrical and elastic strain energy considerations. In terms of ionic radii $R_{Ni}<R_{Mg}<R_{Zn}<R_{Cd}$ [27], thus $Pb(Ni_{1/3}Nb_{2/3})O_3$ exhibits a lower degree of 1:1 ordering than PMN. Conversely, $Pb(Zn_{1/3}Nb_{2/3})O_3$ and $Pb(Cd_{1/3}Nb_{2/3})O_3$ would be expected to have a greater tendency to favor 1:1 ordering, and work is currently underway to test this predicted trend. It is postulated that the short-range ordering in lead-based materials is directly related to the instability of the perovskite structure, since the resulting disordered Nb rich matrix will more readily form the pyrochlore phase. This would provide an explanation as to why strongly ordered materials such as PZN and PCN are difficult to sinter to the perovskite structure.

CONCLUSIONS

The relaxor material $Pb(Mg_{1/3}Nb_{2/3})O_3$ exhibits short-range 1:1 ordering of the Mg^{2+} and Nb^{5+} ions on the B-site sublattice. In undoped PMN the ordered microdomains are 2 - 5 nm in size, and have been directly observed using dark field imaging. The degree of ordering cannot be controlled by heat treatment due to the charge imbalance between the ordered and disordered regions. By doping with La^{3+} or Na^+ on the A-sites however, it is possible to either decrease or increase these charge effects respectively. Thus donor doping with La increases the degree of order, but acceptor doping with Na suppresses ordering. The tendency to 1:1 order is believed to be directly related to the stability of the pyrochlore structure with respect to perovskite in $Pb(B'_{1/3}Nb_{2/3})O_3$ systems.

Acknowledgements

REFERENCES

[1] G.A. Smolenskii and A.I. Agranovskaya "Dielectric Polarization and Losses of Some Complex Compounds" Sov. Phys.Tech. Phys.,3[7] 1380-82 (1958)

[2] V.A. Pokov and I.E. Mylnikova "Electrical and Optical Properties of Single Crystals of Ferroelectrics with a Diffused Phase Transition" Sov. Phys.-Solid State 3[3] 613-23 (1961)

[3] G.A. Smolenskii, A.I. Agranovskaya and S.N. Popov "On the Mechanism of Polarization in Solid Solutions of $Pb_3NiNb_2O_9$-$Pb_3MgNb_2O_9$" Sov. Phys.-Solid State 1[1] 147-48 (1959)

[4] G.A. Somlenskii and A.I. Agranovskaya "Dielectric Polarization of a Number of Complex Compounds " Sov. Phys.-Solid State 1[10] 1429-37 (1960)

[5] S.L. Swartz, T.R. Shrout, W.A. Schulze and L.E. Cross "Dielectric Properties of Lead-Magnesium Niobate Ceramics" J. Am. Cream. Soc. 67[5] 311-15 (1984)

[6] K. Uchino, S. Nomura, L.E. Cross, S.J. Jang and R.E. Newnham "Electrostrictive Effect in Lead Magnesium Niobate Single Crystals" J. Appl. Phys., 51[2] 1142-45 (1980)

[7] G.A. Smolenskii "Physical Phenomena in Ferroelectrics with Diffused Phase Transition" J. Phys. Soc. Jpn. [28] 26-37 (1970)

[8] B.N. Rolov "Effect of Composition Fluctuations on Unsharp Ferroelectric Phase Transitions" Sov.Phys.-Solid State 6[7] 1676-78 (1965)

[9] L. E. Cross, "Relaxor Ferroelectrics" Ferroelectrics Vol.76 241-67 (1987)

[10] N. Setter and L.E. Cross "The Contribution of Structural Disorder to Diffuse Phase Transitions in Ferroelectrics" J. Mater. Sci. 15 2478-82 (1980)

[11] N. Setter and L.E. Cross "The Role of B-site Cation Disorder in Diffuse Phase Transition Behavior of Perovskite Ferroelectrics" J. Appl. Phys. 51[8] 4356-60 (1980)

[12] M.P. Harmer, A. Bhalla, B. Fox and L.E. Cross "Electron

Microscopy of Ordered Domains in Lead Scandium Tantalate $Pb(Sc_{0.5}Ta_{0.5})O_3$" Mater. Lett. 2[4A] 278-80 (1984)

[13] H.M. Chan, M.P. Harmer, A Bhalla and L.E. Cross "TEM of the Relaxor Material $Pb(Sc_{0.5}Ta_{0.5})O_3$" J. Appl. Phys. Jpn 24 550-52 (1985)

[14] I.G. Ismailzade "An X-ray Study of the $Pb_3NiNb_2O_9-Pb_3MgNb_2O_9$ System" Sov. Phys.-Crystallography 5 292-93 (1960)

[15] H.B. Krause, J.M. Cowley and J. Wheatley "Short-range Ordering in $Pb(Mg_{1/3}Nb_{2/3})O_3$" Acta. Cryst. A35 1015-17 (1979)

[16] H.M. Chan, M.P. Harmer, A. Bhalla and L.E. Cross "Transmission Electron Microscopy of Undoped and Mn-doped Lead Magnesium Niobate:Lead Titanate,$Pb(Mg_{1/3}Nb_{2/3})O_3$:$PbTiO_3$ Relaxor Ferroelectrics" (66-E-86) Presented at 88th Annual Meeting of Am Ceram. Soc. in Chicago, IL.1986

[17] H. M. Chan and M. P. Harmer "Microstructures of High Dielectric Constant Materials" Ceramic Microstructures '86 Edited by Pask and Evans (Plenum Publishing Corporation, 1988)

[18] J. Chen, H.M. Chan and M.P. Harmer "Forced Ordering in Lanthanum-Doped Lead Magnesium Niobate" (89-E-87) Presented at 89th Annual Metting of Am. Ceram. Soc. in Pittsburgh, PA. 1987

[19] S.L. Swartz and T.R. Shrout "Fabrication of Perovskite Lead Magnesium Niobate" Mat. Res. Bull. 17 1245-50 (1982)

[20] J. Chen, A. Gorton, H.M. Chan and M.P. Harmer "Effect of Powder Purity and Second Phases on the Dielectric Properties of Lead Magnesium Niobate Ceramics" J. of Am. Ceram. Soc. Vol69 C-303 (1986)

[21] E.J. Fresia, L. Katz and R. Ward "Cation Substitution in Perovskite-like Phases" J. Am. Chem. Soc. 81 4783-85 (1959)

[22] F.S.Galasso: Structure, Properties and Preparation of Perovskite-type Compounds (Peragamon Press, New-York 1969)

[23] J.W. Edington: Practical Electron Microscopy in Materials Science (Macmillan Press, London,1975) p43

[24] K.H. Hardtl and D. Hennings "Distribution of A-site and B-site Vacancies in (Pb,La)(Ti,Zr)O_3 Ceramics" J. Am. Ceram. Soc. 55[5] 230 (1972)

[25] V.V. Kirillov and V.A. Isupov "Relaxation Polarization of $Pb(Mg_{1/3}Nb_{2/3})O_3$(PMN)-a Ferroelectric with a Diffused Phase Transition" Ferroelectrics 5 3-9 (1973)

[26] L. E. Cross "High-Permittivity Relaxation Dielectrics" Proceedings I.E.E., vol109, Part B Suppl. No.22, 1962

[27] R. D. Shannon and C. T. Prewitt "Effective Ionic Radii in Oxides and Fluorides" Acta Cryst. B25, 925-45 (1969)

Superscript

1 99.999% MgO, 99.9999% PbO, 99.999% Nb_2O_5, 99.99% La_2O_3, 99.999% Na_2CO_3 JMC Puratronic, Seabrook, NH.

2 733 Superprobe, JEOL U.S.A. Inc., Medford, MA.

3 ADP 3600, Philips Electronic Instruments.

4 400T, Philips Electronic Instruments, Inc., Mount Vernon, NY.

Figures

Fig.1   (a) Diffraction pattern of $Pb(Mg_{1/3}Nb_{2/3})O_3$ showing superlattice reflections, [0$\bar{1}$1] zone. (b) Centered dark-field image of ordered microdomains (2-5nm) in PMN using $(1/2\ 1/2\ 1/2)_s$ reflection.

Fig.2   Structure of ordered perovskite $A(B'_{1/2}B''_{1/2})O_3$

Fig.3 Schematic model showing ordered microdomains (Mg/Nb>0.5) in disordered matrix (Mg/Nb<0.5).

Fig.4 CDF images of PLMN-5%La(a), 10%La(b), 20%La(c) showing enhanced ordering as evidenced by the presence of large domains and the appearance of anti-phase domain boundaries (APB's).

Fig.5 X-ray results of La doped PMN showing the superlattice reflections ($(1/2\ 1/2\ 1/2)_s$ and $(3/2\ 1/2\ 1/2)_s$).

Fig.6 Backscattered electron image (a) and Mg X-ray map (b) of PLMN-k 10%La ($Pb_{.85}La_{.1}\square_{.05}(Mg_{1/3}Nb_{2/3})O_3$) showing the pyrochlore phase (dark grains) and the magnesium niobate phase (rectangular grains).

Fig.7 CDF image of PLMN-k 5%La showing a nonuniform microdomain structure. Region A shows enhanced ordering compared to region B. X-ray EDS shows region A to have a higher La content, and an increased Mg/Nb ratio.

Fig.8   Temperature dependence of dielectric constant (100Hz) for the undoped and La,Na doped PMN system.
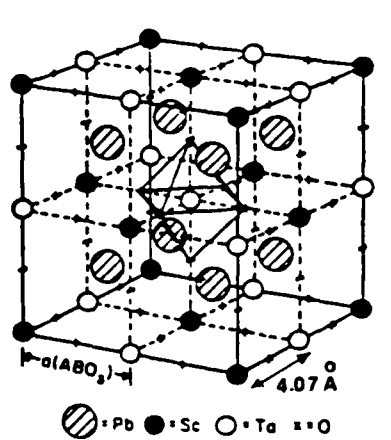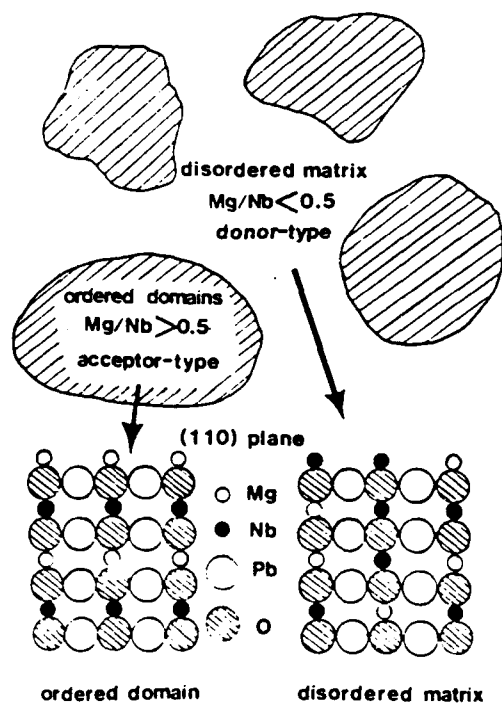
(a)　　Fig 1　　(b)

Fig 2

Fig 3

Fig. 4
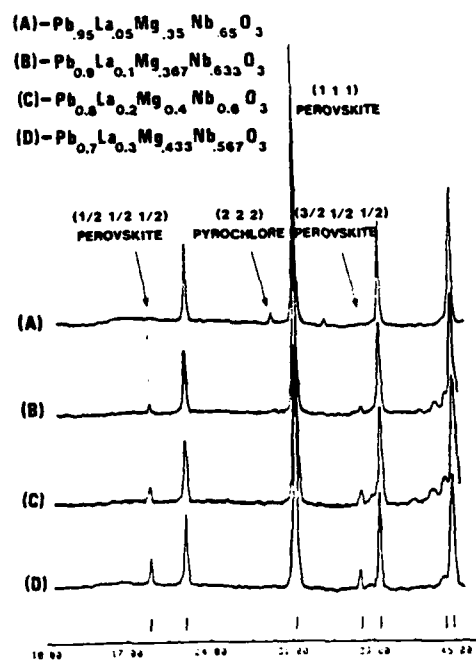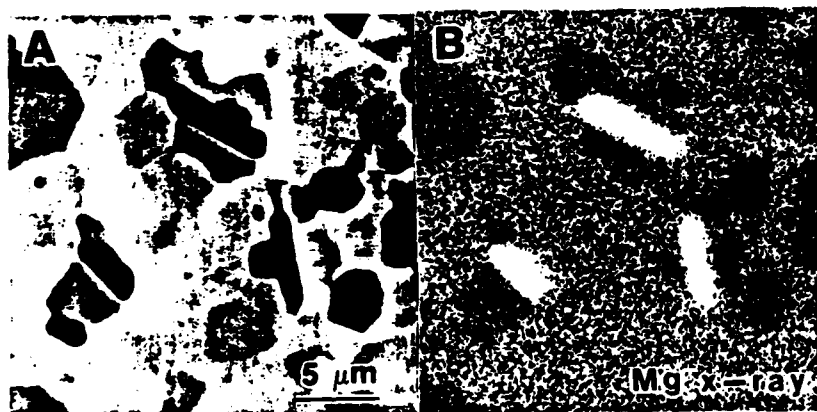
(A)$-Pb_{.95}La_{.05}Mg_{.35}Nb_{.65}O_3$

(B)$-Pb_{0.9}La_{0.1}Mg_{.367}Nb_{.633}O_3$

(C)$-Pb_{0.8}La_{0.2}Mg_{0.4}Nb_{0.6}O_3$

(D)$-Pb_{0.7}La_{0.3}Mg_{.433}Nb_{.567}O_3$

(1 1 1)
PEROVSKITE

(1/2 1/2 1/2)
PEROVSKITE

(2 2 2)
PYROCHLORE

(3/2 1/2 1/2)
PEROVSKITE

(A)

(B)

(C)

(D)
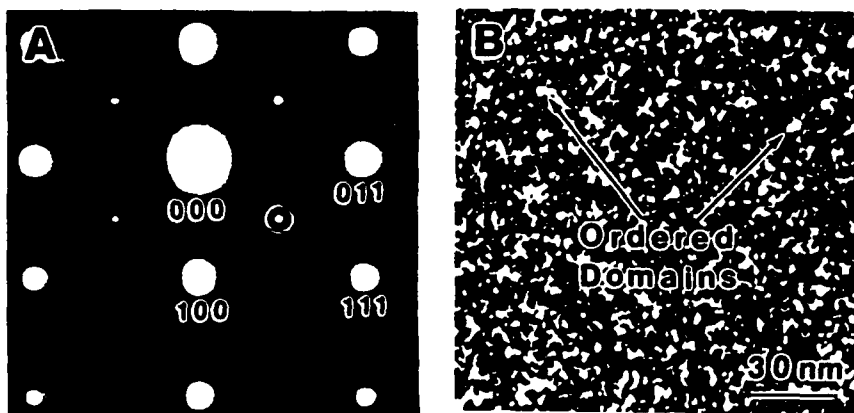
Fig. 5

(a)   Fig. 6   (b)
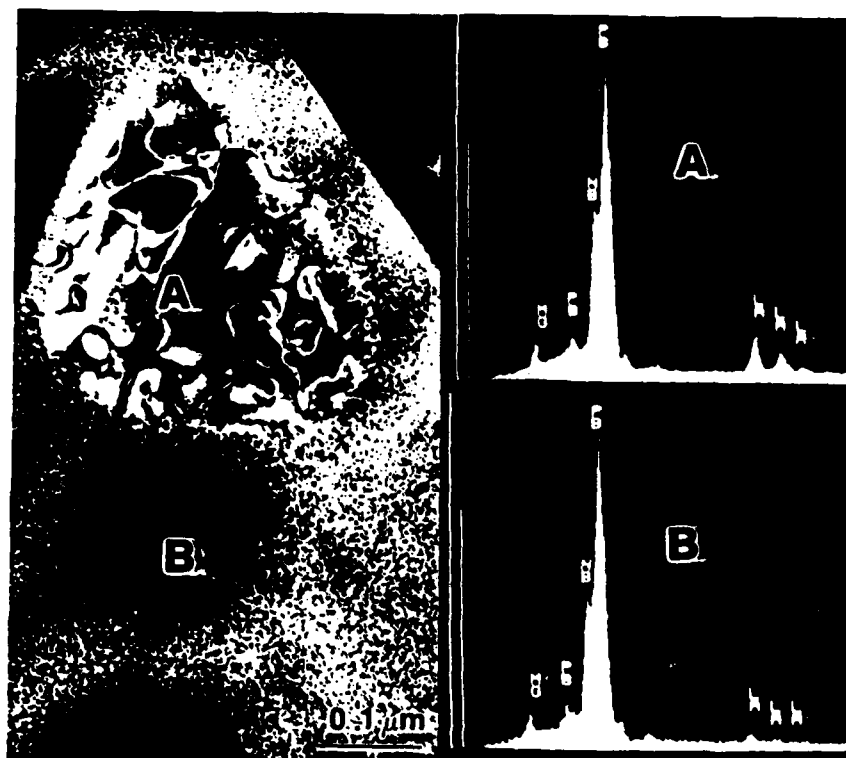
Fig. 7
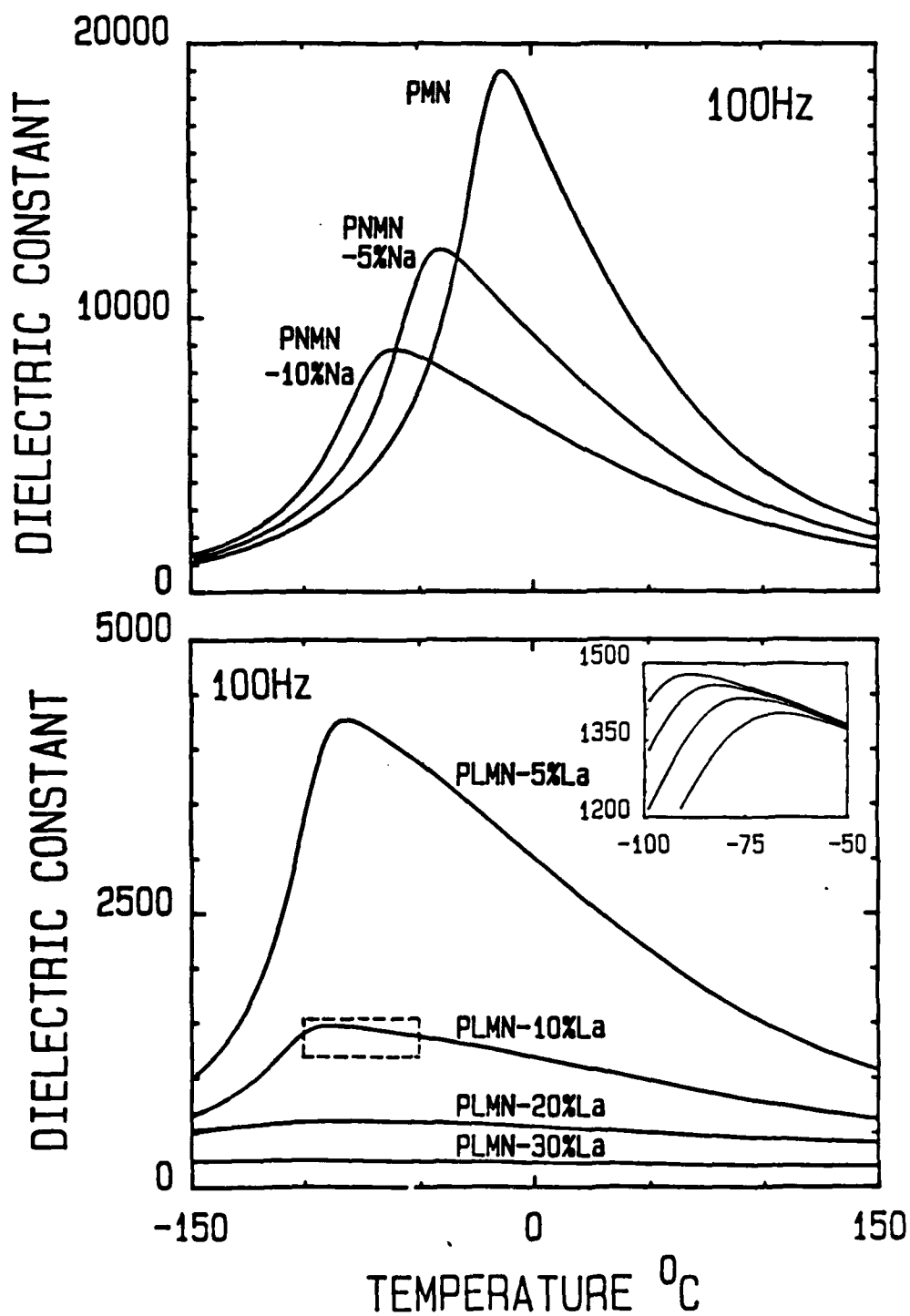
Fig. 8

----

(1) PMN   Undoped

$Pb(Mg_{1/3}Nb_{2/3})O_3$

----

(2) PLMN   Donor doped, charge

$Pb_{1-x}La_x[Mg_{(1+x)/3}Nb_{(2-x)/3}]O_3$ compensation by increasing

    x=0.05--0.30   Mg/Nb ratio

----

(3) PLMN-K   Donor doped, maintaining

$Pb_{1-3x/2}La_x\square_{x/2}[Mg_{1/3}Nb_{2/3}]O_3$ Mg/Nb ratio

    x=0.03--0.20

----

(4) PLNMN   Co-doped , Mg/Nb ratio

$Pb_{1-2x}La_xNa_x[Mg_{1/3}Nb_{2/3}]O_3$ unchanged

    x=0.10--0.20

----

(5) PNMN   Acceptor doped, charge

$Pb_{1-x}Na_x[Mg_{(1-x)/3}Nb_{(2+x)/3}]O_3$ compensation by decrease

    x=0.05--0.10   Mg/Nb ratio.

Table-1

	PMN-base materials	Mg/Nb ratio	ordered domain size
PMN	$Pb(Mg_{1/3}Nb_{2/3})O_3$	0.50	2--5nm
	$Pb_{.95}La_{.05}(Mg_{.35}Nb_{.65})O_3$	0.54	10-20nm
PLMN	$Pb_{.9}La_{.1}(Mg_{.367}Nb_{.633})O_3$	0.58	-100nm
5%- 30%	$Pb_{.8}La_{.2}(Mg_{.40}Nb_{.60})O_3$	0.67	>300nm
	$Pb_{.7}La_{.3}(Mg_{.433}Nb_{.567})O_3$	0.76	>500nm
PLNMN 10%-	$Pb_{.8}La_{.1}Na_{.1}(Mg_{1/3}Nb_{2/3})O_3$	0.50	2--5nm
20%	$Pb_{.6}La_{.2}Na_{.2}(Mg_{1/3}Nb_{2/3})O_3$	0.50	2--5nm
PNMN 5%-	$Pb_{.95}Na_{.05}(Mg_{.317}Nb_{.683})O_3$	0.46	2--5nm
10%	$Pb_{.9}Na_{.1}(Mg_{.30}Nb_{.70})O_3$	0.43	almost disorder

Table-2

COMPOSITION

	PMN	PLMN 5%La	PLMN 10%La	PLMN 20%La	PLMN 30%La	PLNMN 10%	PNMN 5%Na	PNMN 10%Na
ΔT_o ($^\circ$C)	15.4	22	21	9	9	22.5	19	21
δ ($^\circ$C)	47	98	151	/	/	/	58	70

Table-3

ORDERING OF BARIUM ZINC NIOBATE
WITH PEROVSKITE STRUCTURE

Ping Peng, Martin P. Harmer and Donald M. Smyth
Department of Materials Science and Engineering
The Materials Research Center
Lehigh Universoty, Bethlehem, PA 18015

[ABSTRACT]

In the perovskite-like materials with general formula $A(B'_{1/3}B''_{2/3})O_3$, the B' and B'' atoms may be either randomly distributed or ordered. Barium Zinc Niobate has been reported to have the cubic structure by X-ray diffraction study. In this study, partially ordered stoichiometric $Ba(Zn_{1/3}Nb_{2/3})O_3$ (BZN, Zn/Nb=1/2) has been identified by electron diffraction. Ordered domains having 1:1 or 1:2 packing sequences of B-site cation layers were observed. Although the high temperature annealing cannot enhance the 1:1 ordered phase, it does promote the 1:2 ordered phase preferentially along grain boundary region. The preference of different ordered phases in nonstoichiometric BZN(Zn/Nb≠1/2) depends on the Zn/Nb ratio. Zn rich BZN shows 1:1 type ordering. However, Nb rich BZN eliminates the 1:1 type ordering and promotes the 1:2 type ordering which can be related to the heat treatment result, where Zn loss can cause the Nb rich nonstoichiometry.

INTRODUCTION

Dielectric ceramic resonators have been extensively studied for microwave component applications in the past 15 years. The main benefit of using dielectric materials is the reduction of the physical size of the microwave component[1,2,3]. Recently, complex perovskite compounds with general formula $A(B'_{1/3}B''_{2/3})O_3$ have been found to have desirable properties for microwave resonator applications[2,3,4,5,6]. These compounds have high dielectric constants k(20~40), high dielectric loss quality Q(~10^5) and small temperature coefficient of resonating frequency T_f(< 5ppm/°c). However the microstructures and defect chemistry of these kinds of materials are not well understood. Microchemical ordering[4,5], solid solution additives[6] and nonstoichiomestry[7], each has a strong influence on the microwave properties. The purpose of this study is to investigate the effect of chemical modification on the ordered structures of BZN.

The crystal structure of $A(B'B'')O_3$ type complex perovskites has been investigated by Galasso et. al.[8,9,10,11,12]. The octahedral B-site cations can be either randomly distributed

or ordered. The majority of the studies of B-site cation ordering in perovskites has been conducted on stoichiometric ternary perovskites of general formula: $A(B'_{1/2}B''_{1/2})O_3$, $A(B'_{1/3}B''_{2/3})O_3$ and $A(B'_{2/3}B''_{1/3})O_3$[8,10,11].[1] Figure 1 is a schematic diagram showing possible cation ordering schemes in the perovskite structure. The ordering of B-site cations in $A(B'_{1/2}B''_{1/2})O_3$ type compounds has been extensively studied[8,13,14,15,16]. However, very few detailed structural investigations of ordering in $A(B'_{1/3}B''_{2/3})O_3$ systems have been reported. In some $A(B'_{1/3}B''_{2/3})O_3$ systems, such as $Ba(Zn_{1/3}Ta_{2/3})O_3$, $Sr(Zn_{1/3}Ta_{2/3})O_3$ etc.[8], 1:2 type ordering has been observed. Whereas in other systems, such as $Pb(Mg_{1/3}Nb_{2/3})O_3$[17], $Ba(U_{1/3}Fe_{2/3})O_3$[18], $Sr(W_{1/3}Sc_{2/3})O_3$[19] and $Sr(Sr_{1/3}Nb_{2/3})O_3$[20]], 1:1 type ordering has been observed.

Stoichiometric BZN(Zn/Nb=1/2) has been reported to have a cubic structure with space group Pm3m, where the cations Zn and Nb are randomly distributed[12]. In this study, the partially ordered nature of stoichiometric BZN has been identified by electron diffraction. It has also been found that the Zn/Nb ratio plays an important role in determining the nature of the ordering in nonstoichiometric BZN(Zn/Nb$\neq$1/2). Nb-rich BZN favors 1:2 type of ordering which can be promoted by high temperature annealing. On the other hand, Zn-rich BZN shows only 1:1 type ordering, which cannot be enhanced by thermal annealing. The 1:1 type ordering can be enhanced, however, by doping La into the Ba sites.

EXPERIMENTAL PROCEDURES

A summary of the compositions of the samples studied is given in table I. All polycrystalline ceramics were made by a conventional ceramic processing method. The starting materials; $BaCO_3$, ZnO, Nb_2O_5 and La_2O_3(purity> 99.99%[2]) were mixed and ball milled in polyethylene bottles using latex coated iron balls for 24 hours in alcohol, dried and then calcined at 1000°C for 10 hours. Samples were cold pressed under 1 ton/cm^2 and sintered between 1350°C and 1600°C for 3 hours. Some of the stoichiometric BZN samples were quenched from 1400, 1500 and 1600°C to room temperature, a few were fast fired at 1600°C and some were annealed at 1400°C. Nonstoichiometric BZNZ and BZNN were investigated to see how the ordering type was affected by changes in the Zn/Nb ratio. BLZN and BLZN' were fabricated to test whether La could enhance 1:1 type ordering. Final relative densities in the range of 90 -- 98% were achieved for all samples except the heavily Zn rich sample(BZNZ with x>3%), which only reached about 80% of theoretical density.

---

[1]*Numerical superscripts(B^1, B^2) refer to B-layer stacking sequence; slash superscripts(B', B'') refer to B-atom identity.*

[2]*99.99% high purity materials are purchased through JMC Puratronic, Seabrook, NH.*

Polished sections of samples were analyzed on an electron microprobe(EMPA)[3] and X-ray powder diffractometry(XRD)[4]. Thin foils were prepared as follows: the bulk samples were polished on SiC paper down to about 50~100 μm, thin section was then ion beam thinned[5] under 5.5kv and liquid N_2 cooling stage to avoid ion beam damage. The thin foil specimens were examed in a transmission electron microscope(TEM)[6] equiped with an energy dispersive X-ray detector for chemical analysis. High resolution TEM images were taken at 300 kv with near Scherzer defocus as determined by optical diffractometry(ODM).

RESULTS and DISCUSSIONS

(1) Stoichiometric BZN

(a) 1:1 type of ordering

The stoichiometric BZN was sintered at 1600°C for 3 hours and furnace cooled (-400°C/hr.) to room temperature. XRD results showed that the samples were single phase with perovskite structure with a=0.4094 nm(figure 2a). However, as can be seen in the selected area electron diffraction(SAED) pattern(figure 2b), diffuse superlattice reflections of the type $(\frac{h}{2} \frac{k}{2} \frac{l}{2})$ (h k l odd) were obtained in the electron diffraction patterns, thus indicating a doubling of BZN unit cell dimension due to ordering. Figure 2d shows a centered dark-field (CDF) micrograph taken using a $(\frac{1}{2} \frac{1}{2} \frac{1}{2})$ reflection; the bright regions(2~5 nm) are ordered domains. Identical CDF images were obtained when imaging by using different variants of the $(\frac{1}{2} \frac{1}{2} \frac{1}{2})$ family of reflections. Since the $(\frac{1}{2} 0 0)$ and $(\frac{1}{2} \frac{1}{2} 0)$ reflections were absent, and no dynamical absences were observed in the convergent beam electron diffraction(CBED) patterns[21], it was concluded that the lattice type in 1:1 type ordered BZN was face centered cubic(FCC). By analogy with lead scandium tantalate(PST)[15, 16], the above results indicate that the structure of ordered BZN is of general form $A(B'_{1/2}B''_{1/2})O_3$(figuer 1b). The two most likely ordering models consistent with this ordering scheme are:

MODEL 1: B^1----- Zn^{2+} and Nb^{5+} (disordered, 2:1 ratio)

B^2----- Nb^{5+}
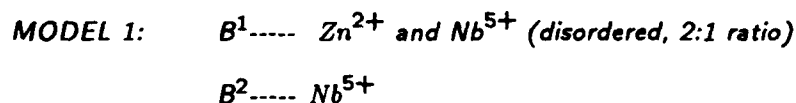
This type of ordering is equivalent to the $(NH_4)_3FeF_6$[14] type structure, and has been reported to occur in some other systems[8, 17, 18, 19, 20]. Padel[18] calculated the ordering

---

[3] *733 Superprobe, JEOL U.S.A. Inc., Medford, MA.*

[4] *ADP 3600, Philips Electronic Instruments.*

[5] *Ion Beam Thinner, Gaton 600,*

[6] *400T equiped with TN2000 MCA X-ray analyser and 430T capable offering Scherzer resolution of about 2.30 Å, Philips Electronic Instruments, Inc., Mount Vernon, NY.*

based on the X-ray analysis for the system $Ba(U_{1/3}Fe_{2/3})O_3$. The simulation results were in good agreement with his experimental results. In this model, the ordered BZN structure can be represented as $Ba[(Zn_{2/3}Nb_{1/3})_{1/2}Nb_{1/2}]O_3$; thus the B^2 layer sites are occupied exclusively by Nb^{5+} ions, and the B^1 layer sites are occupied by a random mixture of the remaining Zn^{2+} and Nb^{5+} ions. Because the average composition of ordered regions is identical to that of the bulk BZN, no charge imbalance exists within the ordered regions. Hence, if that were the case, the ordered domains would be expected to grow during heat treatment. Experimentally, however, the domains were not observed to grow. Table II summarizes the heat treatment results. As can be seen, the 1:1 type ordering persists at all heat treatments. It follows, therefore, that 1:1 type ordered domain growth is strongly inhibited in stoichiometric BZN. This can be explained more easily on the basis of model 2.

MODEL 2: B^1 ----- Zn^{2+}

   B^2 ----- Nb^{5+}
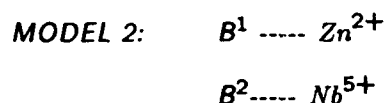
In this model, it is postulated that the Zn^{2+} and Nb^{5+} ions order in a 1:1 ratio on the B site sublattice of BZN. This is directly analogous to the ordered PST structure for this type of ordering. Assuming that the Zn/Nb ratio is 1:1 (or close to 1:1) within the ordered domains, (as opposed to 1:2 for the average composition), strong charge effects would result, in which the ordered regions would have a net negative charge with respect to the surrounding region. This in turn, would be expected to severely restrain domain growth, and indeed, this was observed. In view of this fact, we are inclined to favor model 2 over model 1. Since the ordered regions would be Zn rich (relative to the average BZN composition), in order to preserve stoichiometry, the regions between the domains would have to be Nb rich. It then follows that the 1:1 type ordered domains would in fact be acceptor-type island regions(Zn/Nb>1/2), in a donor-type disordered matrix(Zn/Nb<1/2). Fender et. al.[9] studied oxygen difficient barium zinc tantalate(BZT) with formula $Ba(Zn_{1/2}Ta_{1/2})O_3$ and found very weak 1:1 type ordering by X-ray analysis, which supports model 2.

   (b) 1:2 type of ordering

The SAED patterns with long exposure time taken from the [110] and [111] zone axes are shown in figures 2b,c. Both 1:1 type ordered superlattice spots and other weak superlattice reflections of type $(\frac{h}{3} \frac{k}{3} \frac{l}{3})$ can be observed. Unfortunately, the superlattice reflections located in the $(\frac{1}{3} \frac{1}{3} \frac{2}{3})$ and $(\frac{2}{3} \frac{2}{3} \frac{4}{3})$ in the [111] zone axis were too weak to resolve the ordered domains by the CDF technique.

The simplest and most straight forword 1:2 ordering scheme for BZN is:[7](figure 1)

$$B^1 ------ Zn^{2+}$$
$$B^2 ------ Nb^{5+}$$
$$B^2 ------ Nb^{5+}$$
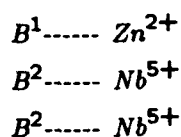
This ordering arrangement, which does not involve any charge imbalance would be expected to coarsen upon annealing, kinetics permitting. To test this concept, samples were annealed for long periods(100hrs. at 1400°C) and subsequently examined by TEM. Figure 4 shows significant 1:2 ordering in these samples located preferentially near the grain boundary region. During annealing, a significant amount of zinc was volatilized out of the samples (figure 5), preferentially from the grain boundary region. It would appear, therefore, that the enhanced 1:2 ordering at the grain boundaries was promoted by a zinc deficiency in those regions. It also suggests that ordering in BZN may be sensitive to the Zn/Nb nonstoichiometry. A summary of the proposed microstructure and ordering arrangement in stoichiometric BZN is shown in figure 3. It comprises a mixture of three phases: an isolated 1:1 type ordered phase(Zn/Nb≈1:1); an isolated 1:2 type ordered phase(Zn/Nb=1:2); and a continous disordered phase(Zn/Nb≤1:2).

(2) La doped BZN

(a) Zn/Nb ratio increased (BLZN):

In an attempt to distinquish between models 1 and 2, a series of samples was made up of the following compositions:

$$Ba_{1-x}La_x(Zn_{(1+x)/3}Nb_{(2-x)/3})O_3, \quad \text{where } x=1\%, 5\%, 10\%.$$
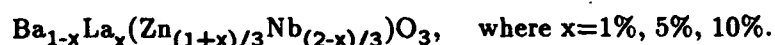
For these compositions, La^{3+} ions are substituted for Ba^{2+} ions on the A site sublattice. Since La is trivalent whereas Ba is divalent, the La behaves as a donor dopant. In this series of samples, the compositions are adjusted so that compensation for the La is achieved by increasing the Zn:Nb ratio. Now let us consider how this influences the 1:1 type of ordering behavior. In the case of model 1, since the Zn/Nb ratio in the ordered regions is the same as in the bulk, there is no charge imbalance resulting from the ordering, thus La doping would not be expected to influence the degree of ordering. However, for model 2, since the ordered regions are Zn rich, they can be considered to be acceptor doped. Thus donor doping with La would be expected to compensate the charge effects resulting from ordering, and hence favor an increased degree of order. As can be seen in the following discussion, enhanced ordering

---

[7]*An alternative 1:2 type ordering scheme for $Sr(Sr_{1/3}Nb_{2/3})O_3$ has been proposed by Raveau et. al.[20]. It corresponds to an ordered arrangement of the type: $Sr_3(B'=Zn_2Nb, B''=Nb)O_9$.*

was indeed observed, thus favoring model 2.

SAED patterns show that the intensity of the $(\frac{1}{2}\,\frac{1}{2}\,\frac{1}{2})$ type superlattice reflections increase with the La^{3+} concentration, thus indicating an increased degree of order. In addition, CDF images reveal that the size of ordered domains increased from $10\sim20$ nm to > 500nm(see figure 6). The wavy boundaries seperating the ordered domains are anti-phase domain boundaries(APB's)[22].
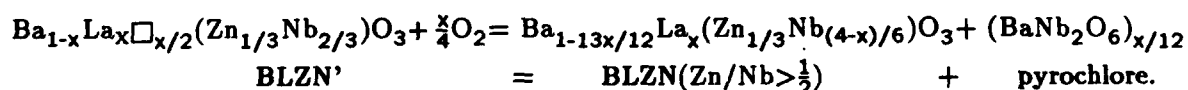
(b) Zn/Nb ratio unchanged (BLZN'):

$$Ba_{1-x}La_x\square_{x/2}(Zn_{1/3}Nb_{2/3})O_3 \;^8 \quad \text{where x=1\%, 5\%, 10\%;}$$
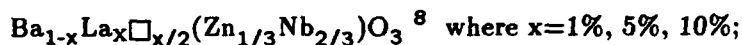
For this series of samples, the intention was to test whether the La doping could be compensated by the introduction of barium vacancies.

Examination of the sintered microstructures using TEM and EMPA revealed a pyrochlore second phase(figure 7). XRD results showed that as the La concentration increased, the volume fraction of pyrochlore second phase increased accordingly. In addition, TEM revealed that the ordered domain structure of these specimens was identical to that of the BLZN compositions(i.e. where compensation was achieved by adjustment of the Zn/Nb ratio).

It can be concluded from these results that barium vacancies are not *favorable defect* species in this system. Instead, the system prefers to restore the A:B ratio via the formation of pyrochlore phase(which is Nb rich), and by self-adjusting the Zn/Nb ratio which results in the enhancement of 1:1 type of ordering. The reaction equation can be written as

$$Ba_{1-x}La_x\square_{x/2}(Zn_{1/3}Nb_{2/3})O_3+\tfrac{x}{4}O_2= Ba_{1-13x/12}La_x(Zn_{1/3}Nb_{(4-x)/6})O_3+ (BaNb_2O_6)_{x/12}$$

$$\text{BLZN'} \qquad = \qquad \text{BLZN(Zn/Nb>}\tfrac{1}{2}\text{)} \qquad + \qquad \text{pyrochlore.}$$

(3) Nonstoichiometric BZN

Further information on the mechanism of ordering in BZN can be obtained through an adjustment of nonstoichiometry. Figure 8 shows the SAED patterns of a systematic study of a series of Zn and Nb rich nonstoichiometric BZN.

(a) Zn rich nonstoichiometric BZN (BZNZ)

As discussed previously, La doping increases the Zn/Nb ratio and enhances 1:1 type ordering. If model 2 is the correct interpretation for 1:1 type ordering, the Zn rich nonstoichiometric BZN with formula

$$Ba(Zn_{1/3}Nb_{2/3})_{1-x}Zn_xO_3, \quad \text{Where x= 0.5, 1, 3\%}$$
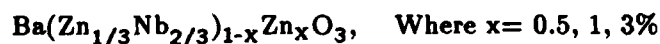
should be inclined towards 1:1 type ordering. The experimental results indicate that this is the

---

$^8\square$ *stands for a vacancy.*

case. The 1:1 type ordered domains were observed in all BZNZ samples. There appears to be almost no difference in the size of the domains observed among different BZNZ samples. Notice that the 1:2 type of superlattice reflections, however, become weaker and eventually disappear as the Zn concentration increases. This behavior could be understood as a competition between Zn rich 1:1 type ordering and Nb rich 1:2 type ordering. The higher the Zn/Nb ratio, the more the 1:1 type ordering, and the less the 1:2 type ordering due to the corresponding chemical composition adjustment in the disordered matrix.

(b) Nb rich nonstoichiometric BZN (BZNN)

In this case, samples with formula

$$Ba(Zn_{1/3}Nb_{2/3})_{1-x}Nb_xO_3, \quad \text{where } x=0.5, 1, 2, 3, 9\%;$$
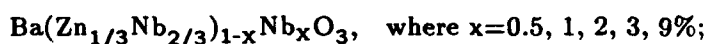
favor the 1:2 type of ordering. As shown in figures 8, the degree of ordering increases with Nb concentration, and the ordered domains can be controlled by heat treatment. The 1:2 type ordered domains do grow with increasing Nb concentration(figure 9) and/or high temperature annealing(figure 10). This behavior is different to the 1:1 type ordering in the BZNZ system, but it is consistent with the heat treatment results of stoichiometric BZN and BZNZ(figures 4,10). The grain boundary nucleation of 1:2 ordered domains in BZNZ(figure 10a) was believed due to Zn loss through grain boundary.

The 1:2 type ordering in the $A(B'_{1/3}B''_{2/3})O_3$ system can be understood based on the simple model presented earlier. Since the 1:2 type ordered trigonal phase(space group P3̄m1) is generated from a disordered cubic matrix(space group Pm3m), the orientation relationship between these two phases should be geometrically simple[24,25]. As shown in table III, four orientational variants are expected in this system, which were indeed observed in the present study(figure 11). Figure 12 is a high resolution transmission electron micrograph(HRTEM) of BZNN with x=2% taken at near Scherzer defocus condition. Ordered domains with two different variants can be seen in this image. Laser optical diffractometry was used to check the orientation relationship. The laser beam was focused on the ordered domains with different variants in the HRTEM micrograph, and superlattice reflections with two different variants were revealed. With increasing Nb concentration, the 1:2 type ordered domains coarsen. Finally for x=9%, SAED patterns from an ordered domain shows only one variant(figure 8f).

CONCLUSIONS

(1) Stoichiometric BZN contains a mixture of 1:1 and 1:2 short-range ordered phases. The 1:1 type ordered domains(2~4 nm in size) are uniformly distributed, which could be directly imaged by TEM using the CDF technique. The degree of 1:1 ordering could not be

7

controlled by heat treatment due to the charge imbalance created by the 1:1 type of order, but could be promoted by lanthanum doping on the A-sites. The intrinsic 1:2 ordered phase in stoichiometric BZN diffracts electrons too weak to image the ordered domains by CDF in the TEM.

(2) The type of ordering in nonstoichiometric BZN depends on the Zn/Nb ratio. If the Zn/Nb ratio is greater than $\frac{1}{2}$, it prefers 1:1 type of ordering; if the Zn/Nb ratio is less than $\frac{1}{2}$, it favors 1:2 type of ordering.

(3) The 1:2 type of ordering maintains the same chemical composition as the bulk. The degree of 1:2 ordering can be controlled by either heat treatment or by making BZN Nb rich. The SAED patterns of a series of Nb rich nonstoichiometric BZN samples can be explained by the formation of four possible variants of the ordered trigonal superstructure from a cubic matrix.

(4) High temperature annealing causes Zn loss which generates 1:2 type of ordering preferencially along the grain boundary region.

Table I Chemical composition summary

BZN: $Ba(Zn_{1/3}Nb_{2/3})O_3$	stoichiometric undoped BZN.
BZNZ: $Ba(Zn_{1/3}Nb_{2/3})_{1-x}Zn_xO_3$ x=0.005 — 0.03	nonstoichiometric BZN ; Zn rich and acceptor doped. $Zn/Nb > 1/2$.
BZNN: $Ba(Zn_{1/3}Nb_{2/3})_{1-x}Nb_xO_3$ x= 0.005 — 0.09	nonstoichiometric BZN; Nb rich and donor doped. $Zn/Nb < 1/2$.
BLZN: $Ba_{1-x}La_x(Zn_{(1+x)/3}Nb_{(2-x)/3})O_3$ x=0.01 — 0.10	donor doped, charge compensated by increasing Zn/Nb ratio.
BLZN': $Ba_{1-x}La_x\square_{x/2}(Zn_{1/3}Nb_{2/3})O_3$ x= 0.01 — 0.10	donor doped, maintaining Zn/Nb ratio.

Table II heat treatment of stoichiometric BZN

heat treatment	phase	structure
sintered at 1600°C and furnace cooled	single(fig.2a)	mixture of short range ordering of 1:1 and 1:2 type(fig. 2b,c)
fast fired at 1600°C	single	same as above
quenched from 1600 1500, 1400°C	single	1:1 type ordering only
Annealed at 1400°C for 100 hrs.	surface: Nb rich pyrochlore, bulk: Nb rich phase along grain boundaries	mixture of short range ordering of 1:1 and grain boundary nucleation of 1:2 type ordered phases(fig. 4)

Table III Orientation relationship between four variants of ordered phase and cubic phase
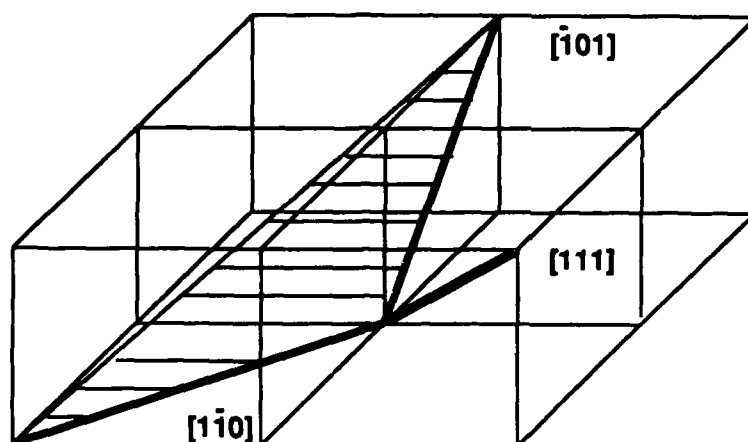
$<\bar{1}01>_{dc}{}^* --- <100>_{ot}$ or $<2\bar{1}\bar{1}0>_{ot}$ *angle:* $(<\bar{1}01>_{dc}$ & $<1\bar{1}0>_{dc})= 120°$

$<1\bar{1}0>_{dc} --- <010>_{ot}$ or $<\bar{1}2\bar{1}0>_{ot}$ *angle:* $(<100>_{ot}$ & $<010>_{ot})= 120°$

$[111]_{dc} --- [001]_{ot}$ or $[0001]_{ot}$

variant 1	*variant* 2	*variant* 3	*variant* 4
$<1\bar{1}0>$	$<0\bar{1}1>$	$<101>$	$<011>$
$<\bar{1}01>$	$<110>$	$<\bar{1}10>$	$<\bar{1}01>$
$[111]$	$[\bar{1}11]$	$[\bar{1}\bar{1}1]$	$[1\bar{1}1]$

* dc stands for disordered cubic phase, and ot stands for ordered trigonal phase.

REFERENCES

[1] K. WAKINO; Invited talk at 6th IEEE Int. Symp. on Ferroelectric, June 8-11(1986), Lehigh University.

[2] H. TAMURA, T. KONOIKE, Y. SAKAB, and K. WAKINO; J. of Amer. Cer. Soc. C59, 67, (1984)

[3] K. WAKINO, K. MINAI, and H. TAMURA; ibit, 278, 67, (1984)

[4] K. MATSUMO, T. HINGA, K. TAKADA and H. ICHIMURA; Proc. of 6th IEEE Int. Symp. on Ferroelectric, June 8-11(1986), Lehigh University, pg.

[5] H. TAMURA, D. A. SAGALA and K. WAKINO; Japan. J. Appl. Phys., 787, ,(1986)

[6] K. WAKINO, D. A. SAGALA, and H. TAMURA; ibit, 1042, 24, (1985)

[7] S. B. DESU, H. M. O'BRYAN; J.of Amer. Cer. Soc. 546, 68, (1985)

[8] F. GALASSO; "Structure croperties and preperation of perovskite-type compounds", Oxford, pergamon, (1969)

[9] A. J. JACOBSON, B. M. COLLINS, and B. F. F. FENDER; Acta Cryst., 1083, B32, (1976)

[10] G. BLASSE; Inorgan. Nucl. Chem., 993, 27, (1965)

[11] R. ROY; J. of Amer. Cer. Soc., 581, 37, (1954)

[12] F. GALASSO and J. PYLE; Inorgan. Chem., 482, 2, (1963)

[13] J. B. GOODNOUGH and J. M. LONGO; "Crystallographic and Magnetic Properties of Perovskite and Perovskite Related Compounds", Landolt-Bornstein, New series, Group III, Vol. 4a, N. Y. Springer-Verlag, (1970)

[14] L. PAULING; J. of Amer. Chem. Soc., 2738, 46, (1924)

[15] N. SETTER; "The Role of Positional Disorder in Ferroelectric Relaxers", PhD. Thesis at Penn. State University, (1980)

[16] H. M. CHAN, M. P. HARMER, A. BHALLA and L. E. CROSS; Japan. J. of Appl. Phys., 550, 24, (1985)

[17] J. CHEN, H. M. CHAN and M. P. HARMER; presented at the 89 annual meeting of Amer. Cer. Soc., (1987)

[18] L. PADEL, P. POIX, and A.MICHEL; Revue de chimie minerale, 337, 9, (1972)

[19] E. J. FRESIA, L. KATZ and R. WARD; J. of Amer. Cer. Soc. 4783, 81, (1959)

[20] J. JECOMTE, J. P. LOUP, M. HERVIEU and B. RAVEAU; J. of Soli. Stat. Physica, 743, 65, (1981)

[21] D.B. WALLIAMS; "Analytical Electron Microscopy", p ,

[22] J. W. EDINGTON; "Practical Electron Microscopy in Materials Science", p43, Mcmillan Press, London, (1975)

[23] W. SLEIGHT, J. LONGO and R.WARD; Inorg. Chem., 245, 1, (1962)

[24] P. F. REYNAUD; J. Appl. Cryst., 263, 9, (1976)

[25] L. KATZ and R. WARD; Inorg. Chem. 205, 3, (1964)
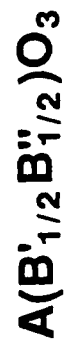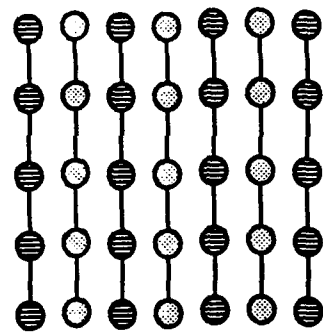
(1) *Ordering scheme of complex perovskite*
(a) ABO_3 *ideal perovskite with disordered cubic structure;* (b) $A(B'_{1/2}B''_{1/2})O_3$ *with*
1:1 type ordered face centered cubic(FCC) structure; (c) $A(B'_{1/3}B''_{2/3})O_3$ *with 1:2*
type ordered trigonal structure.

(2) *Structure information of stoichiometric BZN*
(a) *X-ray diffraction(XRD) pattern showing single phase with cubic ideal perovskite*
structure; (b) *selected area electron diffraction(SAED) patterns taken from* [110]
zone axis showing a 1:1 type of ordering, notice the intensity singularity in $\frac{1}{3}$ *and* $\frac{2}{3}$
positions along <111> *direction;* (c) *SAED patterns from* [111] *zone axis,*
notice very faint 1:2 type of superlattice spots; (d) *TEM centered dark field(CDF)*
image($\frac{1}{2}\frac{1}{2}\frac{1}{2}$ reflection) showing very fine 1:1 type microdomains(bright dots).

(3) *Schematic model of stoichiometric BZN.*

(4) *CDF image($\frac{1}{3}\frac{1}{3}\frac{1}{3}$ reflection) of stoichiometric BZN annealed at 1400°C for 100 hrs.*
showing grain boundary(black arrow pointed) nucleation of 1:2 type of ordered
domain structure(bright region) and no significant chemical composition difference
between the ordered phase and matrix can be detected by microchemical analysis.

(5) *Weight change of stoichiometric BZN at 1400°C versus time.*

(6) *CDF image($\frac{1}{2}\frac{1}{2}\frac{1}{2}$ reflection) of* $Ba_{1-x}La_x(Zn_{(1+x)/3}Nb_{(2-x)/3})O_3$*, with* (a) x=0.01,
(b) x=0.05, (c) x=0.10; *notice the degree of ordering increases with increasing of*
the doping concentration of lanthanum.

(7) *Bright field(BF) and CDF image($\frac{1}{2}\frac{1}{2}\frac{1}{2}$ reflaction) of BLZNV with x=10%,*
notice a pyrochlore second phase(arrow) along the grain boundary and APB's.

(8) *SAED patterns of* [110] *zone axes of systematic study of* $Ba(Zn_{1/3}Nb_{2/3})_{1-x}M_xO_3$
(a) *stoichiometric BZN: M=0, x=0.00;*
(b) *nonstoichiometric BZNZ: M=Zn, x=0.005;*
(c) *nonstoichiometric BZNZ: M=Zn, x=0.01;*
(d) *nonstoichiometric BZNN: M=Nb, x=0.01;*
(e) *nonstoichiometric BZNN: M=Nb, x=0.03;*
(f) *nonstoichiometric BZNN: M=Nb, x=0.09.*

(9) *TEM CDF image($\frac{1}{3}\frac{1}{3}\frac{1}{3}$ reflection) of BZNN with x=0.02(a), 0.09(b); the bright*
regions are 1:2 type ordered domains.

(10) *TEM CDF image($\frac{1}{3}\frac{1}{3}\frac{1}{3}$ reflection) of x=0.01(a) BZNZ and x=0.02(b) BZNN*
annealed at 1400°C for 100 hrs., notice the grain boundary nucleation and uniformly
distributed 1:2 type ordered domain structure in two cases respectively.

(11) *SAED patterns of four variants in 1:2 type ordered BZN*
(a) $[110]_{dc}=[100]_{ot}$ *or* $[2\bar{1}\bar{1}0]_{ot}$ *zone axis of BZNN with x= 0.03;*
(b) $[012]_{dc}=[0\bar{1}\bar{1}]_{ot}$ *or* $[1\bar{2}13]_{ot}$ *zone axis of BZNN with x=0.03;*
(c) $[113]_{dc}=[0\bar{2}1]_{ot}$ *or* $[\bar{2}463]_{ot}$ *zone axis of BZNN with x=0.03.*

(12) *HRTEM of BZNN with x=0.02; 1:2 type of ordered domains with two*
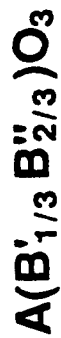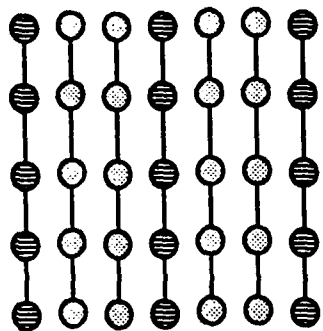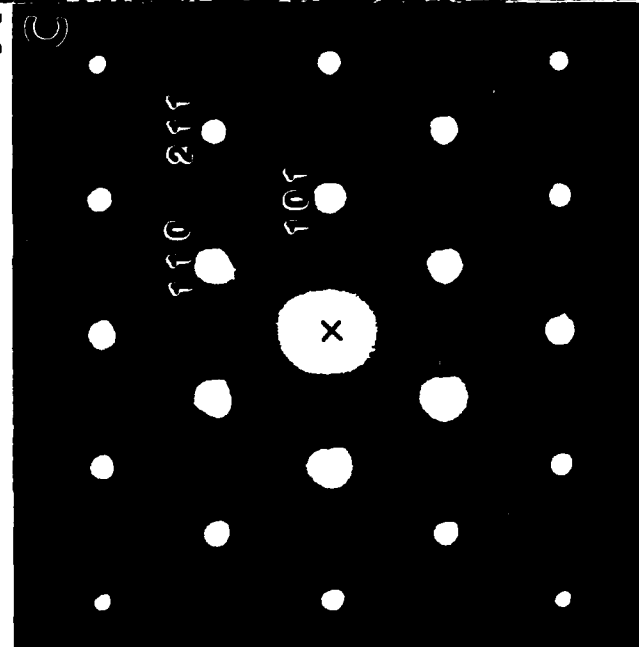*orientations were observed. The laser optical photographs indicate two different*
variants.
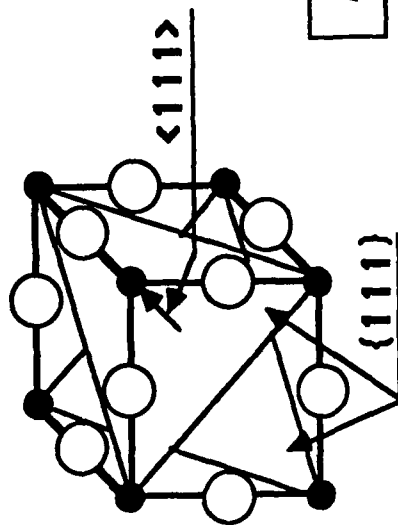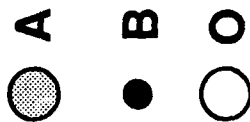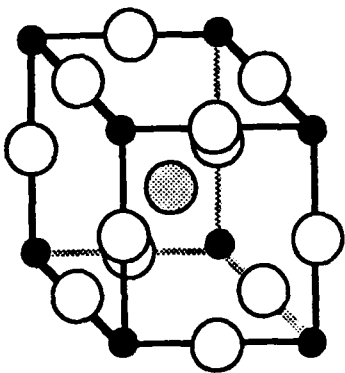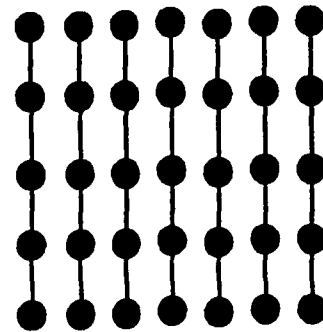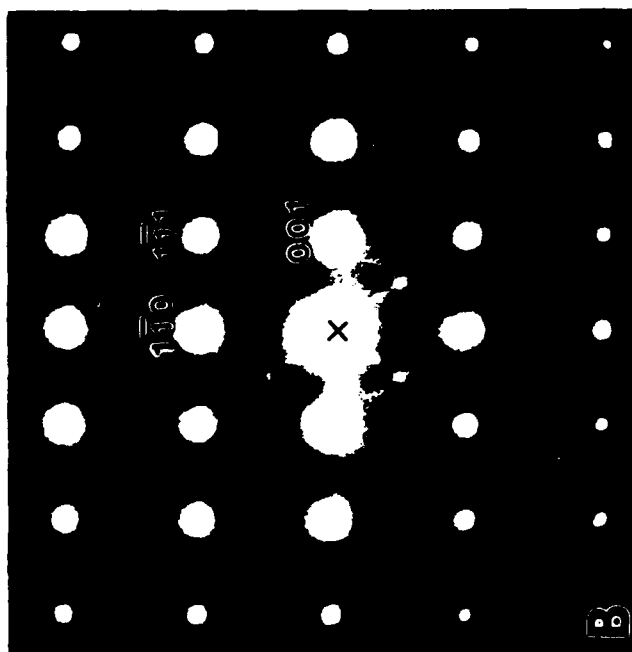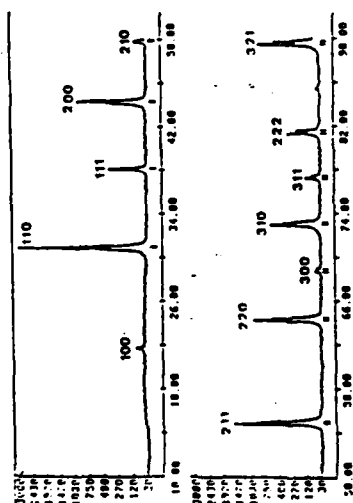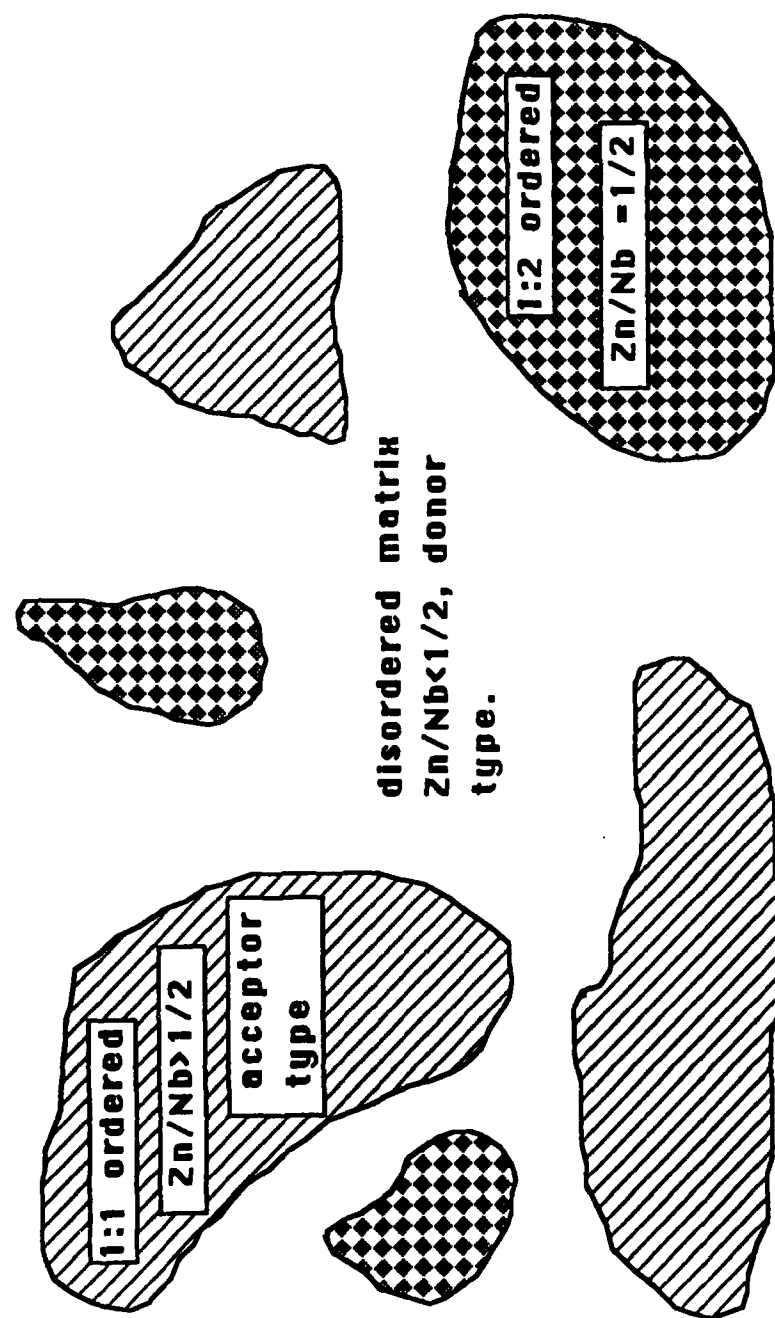
Fig. 1
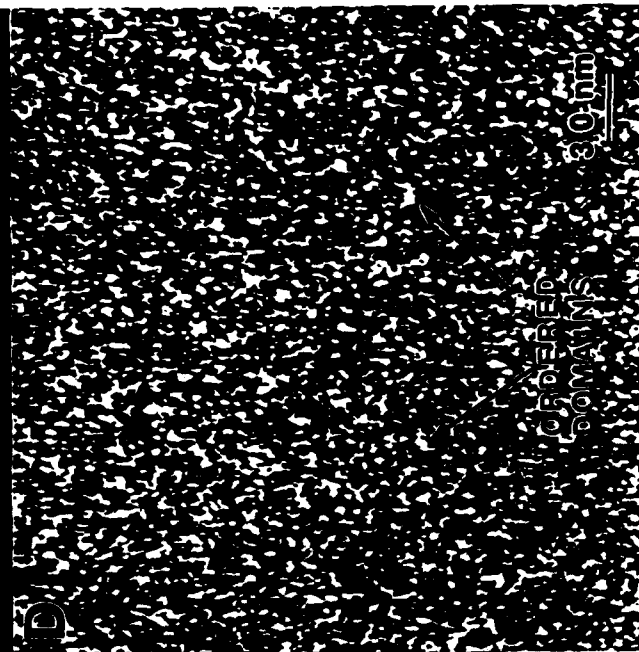
ABO₃

A(B'₁/₂B''₁/₂)O₃   A(B'₁/₃B''₂/₃)O₃

ABO₃

1:1   1:2

disordered

A   B   O

⟨111⟩   {111}

For A(B'B'')O₃ :   ● B(disordered)   ⊕ B'   ○ B''

disordered matrix Zn/Nb<1/2, donor type.

1:2 ordered
Zn/Nb =1/2

1:1 ordered
Zn/Nb>1/2
acceptor type

Fig 3

Fig 5

BF

A

300 nm

CDF

APB's

300 nm

B

Fig 8

a

10 μm

b

Fig. 9

variant: + 1   ▪ 2   □ 3   * 4

Fig 12

ORDERED
DOMAINS

10·nm

0.409nm

0.289nm
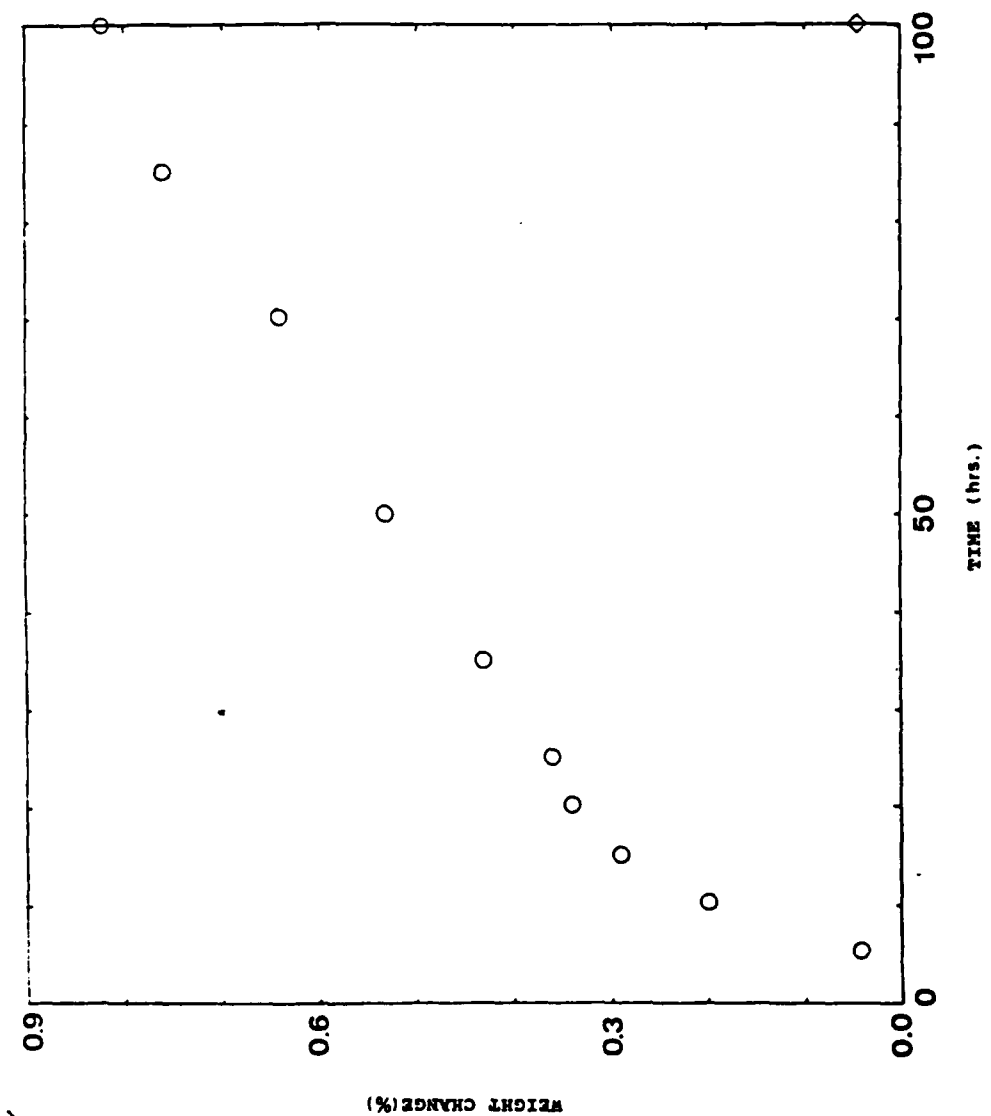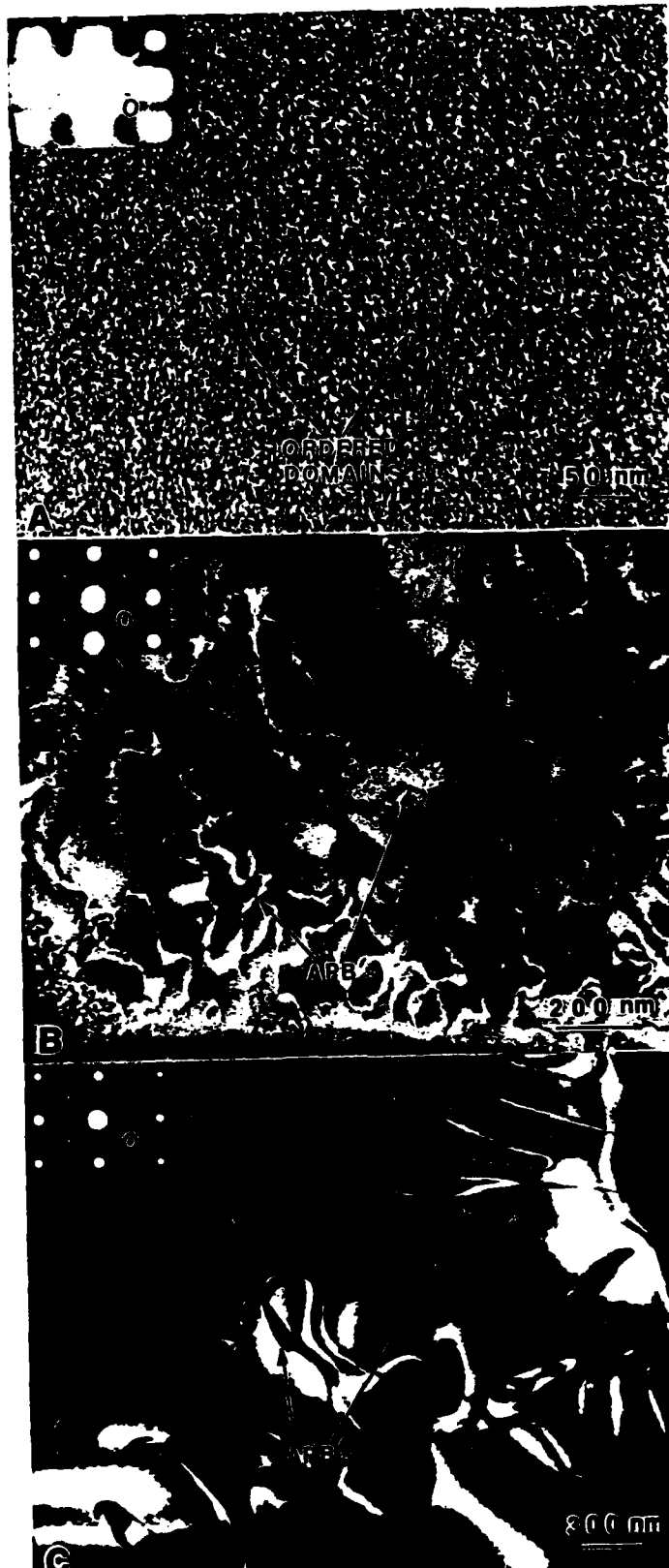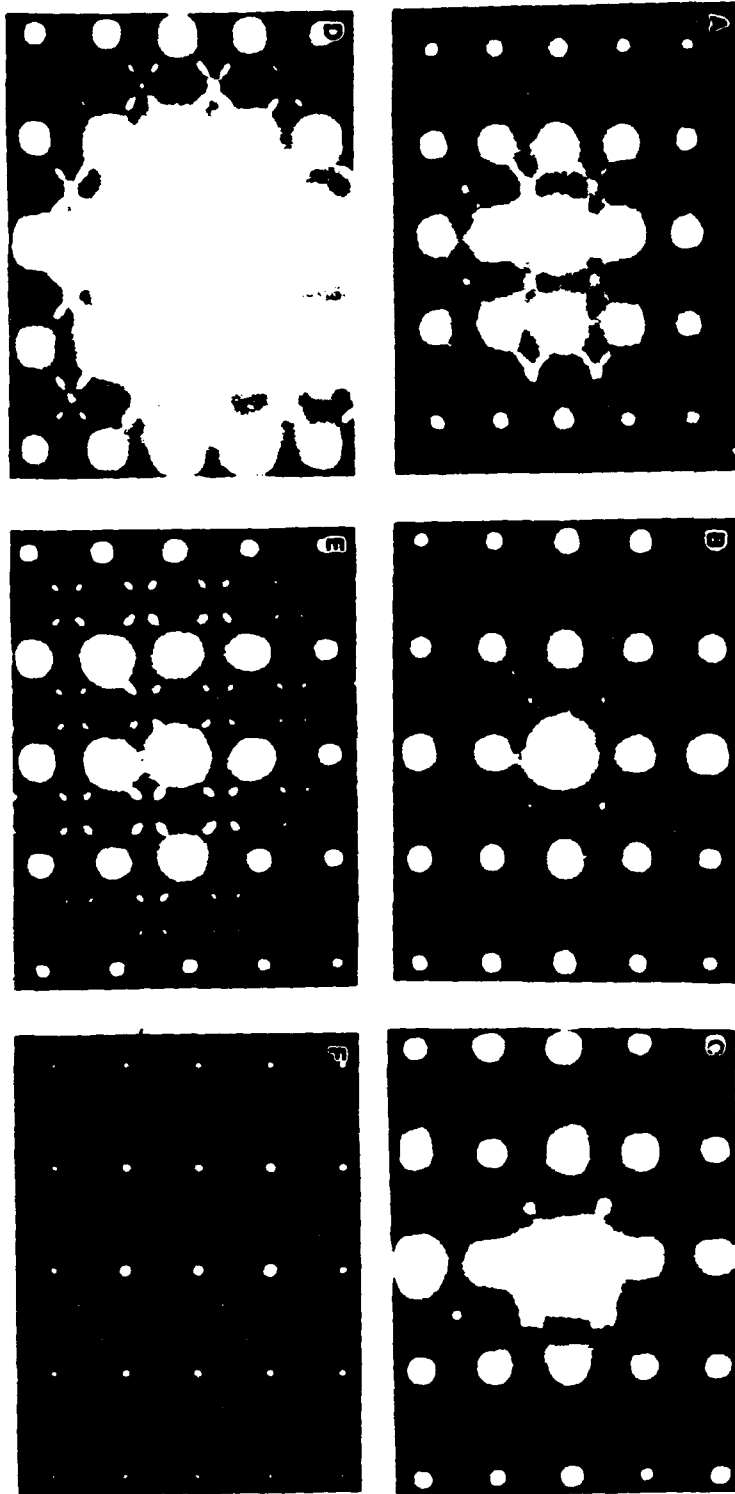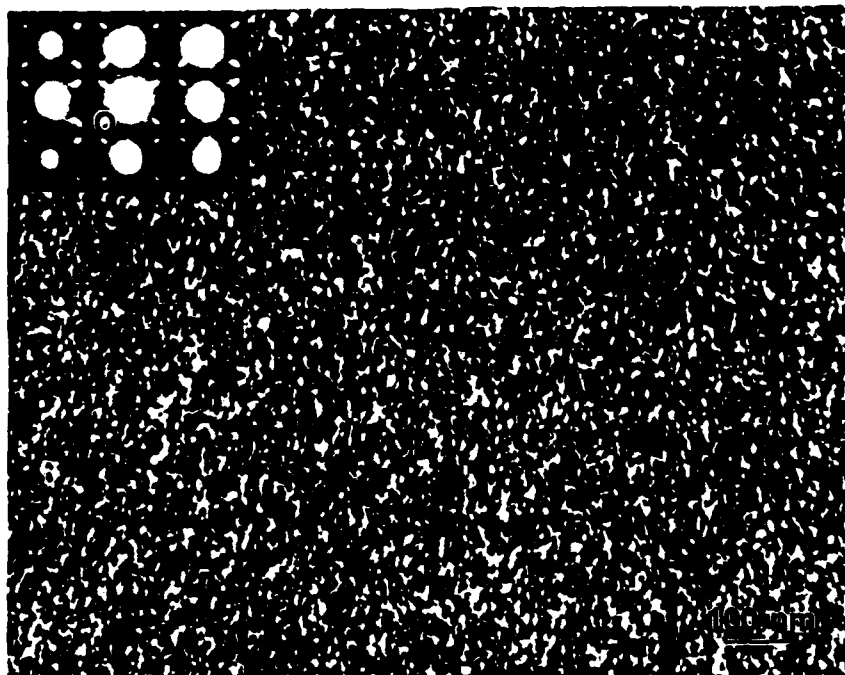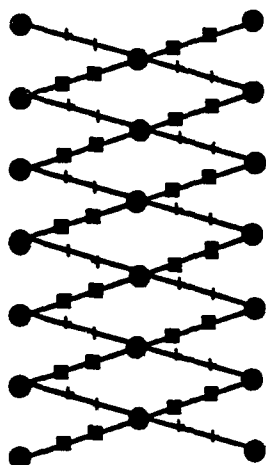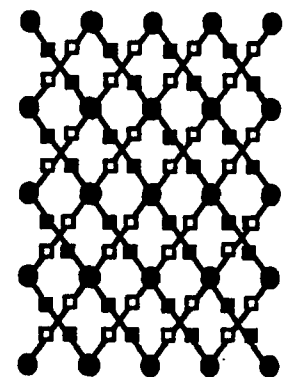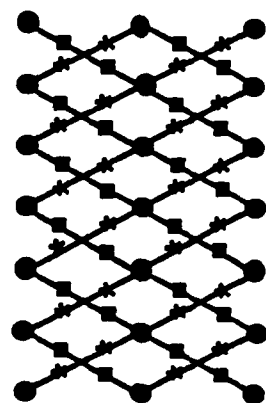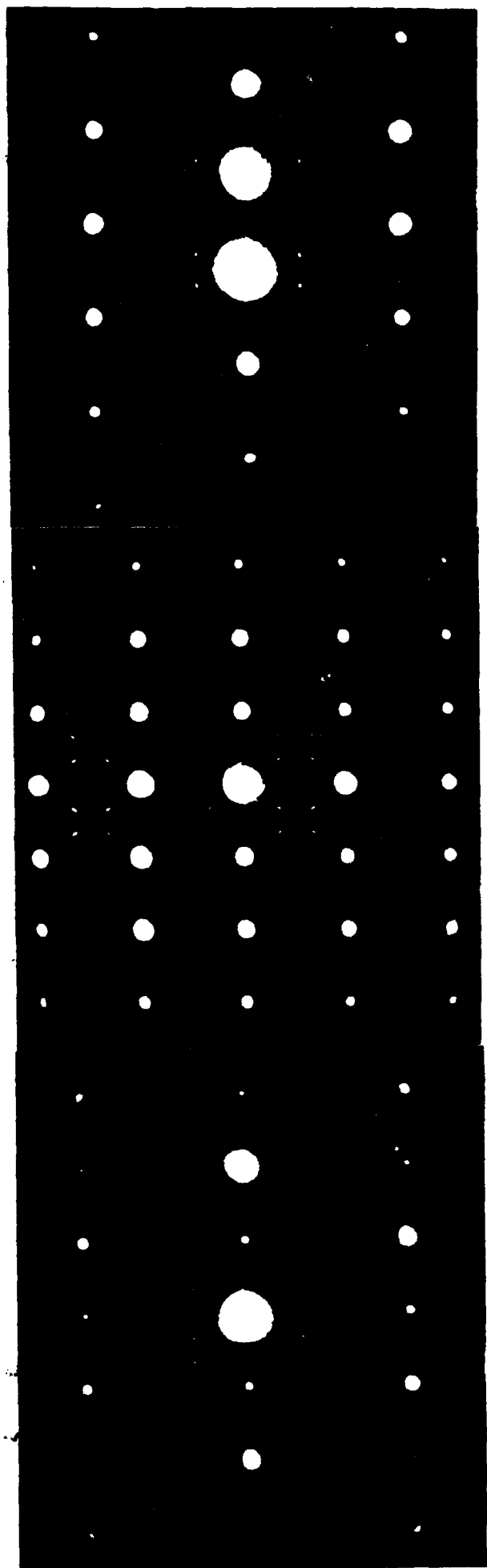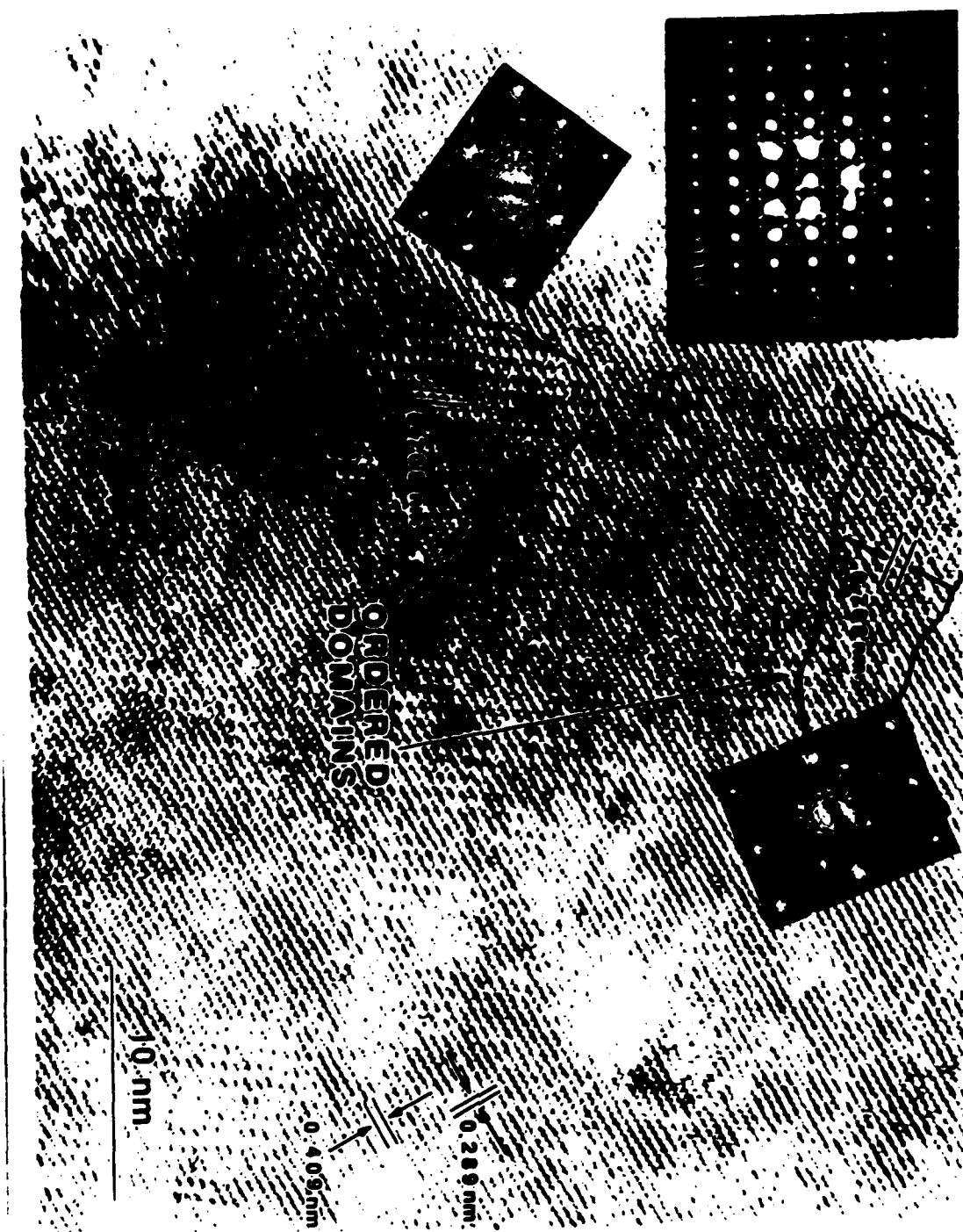
<u>TEM of the Relaxor Material $Pb(Sc_{0.5}Ta_{0.5})O_3$</u>

H. M. Chan and M. P. Harmer

Lehigh University, Bethlehem, PA 18015

A. Bhalla and L. E. Cross

Pennsylvania State University, University Park, PA 16802

Abstract

The transmission electron microscope (TEM) was used to directly observe ordered microdomains in $Pb(Sc_{0.5}Ta_{0.5})O_3$ (PST). The microstructure of both single crystal and polycrystalline PST was studied as a function of S, the degree of order (which was controlled by thermal treatment). The observed domain sizes were in good agreement with the results of prior x-ray studies. It was found that the domain coarsening kinetics are much slower for the single crystal than the polycrystalline material. Also evidence was obtained for the presence of short range order within PST.

Introduction

Lead scandium tantalate $Pb(Sc_{0.5}Ta_{0.5})O_3$ is one of a number of ferroelectric compounds which exhibit so-called "relaxor behavior" i.e., these materials show a broad dielectric permittivity versus temperature peak, and dielectric dispersion at low frequencies. It has been postulated[1-3] that this type of behavior is due to the presence of microscopic regions within the material which are of slightly differing compositions (and hence Curie temperatures).

Setter and Cross investigated this model by studying the behavior of lead scandium tantalate (PST).[4,5] This material is particularly suited to this type of study because the degree of order of the B-site cations (Sc^{2+} and Ta^{5+}) can be controlled by thermal treatment. The structure of fully ordered PST is shown in Figure 1; it can be seen that the Sc^{2+} and Ta^{5+} ions adopt a NaCl type structure on the B-site sublattice. Setter and Cross showed that in the disordered state, PST exhibited classic relaxor behavior. On ordering however, a pronounced sharpening of the permittivity versus temperature curves took place, thus supporting the model that the relaxor behavior is caused by chemical inhomogeneity on a nanoscopic scale.

Until very recently, evidence for the existence of ordered microdomains within PST has been indirect.[4] Harmer et al.[6] were the first workers to directly observe ordered microdomains in PST using the transmission electron microscope (TEM). The scale of the ordered structures was found to be of the order of 35-120 nm, which was in good agreement with the earlier x-ray results. A particularly interesting result from the study of Setter and Cross[5] was the difference in domain coarsening behavior exhibited by the single crystal and polycrystalline PST. On annealing the polycrystalline (ceramic) PST, the degree of order increased, and there was a corresponding increase in the size of the ordered domains (as determined by x-ray line broadening measurements). For the single crystal however, even for relatively high degrees of order ($\sim$80%), the domain size was determined to be <100Å. The purpose of this study, therefore, was to use the TEM to directly examine the ordered domain configurations for both single crystal and ceramic PST, as a function of annealing conditions. In this way, it was hoped to gain a better understanding of the microstructure/property

relationships in this system.

Experimental

The techniques used to prepare the PST single crystals[4] and polycrystalline sintered pellets[5] have been described in detail elsewhere. The samples studied, together with the corresponding heat-treatments are summarized in Table I. Lead loss during the annealing treatments was minimized by surrounding the specimens with a $PbZrO_3$-20 wt% PbO mixture. Thin foil TEM specimens were prepared by polishing down to $\sim$30 μm, and

argon-ion-beam thinning using 6 kV argon ions incident 15° to the foil plane. To prevent lead evaporation during ion-beam milling, a liquid-N_2 cooled cold stage was used.

From Figure 1 it can be seen that there is an effective doubling of the unit cell parameters when PST goes from the disordered to the ordered state. The effect of this on the observed reflections in the electron diffraction pattern is shown in Table II. The $(100)_s$* and $(110)_s$ super-lattice reflections are forbidden due to structure factor considerations, however the $(111)_s$ is allowed. It is this reflection therefore which can be used to image the ordered domains in dark field.

Results

Single Crystal

i) As grown (S = 0.8)

Figure 2 shows a centered dark-field micrograph of the as grown single crystal taken using the $(111)_s$ reflection. The bright regions are the ordered microdomains; the matrix (dark contrast) is disordered. The domain size was of the order 100-600Å. When this structure was annealed for 24 hrs. at 1000°C, no

---

*Indexed using the ordered unit cell.

coarsening of the domains was observed, and the microstructure remained for the most part unchanged. This is in direct contrast to the behavior of the polycrystal which is discussed in a later section. Figure 2 is representative of the structure observed in the majority of the areas studied. In some isolated regions of the sample however, domains more resembling those reported by Harmer et al.[6] were observed. The reason for this variation in structure is unclear. It may be related to local variations in the degree of order occurring during the growth process.

ii) S = 0.35

The degree of order of the as grown single crystal was relatively high. Disordering can be achieved however by annealing for 1 hr. at $1400^{O}C$, and air quenching. The resulting structure was very similar to that shown in Figure 2. Despite the lower degree of order, ordered microdomains are still visible, the scale of the domains being similar to those of the "as grown" state.

Polycrystal

i) As sintered (S = 0.34)

In the as sintered state, the degree of order is relatively low. Ordered microdomains $\sim 200\overset{O}{A}$ in diameter were observed, and the overall microstructure resembled that of the single crystal.

ii) Annealed at $1000^{O}C$ (S = 0.86)

After annealing for 30 hrs. at $1000^{O}C$, the structure underwent considerable coarsening as can be seen in Figure 3. The wavy boundaries seen separating the domains are anti-phase domain boundaries (APB's). An APB is characterized by a disruption in the correct ordering sequence, and separates two fully ordered regions.[8] The observed domain size varied widely from $\sim 200\overset{O}{A}$ to over $4000\overset{O}{A}$. A similar structure was observed

after annealing for only 2 hrs. at 1000°C, except in this case the maximum observed domain size was ∿2000Å. This result confirms that coarsening of the domain structure occurs much more rapidly in the polycrystal than in the single crystal, and possible reasons for this will be discussed later.

Anomalous (110)$_s$ Reflection

As discussed previously, for the ordered NaCl structure, the (110)$_s$ superlattice reflection is forbidden due to structure factor considerations. Faint (110)$_s$ reflections were observed, however, for both single crystal and ceramic PST (Figure 4). The possible origin of this anomalous (110)$_s$ reflection will be discussed more fully in the next section.

Discussion

Single Crystal

For both the disordered (S = 0.35) and ordered (S = 0.8) single crystal, dark field imaging showed the structure to consist of ordered microdomains (200-600Å) within a disordered matrix. At first sight, the lack of dependence of the ordered domain size or density on the overall degree of order is difficult to understand. It should be remembered however that S (the degree of order) was estimated by ratioing the intensity of the (111)$_s$ x-ray reflection to that of the (200)$_s$. The value of S obtained is thus an average for the whole specimen. The dark field imaging technique however only detects those volumes of material where the intensity of the (111)$_s$ is sufficient to produce an image in reasonable exposure times. Thus the x-ray and TEM techniques are measuring slightly different quantities, and in general one would expect the x-ray technique to give the higher value of S. Another factor which must be taken into consideration is the possibility of partial, short-range ordering (SRO). This is intermediate between disordered and fully

ordered, and represents the stage where there is a marked preference for the B-site ions to have unlike neighbors, but the ordering extends over several unit cells only. This could account for the speckled contrast observed within the ordered domains.[9]

Polycrystalline PST

The ordered domain structure for the polycrystal (annealed 30 hrs. at $1000^\circ C$) is similar to that observed by Chang and Chen[10], however these workers did not state whether they were studying single or polycrystalline material, or the nature of the heat treatments carried out (if any). For the type of order occurring in PST, there is one unique type of APB whose anti-phase vector can be defined as 1/2 [001]. For this reason, no APB triple points can occur, and it is impossible to form a stable foam-like structure. Coarsening usually occurs readily for this type of APB configuration, and this was observed to be the case for the ceramic PST.

The reason for the lack of domain coarsening in the single crystal is not clear. One possibility is that it is related to differences in chemistry between the two samples, since the preparation techniques for the single crystal and polycrystal were completely distinct. If there is an excess of one of the B-site cations for example, this may have a stabilizing influence on a particular domain configuration.[12]

Anomalous $(110)_s$ Reflection

A series of experiments were carried out in order to determine the origin of the anomalous reflection $(110)_s$. The results were as follows:

a) It was determined that the $(110)_s$ reflection was not a thinning artefact, as the reflection was observed

in thin specimens produced by crushing, as well as in ion-beam thinned samples.

b) It was shown to be unlikely that the $(110)_s$ reflection was the result of beam damage, because the d-spacing did not correspond to any reflections previously obtained from heavily damaged areas.

c) The $(110)_s$ reflection was determined not to originate from the APB's, since the reflection was observed even for selected area diffraction patterns taken from within a single domain.

Taking into account the above evidence, it is postulated that the observed $(110)_s$ reflections are the result of small regions within the crystal which have a type of order different from the NaCl structure. These regions could occur in either conventionally ordered or disordered regions of the crystal. Unfortunately this model is difficult to test because the diffuseness of these reflections made dark-field imaging of these regions impractical.

Summary

Dark field imaging has been used to directly observe ordered microdomains in $Pb(Sc_{0.5}Ta_{0.5})O_3$. The size of the microdomains was in good agreement with the results of earlier x-ray determinations. The domain coarsening kinetics were much slower for the single crystal. Evidence has been obtained for the presence of short range order within PST. This study has focussed on the microstructural features of the ordered domains. These results will be presented more fully, together with the corresponding dielectric data, in a separate paper.

Acknowledgement

References

1) V.A.Isupov: Sov. Phys.-Tech. Phys. 1 (1956) 1846.

2) B.N.Rolov: Sov. Phys. Solid State 6 (1965) 1676.

3) V.V.Kirillov and V.A.Isupov: Ferroelectrics 5 (1973) 3.

4) N.Setter and L.E.Cross: J. Mat. Sci. 15 (1980) 2478.

5) N.Setter and L.E.Cross: J. Appl. Phys. 51 (1980) 4356.

6) M.P.Harmer, A.Bhalla, B.Fox and L.E.Cross: Mat. Letters
   2 (1984) 278.

7) N.Setter and L.E.Cross: J. Crystal Growth 50 (1980) 555.

8) D.A.Porter and K.E.Easterling: Phase Transformations in
   Metals and Alloys (Van Nostrand Reinhold (UK) Co. Ltd.,
   1982) 3rd ed. p. 358.

9) J-P.A.A.Chevalier and W.M.Stobbs: Proc.6thEur.Congr. on
   Electron Micros., Jerusalem, 1976.

10) Y.J.Chang and Z.L.Chen: Ferroelectrics Letters 4 (1985) 13.

11) F.S.Galasso: Structure, Properties and Preparation of
    Perovskite-type Compounds (Pergamon, New York, 1969).

12) C.L.Rase and D.E.Mikkola: Met. Trans. 6A (1975) 2267.

Figure Captions

1. Structure of ordered perovskite $Pb(Sc_{0.5}Ta_{0.5})O_3$ (after Galasso[11]).

2. Single crystal, as grown. CDF micrograph, bright regions are ordered microdomains.

3. Polycrystal, annealed 30 hrs. at $1000^\circ C$.

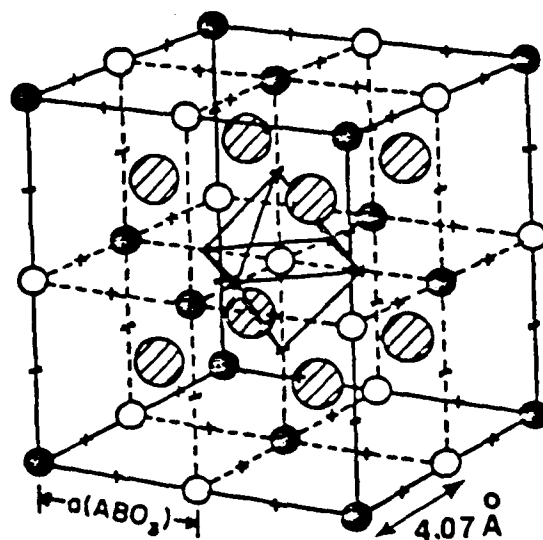4. $[1\bar{2}1]$ diffraction pattern, note diffuse (110) reflections.

Table I

PST		Heat Treatment	Degree of Order
Single Crystal	a)	As-grown	0.8
	b)	Annealed 24 hrs. 1000°C	0.8
	c)	1 hr. 1400°C air quenched	0.35
Polycrystal	a)	As sintered	0.37
	b)	2 hrs. 1000°C	0.86
	c)	30 hrs. 1000°C	0.86

Table II

Disordered			Ordered (NaCl structure)				d-spacing (Å)
h	k	ℓ		h	k	ℓ	
---			F	1	0	0	8.14
---			F	1	1	0	5.76
---				1	1	1	4.70
1	0	0		2	0	0	4.07
1	1	0		2	2	0	2.88

F = forbidden reflection

$\square$ = Pb ● = Sc ◯ = Ta × = O

1000 Å

3

APB

0.1µm

4

$[10\bar{1}]_s$

S
+   O   +
000   111   222

+   O   +
$20\bar{2}$ 420

Section II

FERROELECTRIC DOMAINS

MICROSTRUCTURES OF HIGH DIELECTRIC CONSTANT MATERIALS

Helen M. Chan* and Martin P. Harmer

Department of Materials Science and Engineering
and Materials Research Center, Lehigh University
Bethlehem, PA 18015 U.S.A.

ABSTRACT

A brief overview is given of the important microstructural characteristics of several classes of high dielectric constant ceramics. Attention is focussed on the understanding of ferroelectric domain structures in $BaTiO_3$, the effect of grain size on the dielectric constant in $BaTiO_3$, and the microstructure and microchemistry of so-called "relaxor" ferroelectrics. The relaxor families discussed in particular are $Pb(Sc_{1/2}Ta_{1/2})O_3$, $Pb(Mg_{1/3}Nb_{2/3})O_3$ and $Pb(Zn_{1/3}Nb_{2/3})O_3$. The nature of the B-site cation ordering and the ferroelectric domain structures of these materials are discussed in some detail.

INTRODUCTION

The microstructure and microchemistry of high dielectric constant materials have a profound influence on their dielectric properties (1,2). Because of the commercial importance of these materials, it is necessary to fully understand their microstructure-property relationships, particularly if optimum processing is to be achieved. Interfaces such as grain boundaries, ferroelectric domain boundaries, and antiphase domain boundaries (APBs) can play an important role in determining the material's behavior. This is an extensive topic, and clearly it would be impractical to attempt to cover it exhaustively. Instead, the approach taken will be to focus on areas of particular interest, and to highlight areas where significant advances have been made, and/or where more work needs to be done. The high permittivity materials we will concentrate on are $BaTiO_3$, and various members of the so-called "relaxor" family of ferroelectrics.

---

*Currently on leave of absence at National Bureau of Standards, Gaithersburg, MD 20899.

Ferroelectric Domain Structure

On cooling below the so-called Curie temperature (T_c=130°C), $BaTiO_3$ undergoes a phase transition from the cubic paraelectric phase to the tetragonal ferroelectric phase (3) (Figure 1). In the tetragonal unit cell (c/a ≈ 1.01), the polarization vector is parallel to the long c-axis, and a domain represents a region within the crystal where the polarization direction is uniform. In $BaTiO_3$, there are two types of domain boundaries, namely 90° and 180°, where the angle describes the change in direction of the polarization vector across the boundary. Figure 2 shows a TEM micrograph of 90° boundaries; the domain boundaries lie on (110) planes. Since changes in the bulk polarization of $BaTiO_3$ occur by domain boundary motion, the boundary structure determines such properties as aging and dielectric losses (4).

Much of the initial characterization of the basic crystallography of domain boundaries was carried out using polarization light microscopy. More recently, the transmission electron microscope has proved to be a powerful tool (5-7) because of the much higher spatial resolution, and the ability to obtain exact crystallographic information from selected areas of the specimen. In particular, a recent study by Hu et al. (7) revealed the existence of an "unconventional" 90° domain which had not previously been reported (this domain configuration is shown schematically in figure 3). Although the major features of domain boundaries are now well-known, there still remains some uncertainty over the width of the boundary region (6). Using high resolution transmission electron microscopy (HRTEM), it was possible to directly observe the bending of the (100) planes across a 90° domain boundary (see figure 4). This bending took place gradually over several tens of unit cell lengths. It would be of great interest to carry out a systematic study of domain width as a function of c/a (which could be controlled by dopant type and concentration). The lower the c/a ratio, the less the distortion will be at the boundary, and this would be expected to influence both the equilibrium domain size, and the boundary width.
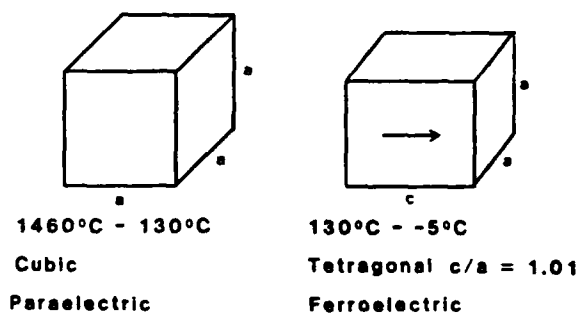
1460°C - 130°C   130°C - -5°C

Cubic   Tetragonal c/a = 1.01

Paraelectric   Ferroelectric

Fig. 1. On cooling below 130°C (Curie temperature) $BaTiO_3$ undergoes a cubic to tetragonal phase change.

Fig. 2.   TEM micrograph of 90° domains.   Boundary planes
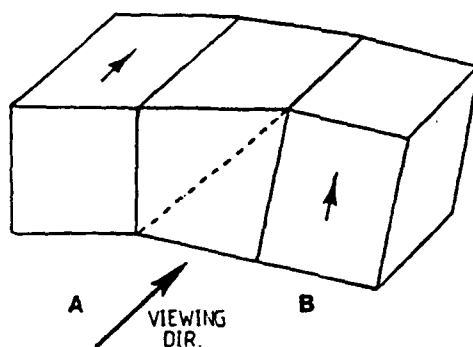lie on (110).

A   B
VIEWING
DIR.

Fig. 3.   Schematic representation of unconventional 90° domain
configuration.   (For the conventional 90° domain boundary, the
polarization vectors of both domains lie in the plane perpendicular to the
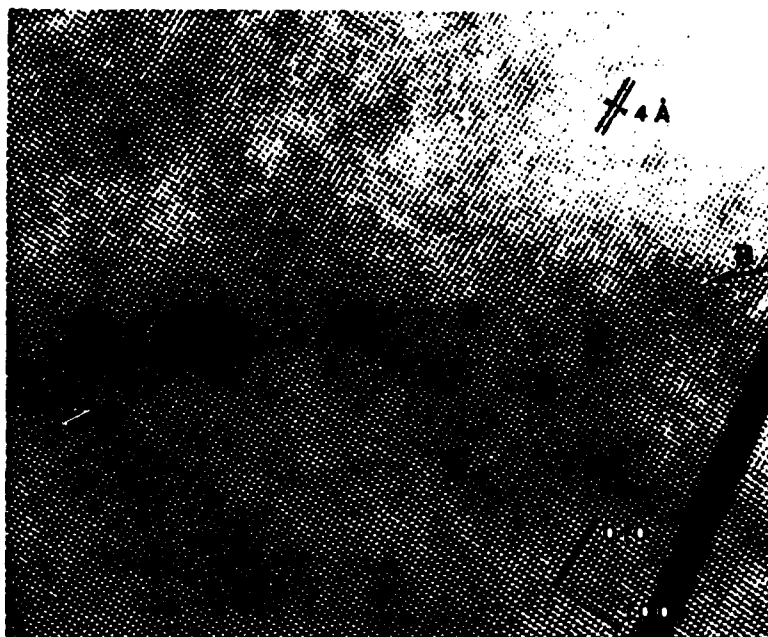viewing direction.)

Fig. 4. HRTEM micrograph across 90° boundary in 0.5 mol%
Nb doped BaTiO$_3$. Trace of boundary lies along AB.
Note bending of (100) planes across boundary region.

Grain Size Effect

It has been observed by several workers (8-10) that the permittivity
of polycrystalline BaTiO$_3$ (at temperatures below the Curie temperature)
initially increases with decreasing grain size. As the grain size
decreases still further, however, the permittivity falls sharply. The
grain size at which the maximum dielectric constant occurs is $\approx$ 1 μm.
Until recently, the model which has been most accepted in explaining this
interesting effect is that due to Buessem et al. (11). It has been
postulated that ferroelectric domains have a minimum size of $\approx$1 μm;
therefore, at grain sizes below this, each grain consists essentially of
only one domain. Thus on cooling through the Curie temperature, internal
stress generated by the cubic to tetragonal phase change cannot be
relieved by the formation of domain boundaries. Using the Devonshire
theory, it can be shown (11) that internal stress should give rise to an
increase in the permittivity. The chief discrepancy with this model is
that domains of less than 1 μm in width have been observed by several
workers (7,10). An alternative model proposed by Alt, et al. (10)
explains the effect in terms of the increased contribution of the domain
boundaries to the total permittivity. These workers were able to show
that the equilibrium domain width (derived by minimizing the sum of the
domain wall, electrical and mechanical energies), was proportional to the
square root of the grain size. It follows, therefore, that at small grain
sizes, the domains are narrower, hence there is a greater contribution of
the domain boundaries to the permittivity. At very fine grain sizes
however (<0.3 μm), the fall in permittivity was attributed to a change in
crystal structure from tetragonal to pseudocubic.

Another important phenomenon which is related to the grain size in $BaTiO_3$ is the positive temperature coefficient of the resistivity (PTCR) effect (12,13). This is where the resistivity increases by several orders of magnitude on heating in the temperature range above the Curie temperature. This effect occurs in n-type $BaTiO_3$, and is caused by the development of insulating layers of material at the grain boundaries, due to compensation by acceptor states. The grain cores, however, remain semi-conducting.

RELAXOR FERROELECTRICS

There is currently a great deal of interest in the so-called "relaxor" ferroelectrics because of their high dielectric and electrostrictive constants, and relatively low firing temperatures. Relaxors are characterized by a very broad dielectric constant against temperature curve, and dielectric dispersion at low frequencies. Discussion of the influence of microstructure on the properties of relaxors will be divided into the following topics: i) ordering, ii) ferroelectric domains and iii) grain boundary phases. The material compositions discussed are listed in Table 1.

Table 1

Material	
PST	$Pb(Sc_{1/2}Ta_{1/2})O_3$
PMN	$Pb(Mg_{1/3}Nb_{2/3})O_3$
PMN:PT	$Pb(Mg_{1/3}Nb_{2/3})O_3.10$ vol%$PbTiO_3$
PZN:PT	$Pb(Zn_{1/3}Nb_{2/3})O_3.10$ vol%$PbTiO_3$

Ordering

Relaxor compositions invariably consist of structures where there are two or more types of ions on at least one of the cation sublattices. From their work on PST ($Pb(Sc_{1/2}Ta_{1/2})O_3$), Setter and Cross (14) showed that relaxor behavior is directly linked to chemical inhomogeneously on a nonoscopic scale. This inhomogeneity is related to the degree of disorder of Sc^{3+} and Ta^{5+} on the B-sites. These workers observed that if PST is heat-treated so as to achieve NaCl-type ordering of the Sc^{3+} and Ta^{5+} ions, the material behaves like a conventional ferroelectric. Transmission electron microscopy by Harmer et al. (15) and Chan et al. (16) confirmed the existence of ordered domains in both single crystal and polycrystalline PST. Recently, electron diffraction evidence was obtained which suggested that the Mg^{2+} and Nb^{5+} ions in PMN ($Pb(Mg_{1/3}Nb_{2/3})O_3$) undergo a similar type of microchemical ordering (see figure 5). The observation that the Mg^{2+} and Nb^{5+} ions might choose to order in a 1:1 ratio was somewhat surprising, particularly since to preserve stoichiometry, the regions between the domains would have to be Nb rich. This means that the ordered domains are in fact acceptor type island regions in a donor-type matrix. The resulting charge separation would limit the domains to small sizes, consistent with the observations. An alternative interpretation of our results is that the $(\frac{1}{2} \frac{1}{2} \frac{1}{2})$ superlattice reflection is due to a type of ordering that is not of the NaCl-type. In order to test our model, a sample was made up of composition $Pb_{0.9}La_{0.1}Mg_{.3667}Nb_{.6333}O_3$. This composition was chosen so that the La^{3+} ions (which occupy A-sites), exactly compensate for the excess magnesium. It can be seen that the Mg:Nb ratio in this sample is 0.58, as compared to 0.50 in PMN. This composition favors therefore any tendency of the
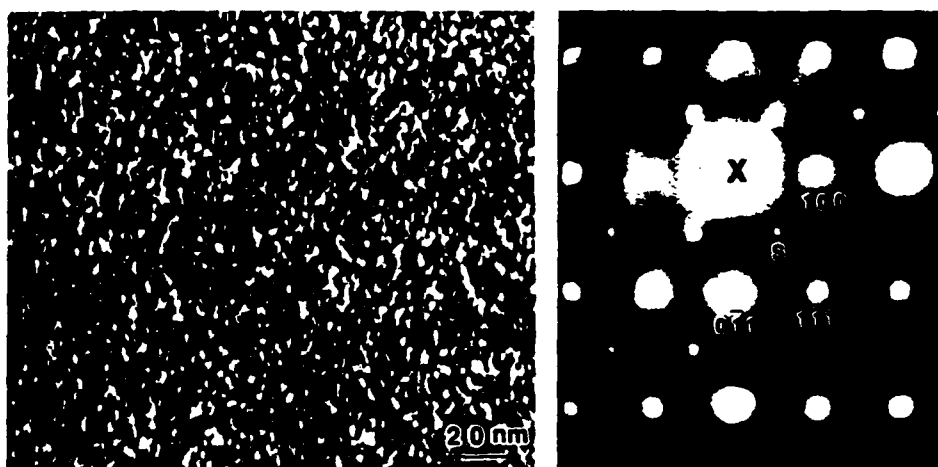
Fig. 5. a) Dark field micrograph of ordered domains in $Pb(Mg_{1/3}Nb_{2/3})O_3$ imaged using superlattice reflection $(\frac{1}{2} \frac{1}{2} \frac{1}{2})$. b) [110] diffraction pattern. (Courtesy J. Chen)

Mg^{2+} and Nb^{5+} to order on a one to one basis. Transmission electron microscopy revealed that regions of this sample were indeed more strongly ordered than PMN--note the high intensity of the $(\frac{1}{2} \frac{1}{2} \frac{1}{2})$ superlattice reflection (figure 6). Although this result supports the 1:1 ordering model, clearly more work needs to be done to prove conclusively whether this model is correct. One possible way to verify our model would be to compare the Mg/Nb ratios in the ordered and disordered regions using microanalysis in the transmission electron microscope.

Ferroelectric Domains

Until now, there have been very few studies of ferroelectric domains in relaxor materials using the TEM (17-19). As will be seen later, one possible reason for this is that domain structures usually develop only at low temperatures, hence a cooling holder is required. In our work, we examined single crystal and polycrystalline PMN:PT, and single crystal PZN:PT, both at room temperature and at temperatures down to -185°C in the TEM. For the PMN:PT, no domain contrast was observed at room temperature. On cooling in-situ in the TEM (see figure 7), the temperature at which the domains first appeared was -120°C. The crystallography of the domain boundaries was found to be consistent with that of the rhombohedral structure, i.e. the boundary planes were parallel to the (100) and (110) planes. (These correspond to 70° and 109° boundaries, respectively.) The diffraction patterns, however, were pseudocubic, and no spot splitting was observed for patterns taken across a domain boundary. In addition, low temperature precision x-ray diffraction work did not reveal any splitting of the (111) peak, although this splitting would be expected for a cubic to rhombohedral transition. Knowing the sensitivity of the x-ray technique, it was estimated that the angle α in the rhombohedral unit cell was $89.95° \lesssim \alpha \lesssim 90°$.
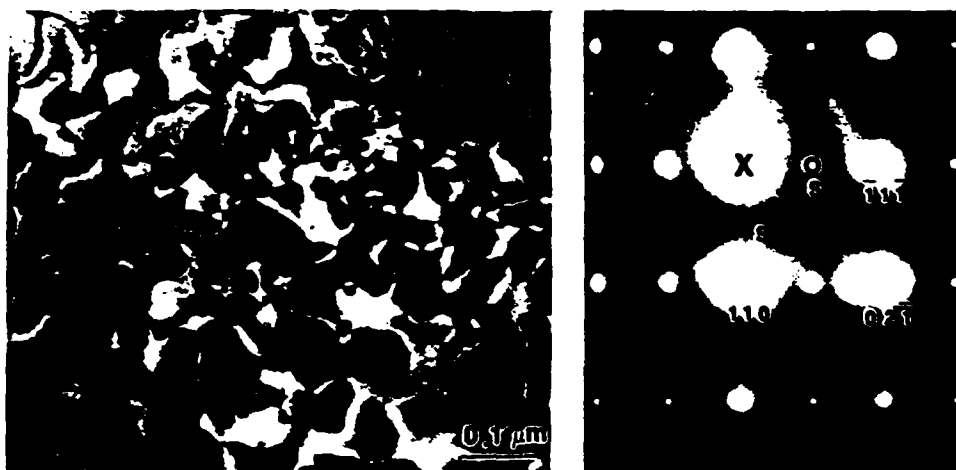
Fig. 6. a) Dark field image showing antiphase domain boundaries in
ordered region of $Pb_{0.9}La_{0.1}Mg_{.3667}Nb_{.6333}O_3$. b) Diffraction pattern.
(Courtesy J. Chen)

Fig. 7. TEM micrograph of ferroelectric domains
in $Pb(Mg_{1/3}Nb_{2/3})O_3.10\%PbTiO_3$. Temperature = -185°C.

For the PZN:PT, ferroelectric domains were visible both at room
temperature and -185°C (see figure 8). As in the case of PMN, the domain
configurations were consistent with the rhombohedral structure, and this
agrees with the results of Kuwata et al. (20). Comparison of figures 7
and 8 shows that the domain width in PZN:PT ($\leq$10nm) is significantly less
than that of PMN:PT.

Fig. 8. TEM micrograph showing ferroelectric aomains in PZN:PT, room temperature.

One model of relaxor behavior is that at room temperature, the ferroelectric domains are very small (100-200Å), and are dynamic, i.e. constantly switching in direction due to thermal aggitation. For the PMN:PT, our observation of macrodomains at low temperatures can be interpreted as the "freezing in" and coalescence of these polar microdomains with decreasing temperature. At room temperature, it is postulated that micropolar domains are present but the frequency of switching is too high for the domains to be observed. The reason then why domains are observed at room temperature in PZN:PT is not well understood, and more work needs to be done in this area.

Grain Boundary Phases

Due to problems with material processing, the full commercial potential of relaxors such as PMN has yet to be realized. Until now, the major problem was thought to be the formation of a pyrochlore phase during processing (21), which was apparently very detrimental to the dielectric properties. Recent results by Chen et al. (22), however, have shown that PMN made from reagent grade starting oxides, contained second phase films over a significant proportion of the grain boundaries (see figure 9). Using x-ray EDS, these films were determined to be rich in lead and phosphorus. When ultra-high purity (99.999%) starting powders were used, the grain boundaries were clean. The ultra-high purity PMN had far superior dielectric properties to the reagent grade PMN, even though it contained a higher volume fraction of the pyrochlore phase. This is very strong evidence that the lower values of dielectric constant measured for reagent grade PMN are due to the presence of impurity derived intergranular phases, rather than the pyrochlore phase itself.

SUMMARY

From the preceding discussion it is clear that a thorough knowledge of the microstructure and chemistry of electronic ceramics is vital to the understanding of their properties. In this regard, modern techniques such as TEM, HRTEM and x-ray EDS have proven extremely valuable.

746

Fig. 9. Grain boundary phase in reagent grade PMN.
(Courtesy J. Chen and A. Gorton)

ACKNOWLEDGEMENTS

REFERENCES

1. "Additives and Interfaces in Electronic Ceramics", Vol. 7, M. F. Yan and A. H. Heuer, eds. Amer. Ceram. Soc. (1983).
2. "Grain Boundary Phenomena in Electronic Ceramics", L. M. Levinson, ed., Amer. Ceram. Soc. (1981).
3. H. D. Megaw, Refinement of the Structure of $BaTiO_3$ and Other Ferroelectrics, Acta Crystallogr. 15:972 (1962).
4. S. I. Kegani and I. Jeda, Mechanism of Ageing in Polycrystalline $BaTiO_3$, J. Phys. Soc. Jpn. 22:725 (1967).
5. V. V. Shakmanov and G. V. Spivak, A Microdiffraction Investigation of the Domain Structure in Barium Titanate Films, Sov. Phys. Solid State 10:802 (1968).
6. T. Malis and H. Gleiter, Investigation of the Structure of Ferroelectric Domain Boundaries by Transmission Electron Microscopy, J. Appl. Phys. 47:5195 (1976).
7. Y. H. Hu, H. M. Chan, X. W. Zhang and M. P. Harmer, Scanning Electron Microscopy and Transmission Electron Microscopy Study of Ferroelectric Domains in Doped $BaTiO_3$, J. Amer. Ceram. Soc. 69 (1986).
8. G. H. Jonker and W. Noorlander, "Science of Ceramics", G. H. Stewart, ed., Academic Press, London (1962).
9. N. C. Sharma and E. R. McCartney, The Dielectric Properties of Pure Barium Titanate as a Function of Grain Size, J. Austr. Ceram. Soc., 10:16 (1974).
10. G. Arlt, D. Hennings and G. deWith, Dielectric Properties of Fine-Grained Barium Titanate Ceramics, J. Appl. Phys. 58:1619 (1985).
11a. W. R. Buessem, L. E. Cross and A. K. Goswami, J. Am. Ceram. Soc., 49:371 (1976).
11b. A. J. Bell, A. J. Moulson and L. E. Cross, The Effect of Grain Size

on the Permittivity of $BaTiO_3$, <u>Ferroelectrics</u> 54:147 (1984).

12. W. Heywang, Barium Titanate as a Semiconductor with Blocking Layers, <u>Solid State Electr.</u>, 3:51 (1961).

13. G. H. Jonker, Equilibrium Barriers in PTC Thermistors, <u>in</u> "Advances in Ceramics", Vol. 7, M. F. Yan and A. H. Heuer, eds., Amer. Ceram. Soc. (1983).

14. N. Setter and L. E. Cross, The Role of B-Site Cation Disorder in Diffuse Phase Transition Behavior of Perovskite Ferroelectrics, <u>J. Appl. Phys.</u>, 51:4356 (1980).

15. M. P. Harmer, A. Bhalla, B. Fox and L. E. Cross, Electron Microscopy of Ordered Domains in Lead Scandium Tantalate, <u>Materials Lettr.</u>, 2:278 (1984).

16. H. M. Chan, M. P. Harmer, A. Bhalla and L. E. Cross, TEM of the Relaxor Material $Pb(Sc_{0.5}Ta_{0.5})O_3$, <u>Jap. J. Appl. Phys.</u>, 24:550 (1985).

17. S. Nomura, M. Endo and F. Kojima, Ferroelectric Domains and Polarization Reversal in $Pb(Zn_{1/3}Nb_{2/3})O_3$ Crystal, <u>Jap. J. Appl. Phys.</u>, 13:2004 (1974).

18. Y. J. Chang and Z. L. Chen, A Study on Ordered Ferroelectric Domains in $Pb(Sc_{1/2}Ta_{1/2})O_3$ Ceramics, <u>Ferroelectrics Lettr.</u> 4:13 (1985).

19. C. A. Randall, D. J. Barber and R. W. Whatmore, A TEM Study of Modified PZT Ferroelectric Ceramics, <u>EMAG '85</u>, Inst. Phys. Conf. Ser. No. 78, Chap. 13 (1985).

20. J. Kuwata, K. Uchino and S. Nomura, Dielectric and Piezoelectric Properties of $0.91Pb(Zn_{1/3}Nb_{2/3})O_3.0.09PbTiO_3$ Single Crystals, <u>Jap. J. Appl. Phys.</u> 21:1298 (1982).

21. S. L. Swartz, T. R. Shrout, W. A. Schulze and L. E. Cross, Dielectric Properties of Lead-Magnesium Niobate Ceramics, <u>J. Am. Ceram. Soc.</u>, 67:311 (1984).

22. J.Chen, A. Gorton, H. M. Chan and M. P. Harmer, Effect of Powder Purity and Second Phases on the Dielectric Properties of Lead Magnesium Niobate Ceramics, <u>J. Am. Ceram. Soc.</u>, in press (1986).

MICROSTRUCTURES OF HIGH DIELECTRIC CONSTANT MATERIALS

Helen M. Chan* and Martin P. Harmer

Department of Materials Science and Engineering
and Materials Research Center, Lehigh University
Bethlehem, PA 18015 U.S.A.

ABSTRACT

A brief overview is given of the important microstructural characteristics of several classes of high dielectric constant ceramics. Attention is focussed on the understanding of ferroelectric domain structures in $BaTiO_3$, the effect of grain size on the dielectric constant in $BaTiO_3$, and the microstructure and microchemistry of so-called "relaxor" ferroelectrics. The relaxor families discussed in particular are $Pb(Sc_{1/2}Ta_{1/2})O_3$, $Pb(Mg_{1/3}Nb_{2/3})O_3$ and $Pb(Zn_{1/3}Nb_{2/3})O_3$. The nature of the B-site cation ordering and the ferroelectric domain structures of these materials are discussed in some detail.

INTRODUCTION

The microstructure and microchemistry of high dielectric constant materials have a profound influence on their dielectric properties (1,2). Because of the commercial importance of these materials, it is necessary to fully understand their microstructure-property relationships, particularly if optimum processing is to be achieved. Interfaces such as grain boundaries, ferroelectric domain boundaries, and antiphase domain boundaries (APBs) can play an important role in determining the material's behavior. This is an extensive topic, and clearly it would be impractical to attempt to cover it exhaustively. Instead, the approach taken will be to focus on areas of particular interest, and to highlight areas where significant advances have been made, and/or where more work needs to be done. The high permittivity materials we will concentrate on are $BaTiO_3$, and various members of the so-called "relaxor" family of ferroelectrics.

---

*Currently on leave of absence at National Bureau of Standards, Gaithersburg, MD 20899.

BARIUM TITANATE

Ferroelectric Domain Structure

On cooling below the so-called Curie temperature (T_c=130°C), $BaTiO_3$ undergoes a phase transition from the cubic paraelectric phase to the tetragonal ferroelectric phase (3) (Figure 1). In the tetragonal unit cell (c/a ≈ 1.01), the polarization vector is parallel to the long c-axis, and a domain represents a region within the crystal where the polarization direction is uniform. In $BaTiO_3$, there are two types of domain boundaries, namely 90° and 180°, where the angle describes the change in direction of the polarization vector across the boundary. Figure 2 shows a TEM micrograph of 90° boundaries; the domain boundaries lie on (110) planes. Since changes in the bulk polarization of $BaTiO_3$ occur by domain boundary motion, the boundary structure determines such properties as aging and dielectric losses (4).

Much of the initial characterization of the basic crystallography of domain boundaries was carried out using polarization light microscopy. More recently, the transmission electron microscope has proved to be a powerful tool (5-7) because of the much higher spatial resolution, and the ability to obtain exact crystallographic information from selected areas of the specimen. In particular, a recent study by Hu et al. (7) revealed the existence of an "unconventional" 90° domain which had not previously been reported (this domain configuration is shown schematically in figure 3). Although the major features of domain boundaries are now well-known, there still remains some uncertainty over the width of the boundary region (6). Using high resolution transmission electron microscopy (HRTEM), it was possible to directly observe the bending of the (100) planes across a 90° domain boundary (see figure 4). This bending took place gradually over several tens of unit cell lengths. It would be of great interest to carry out a systematic study of domain width as a function of c/a (which could be controlled by dopant type and concentration). The lower the c/a ratio, the less the distortion will be at the boundary, and this would be expected to influence both the equilibrium domain size, and the boundary width.
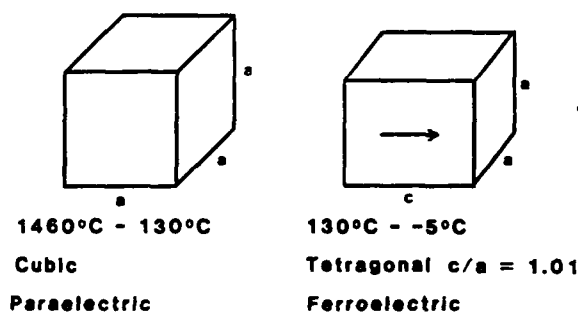

1460°C - 130°C   130°C - -5°C

Cubic   **Tetragonal c/a = 1.01**

Paraelectric   **Ferroelectric**

Fig. 1. On cooling below 130°C (Curie temperature) $BaTiO_3$ undergoes a cubic to tetragonal phase change.

Fig. 2. TEM micrograph of 90° domains. Boundary planes
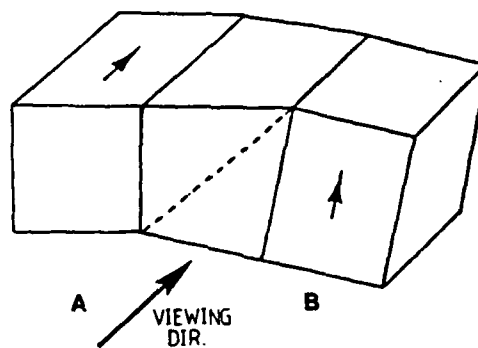lie on (110).

A VIEWING B
DIR.

Fig. 3. Schematic representation of unconventional 90° domain
configuration. (For the conventional 90° domain boundary, the
polarization vectors of both domains lie in the plane perpendicular to the
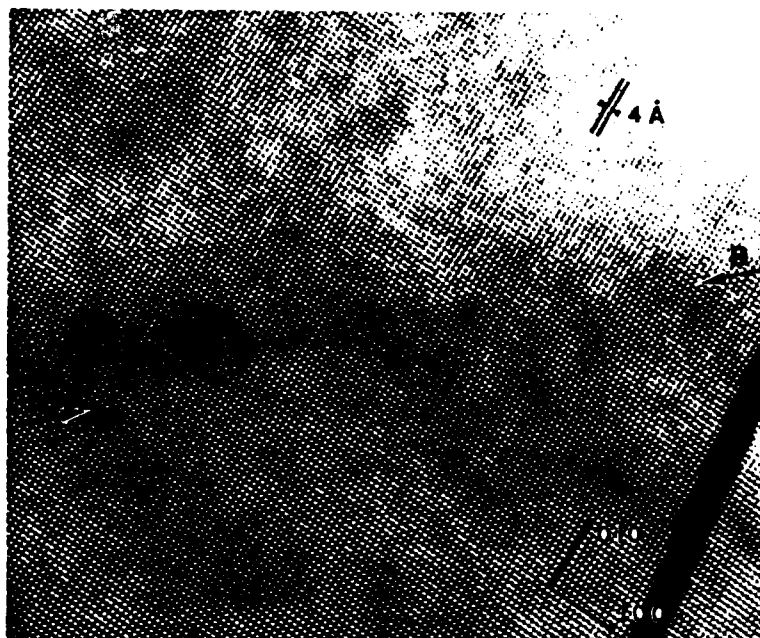viewing direction.)

Fig. 4. HRTEM micrograph across 90° boundary in 0.5 mol%
Nb doped BaTiO$_3$. Trace of boundary lies along AB.
Note bending of (100) planes across boundary region.

Grain Size Effect

It has been observed by several workers (8-10) that the permittivity
of polycrystalline BaTiO$_3$ (at temperatures below the Curie temperature)
initially increases with decreasing grain size. As the grain size
decreases still further, however, the permittivity falls sharply. The
grain size at which the maximum dielectric constant occurs is ≈ 1 μm.
Until recently, the model which has been most accepted in explaining this
interesting effect is that due to Buessem et al. (11). It has been
postulated that ferroelectric domains have a minimum size of ≈1 μm;
therefore, at grain sizes below this, each grain consists essentially of
only one domain. Thus on cooling through the Curie temperature, internal
stress generated by the cubic to tetragonal phase change cannot be
relieved by the formation of domain boundaries. Using the Devonshire
theory, it can be shown (11) that internal stress should give rise to an
increase in the permittivity. The chief discrepancy with this model is
that domains of less than 1 μm in width have been observed by several
workers (7,10). An alternative model proposed by Alt, et al. (10)
explains the effect in terms of the increased contribution of the domain
boundaries to the total permittivity. These workers were able to show
that the equilibrium domain width (derived by minimizing the sum of the
domain wall, electrical and mechanical energies), was proportional to the
square root of the grain size. It follows, therefore, that at small grain
sizes, the domains are narrower, hence there is a greater contribution of
the domain boundaries to the permittivity. At very fine grain sizes
however (<0.3 μm), the fall in permittivity was attributed to a change in
crystal structure from tetragonal to pseudocubic.

742

Another important phenomenon which is related to the grain size in $BaTiO_3$ is the positive temperature coefficient of the resistivity (PTCR) effect (12,13). This is where the resistivity increases by several orders of magnitude on heating in the temperature range above the Curie temperature. This effect occurs in n-type $BaTiO_3$, and is caused by the development of insulating layers of material at the grain boundaries, due to compensation by acceptor states. The grain cores, however, remain semi-conducting.

RELAXOR FERROELECTRICS

There is currently a great deal of interest in the so-called "relaxor" ferroelectrics because of their high dielectric and electrostrictive constants, and relatively low firing temperatures. Relaxors are characterized by a very broad dielectric constant against temperature curve, and dielectric dispersion at low frequencies. Discussion of the influence of microstructure on the properties of relaxors will be divided into the following topics: i) ordering, ii) ferroelectric domains and iii) grain boundary phases. The material compositions discussed are listed in Table 1.

Table 1

Material	
PST	$Pb(Sc_{1/2}Ta_{1/2})O_3$
PMN	$Pb(Mg_{1/3}Nb_{2/3})O_3$
PMN:PT	$Pb(Mg_{1/3}Nb_{2/3})O_3.10$ vol%$PbTiO_3$
PZN:PT	$Pb(Zn_{1/3}Nb_{2/3})O_3.10$ vol%$PbTiO_3$

Ordering

Relaxor compositions invariably consist of structures where there are two or more types of ions on at least one of the cation sublattices. From their work on PST ($Pb(Sc_{1/2}Ta_{1/2})O_3$), Setter and Cross (14) showed that relaxor behavior is directly linked to chemical inhomogeneously on a nonoscopic scale. This inhomogeneity is related to the degree of disorder of Sc^{3+} and Ta^{5+} on the B-sites. These workers observed that if PST is heat-treated so as to achieve NaCl-type ordering of the Sc^{3+} and Ta^{5+} ions, the material behaves like a conventional ferroelectric. Transmission electron microscopy by Harmer et al. (15) and Chan et al. (16) confirmed the existence of ordered domains in both single crystal and polycrystalline PST. Recently, electron diffraction evidence was obtained which suggested that the Mg^{2+} and Nb^{5+} ions in PMN ($Pb(Mg_{1/3}Nb_{2/3})O_3$) undergo a similar type of microchemical ordering (see figure 5). The observation that the Mg^{2+} and Nb^{5+} ions might choose to order in a 1:1 ratio was somewhat surprising, particularly since to preserve stoichiometry, the regions between the domains would have to be Nb rich. This means that the ordered domains are in fact acceptor type island regions in a donor-type matrix. The resulting charge separation would limit the domains to small sizes, consistent with the observations. An alternative interpretation of our results is that the ($\frac{1}{2}$ $\frac{1}{2}$ $\frac{1}{2}$) superlattice reflection is due to a type of ordering that is not of the NaCl-type. In order to test our model, a sample was made up of composition $Pb_{0.9}La_{0.1}Mg_{.3667}Nb_{.6333}O_3$. This composition was chosen so that the La^{3+} ions (which occupy A-sites), exactly compensate for the excess magnesium. It can be seen that the Mg:Nb ratio in this sample is 0.58, as compared to 0.50 in PMN. This composition favors therefore any tendency of the
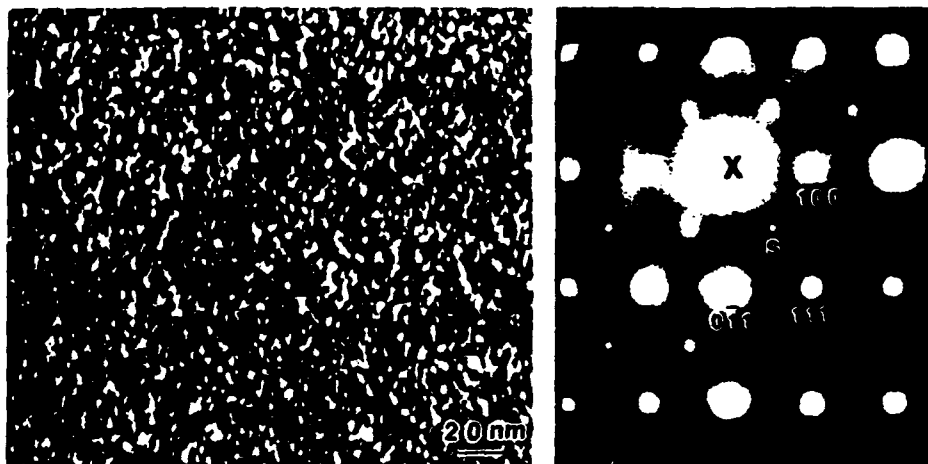
Fig. 5. a) Dark field micrograph of ordered domains in $Pb(Mg_{1/3}Nb_{2/3})O_3$ imaged using superlattice reflection $(\frac{1}{2}\ \frac{1}{2}\ \frac{1}{2})$. b) [110] diffraction pattern. (Courtesy J. Chen)

Mg^{2+} and Nb^{5+} to order on a one to one basis. Transmission electron microscopy revealed that regions of this sample were indeed more strongly ordered than PMN--note the high intensity of the $(\frac{1}{2}\ \frac{1}{2}\ \frac{1}{2})$ superlattice reflection (figure 6). Although this result supports the 1:1 ordering model, clearly more work needs to be done to prove conclusively whether this model is correct. One possible way to verify our model would be to compare the Mg/Nb ratios in the ordered and disordered regions using microanalysis in the transmission electron microscope.

Ferroelectric Domains

Until now, there have been very few studies of ferroelectric domains in relaxor materials using the TEM (17-19). As will be seen later, one possible reason for this is that domain structures usually develop only at low temperatures, hence a cooling holder is required. In our work, we examined single crystal and polycrystalline PMN:PT, and single crystal PZN:PT, both at room temperature and at temperatures down to -185°C in the TEM. For the PMN:PT, no domain contrast was observed at room temperature. On cooling in-situ in the TEM (see figure 7), the temperature at which the domains first appeared was -120°C. The crystallography of the domain boundaries was found to be consistent with that of the rhombohedral structure, i.e. the boundary planes were parallel to the (100) and (110) planes. (These correspond to 70° and 109° boundaries, respectively.) The diffraction patterns, however, were pseudocubic, and no spot splitting was observed for patterns taken across a domain boundary. In addition, low temperature precision x-ray diffraction work did not reveal any splitting of the (111) peak, although this splitting would be expected for a cubic to rhombohedral transition. Knowing the sensitivity of the x-ray technique, it was estimated that the angle α in the rhombohedral unit cell was $89.95° \lesssim \alpha \lesssim 90°$.

744
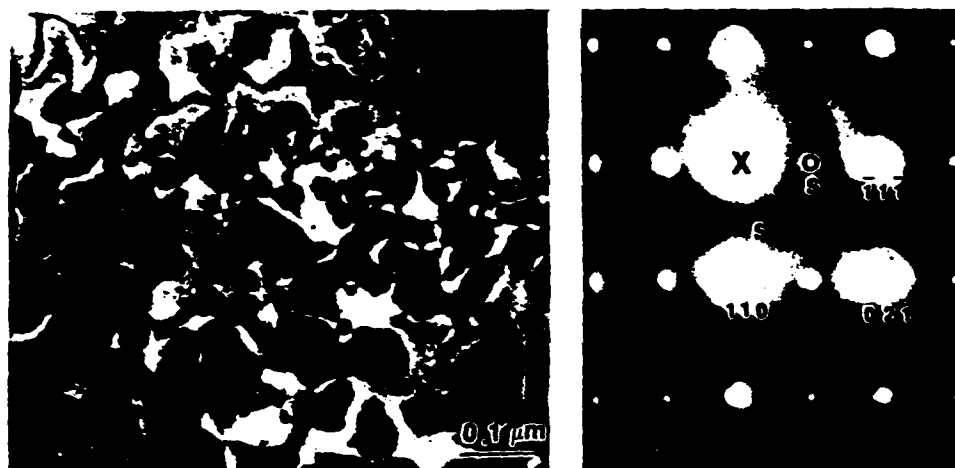
Fig. 6. a) Dark field image showing antiphase domain boundaries in ordered region of $Pb_{0.9}La_{0.1}Mg_{.3667}Nb_{.6333}O_3$. b) Diffraction pattern. (Courtesy J. Chen)

Fig. 7. TEM micrograph of ferroelectric domains in $Pb(Mg_{1/3}Nb_{2/3})O_3.10\%PbTiO_3$. Temperature = -185°C.

For the PZN:PT, ferroelectric domains were visible both at room temperature and -185°C (see figure 8). As in the case of PMN, the domain configurations were consistent with the rhombohedral structure, and this agrees with the results of Kuwata et al. (20). Comparison of figures 7 and 8 shows that the domain width in PZN:PT (≤10nm) is significantly less than that of PMN:PT.

Fig. 8. TEM micrograph showing ferroelectric domains in PZN:PT, room
temperature.

One model of relaxor behavior is that at room temperature, the
ferroelectric domains are very small (100-200Å), and are dynamic, i.e.
constantly switching in direction due to thermal aggitation. For the
PMN:PT, our observation of macrodomains at low temperatures can be
interpreted as the "freezing in" and coalescence of these polar
microdomains with decreasing temperature. At room temperature, it is
postulated that micropolar domains are present but the frequency of
switching is too high for the domains to be observed. The reason then why
domains are observed at room temperature in PZN:PT is not well understood,
and more work needs to be done in this area.

Grain Boundary Phases

Due to problems with material processing, the full commercial
potential of relaxors such as PMN has yet to be realized. Until now, the
major problem was thought to be the formation of a pyrochlore phase during
processing (21), which was apparently very detrimental to the dielectric
properties. Recent results by Chen et al. (22), however, have shown that
PMN made from reagent grade starting oxides, contained second phase films
over a significant proportion of the grain boundaries (see figure 9).
Using x-ray EDS, these films were determined to be rich in lead and
phosphorus. When ultra-high purity (99.999%) starting powders were used,
the grain boundaries were clean. The ultra-high purity PMN had far
superior dielectric properties to the reagent grade PMN, even though it
contained a higher volume fraction of the pyrochlore phase. This is very
strong evidence that the lower values of dielectric constant measured for
reagent grade PMN are due to the presence of impurity derived
intergranular phases, rather than the pyrochlore phase itself.

SUMMARY

From the preceding discussion it is clear that a thorough knowledge
of the microstructure and chemistry of electronic ceramics is vital to the
understanding of their properties. In this regard, modern techniques such
as TEM, HRTEM and x-ray EDS have proven extremely valuable.

Fig. 9. Grain boundary phase in reagent grade PMN.
(Courtesy J. Chen and A. Gorton)

ACKNOWLEDGEMENTS

REFERENCES

1. "Additives and Interfaces in Electronic Ceramics", Vol. 7, M. F. Yan and A. H. Heuer, eds. Amer. Ceram. Soc. (1983).
2. "Grain Boundary Phenomena in Electronic Ceramics", L. M. Levinson, ed., Amer. Ceram. Soc. (1981).
3. H. D. Megaw, Refinement of the Structure of $BaTiO_3$ and Other Ferroelectrics, Acta Crystallogr. 15:972 (1962).
4. S. I. Kegani and I. Ueda, Mechanism of Ageing in Polycrystalline $BaTiO_3$, J. Phys. Soc. Jpn. 22:725 (1967).
5. V. V. Shakmanov and G. V. Spivak, A Microdiffraction Investigation of the Domain Structure in Barium Titanate Films, Sov. Phys. Solid State 10:802 (1968).
6. T. Malis and H. Gleiter, Investigation of the Structure of Ferroelectric Domain Boundaries by Transmission Electron Microscopy, J. Appl. Phys. 47:5195 (1976).
7. Y. H. Hu, H. M. Chan, X. W. Zhang and M. P. Harmer, Scanning Electron Microscopy and Transmission Electron Microscopy Study of Ferroelectric Domains in Doped $BaTiO_3$, J. Amer. Ceram. Soc. 69 (1986).
8. G. H. Jonker and W. Noorlander, "Science of Ceramics", G. H. Stewart, ed., Academic Press, London (1962).
9. N. C. Sharma and E. R. McCartney, The Dielectric Properties of Pure Barium Titanate as a Function of Grain Size, J. Austr. Ceram. Soc., 10:16 (1974).
10. G. Arlt, D. Hennings and G. deWith, Dielectric Properties of Fine-Grained Barium Titanate Ceramics, J. Appl. Phys. 58:1619 (1985).
11a. W. R. Buessem, L. E. Cross and A. K. Goswami, J. Am. Ceram. Soc., 49:371 (1976).
11b. A. J. Bell, A. J. Moulson and L. E. Cross, The Effect of Grain Size

on the Permittivity of $BaTiO_3$, Ferroelectrics 54:147 (1984).

12. W. Heywang, Barium Titanate as a Semiconductor with Blocking Layers, Solid State Electr., 3:51 (1961).

13. G. H. Jonker, Equilibrium Barriers in PTC Thermistors, in "Advances in Ceramics", Vol. 7, M. F. Yan and A. H. Heuer, eds., Amer. Ceram. Soc. (1983).

14. N. Setter and L. E. Cross, The Role of B-Site Cation Disorder in Diffuse Phase Transition Behavior of Perovskite Ferroelectrics, J. Appl. Phys., 51:4356 (1980).

15. M. P. Harmer, A. Bhalla, B. Fox and L. E. Cross, Electron Microscopy of Ordered Domains in Lead Scandium Tantalate, Materials Lettr., 2:278 (1984).

16. H. M. Chan, M. P. Harmer, A. Bhalla and L. E. Cross, TEM of the Relaxor Material $Pb(Sc_{0.5}Ta_{0.5})O_3$, Jap. J. Appl. Phys., 24:550 (1985).

17. S. Nomura, M. Endo and F. Kojima, Ferroelectric Domains and Polarization Reversal in $Pb(Zn_{1/3}Nb_{2/3})O_3$ Crystal, Jap. J. Appl. Phys., 13:2004 (1974).

18. Y. J. Chang and Z. L. Chen, A Study on Ordered Ferroelectric Domains in $Pb(Sc_{1/2}Ta_{1/2})O_3$ Ceramics, Ferroelectrics Lettr. 4:13 (1985).

19. C. A. Randall, D. J. Barber and R. W. Whatmore, A TEM Study of Modified PZT Ferroelectric Ceramics, EMAG '85, Inst. Phys. Conf. Ser. No. 78, Chap. 13 (1985).

20. J. Kuwata, K. Uchino and S. Nomura, Dielectric and Piezoelectric Properties of $0.91Pb(Zn_{1/3}Nb_{2/3})O_3.0.09PbTiO_3$ Single Crystals, Jap. J. Appl. Phys. 21:1298 (1982).

21. S. L. Swartz, T. R. Shrout, W. A. Schulze and L. E. Cross, Dielectric Properties of Lead-Magnesium Niobate Ceramics, J. Am. Ceram. Soc., 67:311 (1984).

22. J.Chen, A. Gorton, H. M. Chan and M. P. Harmer, Effect of Powder Purity and Second Phases on the Dielectric Properties of Lead Magnesium Niobate Ceramics, J. Am. Ceram. Soc., in press (1986).

Scanning Electron Microscopy and Transmission Electron Microscopy Study of Ferroelectric Domains in Doped BaTiO₃

YUNG H. HU,* HELEN M. CHAN,* ZHANG XIAO WEN,* and MARTIN P. HARMER*

Department of Metallurgy and Materials Engineering and Materials Research Center, Lehigh University, Bethlehem, Pennsylvania 18015

This paper describes the results of detailed studies carried out on Ca-doped and Nb-doped BaTiO₃, using scanning electron microscopy and transmission electron microscopy. The techniques used were topographical contrast, selected-area diffraction, and microdiffraction Kikuchi pattern analysis. By these methods it was possible to unambiguously identify the different types of domain boundaries. Also, evidence was obtained for the existence of an unconventional 90° domain boundary which has not previously been reported.

I. Introduction

$\mathbf{M}$ANY of the properties of ferroelectric ceramics such as dielectric constant, aging, dielectric loss, etc., are related to the motion of domain boundaries.[1-5] It is therefore of great importance to be able to examine and accurately interpret ferroelectric domain structures. The domain structure of BaTiO₃ is of particular interest because of its extensive applications in electronic components.[6]

Between 1460° and 130°C, BaTiO₃ adopts a cubic perovskite structure and is paraelectric. On cooling below 130°C, it undergoes a phase transition accompanied by an elongation along one cube axis (c axis), and a contraction along the other two (a) axes. The result is a tetragonal unit cell with a c/a ratio of ≈1.01.[7-9] The tetragonal phase is ferroelectric, the direction of spontaneous po-

larization being parallel to the elongated c axis. This phase is stable down to 5°C, where a transformation to an orthorhombic structure takes place.

Our present knowledge of ferroelectric domains in tetragonal BaTiO₃ can be summarized as follows:

(i) In an individual domain, the direction of polarization occurs along the c axis and parallel to any one of the three original [100] cube axes.

(ii) There are two types of domain boundary, 90° and 180° The angles refer to the angle between the domain polarization vectors on either side of the boundary.

(iii) 90° boundary walls lie on (110) planes and tend to be straight. The energy of 180° boundary walls, however, is less sensitive to crystallographic orientation; thus 180° boundaries are usually "wavy."

(iv) The polarization vectors adopt a "head-to-tail" arrangement across a 90° boundary in order to minimize the charge at the domain wall.

Much of the nomenclature in domain studies derives from early work carried out on Remeika[10] single crystals using a polarization optical microscope.[11-16] Remeika crystals are right-angled triangular plate-shaped crystals. The plane of the crystal is the (001) plane, and the orthogonal crystal edges lie along the [100] and [010] directions.

Domains are designated as either "a" or "c" domains, depending on which axis of the unit cell lies parallel to the viewing direction. The resulting nomenclature for the types of domain boundaries observed can be somewhat confusing because there are (i) 90° a-a boundaries, (ii) 180° a-a boundaries, (iii) c-c boundaries (180° only), and (iv) a-c boundaries (90° only). It should be noted however that (i) and (iv) are structurally identical boundaries, as are (ii) and (iii), the only difference being the direction of viewing. The above boundaries are shown schematically in Fig. 1. Under normal viewing conditions, the optical microscope is unable
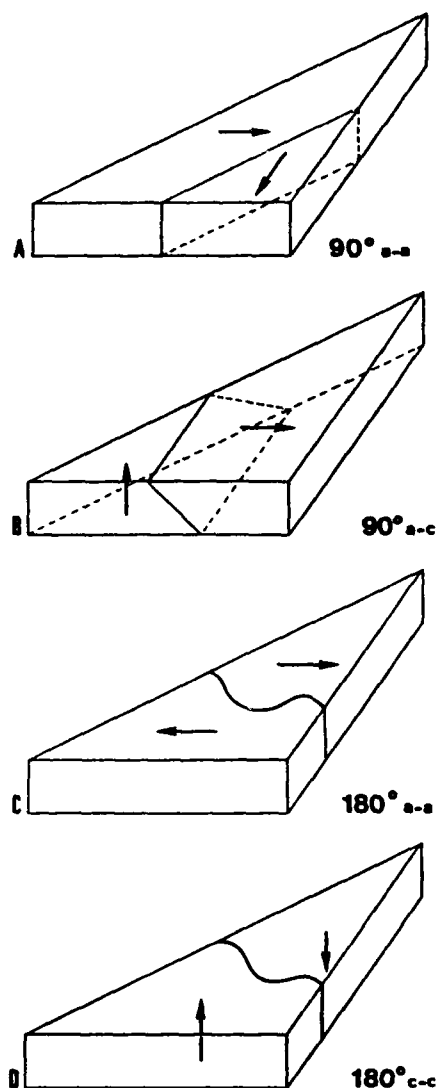
Fig. 1. (A) 90° *a-a* domain boundary. (B) 90° *a-c* domain boundary. (C) 180° *a-a* domain boundary. (D) 180° *c-c* domain boundary.

Gevers and his co-workers[32,33] have applied the dynamical theory of image contrast to calculate the image characteristics of δ boundaries, examples of which are 90° domain walls in BaTiO₃. Delta (δ) boundaries are defined as boundaries where there is a slight difference in lattice parameter across the boundary; thus the value of s (the deviation from the Bragg condition) is different in the two domains for a given reflection. Gevers et al.[29] were able to confirm the results of their calculations by studying the fringe contrast at inclined domain walls for carefully chosen imaging conditions. This technique was also used by Malis and Gleiter,[27] who noted that there was residual contrast when domain walls were imaged using reflections common to both domains. They concluded from this that there is a slight net displacement of the (001) planes which occurs continuously across the domain wall width as a result of the gradual rotation of the polarization vector. In general, fringe contrast analysis is experimentally difficult, and the results can be complicated by thickness effects and multiple diffraction. Shakmanov and Spivak[28] adopted a much simpler approach to domain wall analysis. They derived the selected-area diffraction patterns (SADP) which would be produced for several simple domain configurations. By observing the splitting of high-order diffracted spots, it is possible to determine the domain wall type. The details of this technique will become clear in Section III(2). These workers did not point out, however, that the extent of spot splitting is sensitive to deviations about the zone axis, a problem which is addressed later in this study.

The contrast from 90° domains is diffraction contrast; contrast from 180°C domains, however, is more difficult to understand because there is no difference in the lattice parameters. Despite this, 180° domains can give rise to faint contrast in the TEM for the following reason. The tetragonal unit cell of BaTiO₃ is noncentrosymmetric because of the displacement of the Ti^{4+} ion. For centrosymmetric crystals, Friedel's law (which states that the intensities of the hkl and $\overline{hkl}$ reflections are always equal) is obeyed. Gevers et al.[34] have shown that for noncentrosymmetric crystals, Friedel's law holds for the transmitted beam, but not the diffracted beam. Thus it is possible to see contrast between 180° domains using dark-field imaging only. This effect can also give rise to weak fringe contrast for inclined 180° boundaries.

The purpose of this study was to use state-of-the-art SEM and TEM techniques both to image ferroelectric domains in calcium- and niobium-doped BaTiO₃, and to unambiguously identify the boundary types. A very interesting outcome of this work was the observation of a new type of 90° domain wall which has not been previously reported. Furthermore, the domain structures of Nb-doped and Ca-doped high-purity polycrystalline BaTiO₃ have not previously been reported.

to discern 180° walls. If, however, an electric field is applied perpendicular to the wall, the boundary becomes visible in polarized light because the polarization vector is tilted in opposing directions in the two adjacent domains.[17]

Apart from polarizing light microscopy, several techniques can be used to study ferroelectric domain structures. These include potential contrast,[20-22] decoration techniques,[23] SEM, and TEM. Only studies utilizing electron microscopical techniques will be discussed in detail here.

(1) Scanning Electron Microscopy (SEM)

Hooton and Merz[18] discovered that ferroelectric BaTiO₃ single crystals show a differential etch rate when etched in hydrochloric acid.

During the etching process, the positive ends of the domain etch at the highest rate, whereas the negative ends etch at the slowest rate. The etch rate of domains where the polarization vector is parallel to the surface is intermediate. The difference in etch rates gives rise to topographical contrast which can be used to identify the domain configurations.[19]

(2) Transmission Electron Microscopy (TEM)

Transmission electron microscopy has been used by several groups to study ferroelectric domain structures in BaTiO₃.[24-31]

II. Experimental Procedure

(1) Sample Preparation

Powders of precisely determined chemical composition were made by the liquid mix process.[35] These were then pressed into pellet form and sintered in air at 1450°C for 5 h. The compositions studied were (i) $Ba_{0.95}Ca_{0.05}TiO_3$ and (ii) $BaNb_{0.0025}Ti_{0.9975}O_3$.

(2) SEM

Polished pellets were etched using a solution made up of the following mixture: 35 cm³ of H₂O, 5 cm³ of concentrated HCl, and 5 drops of concentrated HF. The samples were then cleaned ultrasonically in methanol and examined in the ETEC SEM at 20 kV.

(3) TEM

Samples were polished down to ≈20 μm using 600 grit SiC, followed by 6-μm diamond paste. Thin foil specimens were then prepared by ion beam thinning at 6 kV, and examined in an electron microscope[*] at 120 kV. Domain structures were studied using the following techniques:
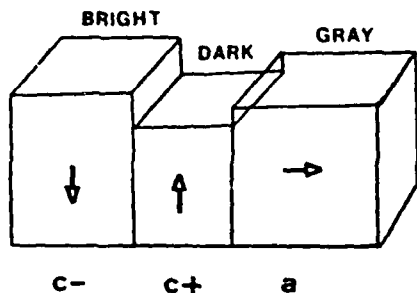
Fig. 2. Topographical contrast caused by differential etch rates.

(A) Selected-Area Diffraction (SAD): Diffraction patterns were obtained by placing the SA aperature over individual domain walls for specific grain orientations.

(B) Microdiffraction Kikuchi Line Measurement: By focusing the electron beam to a fine spot size (<0.1 μm^2), we obtained microdiffraction patterns from individual domains. Because of the convergent nature of the beam, and the small volume of material sampled, a clearly defined Kikuchi line pattern was readily obtained.[36] Great care was taken to ensure that no specimen drift took place during the recording of the diffraction patterns.

III. Results and Discussion

Similar features were observed in the domain structures of both the Ca-doped and Nb-doped $BaTiO_3$; thus the results from these samples will be discussed together.

(1) SEM of Conventional 90° and 180° Domain Boundaries

It can be seen from Fig. 2 that in the SEM $c-$ domains will appear bright, $c+$ domains will appear dark, and a domains will appear gray. The different types of domain are, therefore, clearly discernible from the etched microstructure. In Fig. 3(a), a region of a sample is shown encircled. The significant point about this region is that the observed domain boundaries intersect each other at either 45° or 90°; thus it can be deduced that this grain has been sectioned parallel to a cube (100) plane. Given this fact, it is possible to assign polarization vectors to each domain, and obtain a domain configuration fully consistent with the SEM image as shown in Fig. 3(b). Note that although there is no topographical contrast at 90° $a-a$ and 180° $a-a$ boundaries (shown as dotted lines), their presence can be inferred from the nature of the surrounding domains. Also all of the domain boundary lines in this region are straight; some consist of 180° domain walls, some are all 90°, and others consist of alternating 90° and 180° segments. What is clear and should be learned from this figure is that straight domain boundaries do not always qualify as 90° domain boundaries as has been suggested in the past.[39]

Another possible method for determining the grain orientation is electron channeling. Although this technique was not used in this study, it can be noted that channeling would be more suited to the Ca-doped material, because of its larger grain size.

(2) TEM of Conventional 90° Domain Boundaries

To carry out identification of the domains in the TEM, it is necessary to tilt the grain to a (100) orientation. By comparing the observed SAD patterns with those predicted by superimposing the diffraction patterns of the individual domains, boundary identification can be carried out. Before we present our results however, it is worthwhile discussing a point raised earlier, i.e., that the extent of spot splitting is affected by the foil orientation. The reason for this can be seen from Fig. 4. If the beam direction does not lie exactly on the [100] zone axis, the Ewald sphere is effectively tilted about the 000 transmitted spot so that the spot separation changes from δ to δ'. In order to ensure the correct interpretation of the SADP's obtained in this study (especially
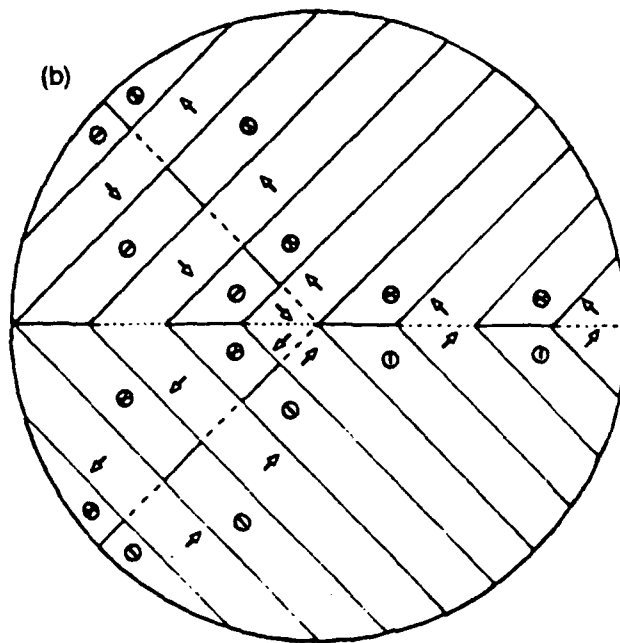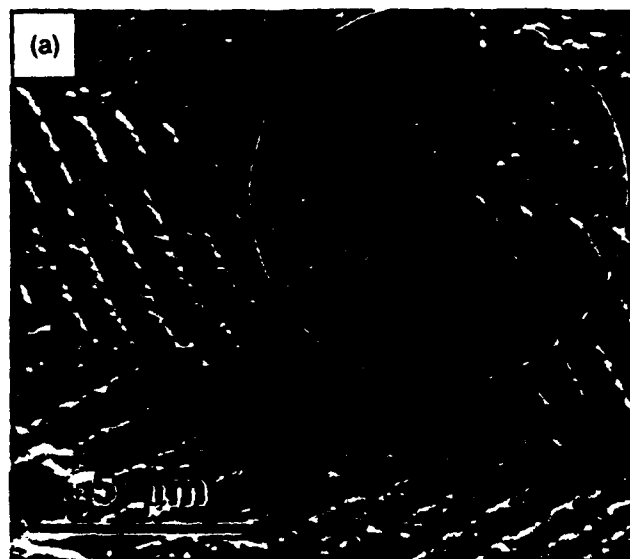
Fig. 3. (a) SEM micrograph of etched microstructure showing topographical contrast at domain boundaries. The encircled region shows an area of the specimen where the surface is parallel to (100) plane. (b) Domain configuration consistent with Fig. 3(a).

with regard to the distinction between conventional and unconventional 90° domain boundaries), it was necessary to determine quantitatively the extent of this effect. The maximum value of ϕ (the angle of tilt) for the [100] spot pattern to be still clearly visible is ≈15°. The value of δ/δ' is given by cos ϕ, hence

$$\delta/\delta' = 0.96 \quad \text{for } \phi_{max}$$

This analysis predicts therefore that the extent of spot splitting does not change significantly with orientation. Tilting away from the zone axis is however advantageous, as it enables the higher orders of reflection (which show greater splitting) to be observed.

The procedure for domain boundary analysis by SAD is illustrated in Fig. 5. Figure 5(a) is the bright-field (BF) image of the domain arrangement, and Fig. 5(b) shows a schematic sketch of the postulated conventional 90° domain structure viewed parallel to the beam direction. Note that because of the tetragonality of the unit cell, a slight rotation (0.57°) of the lattice planes occurs at the
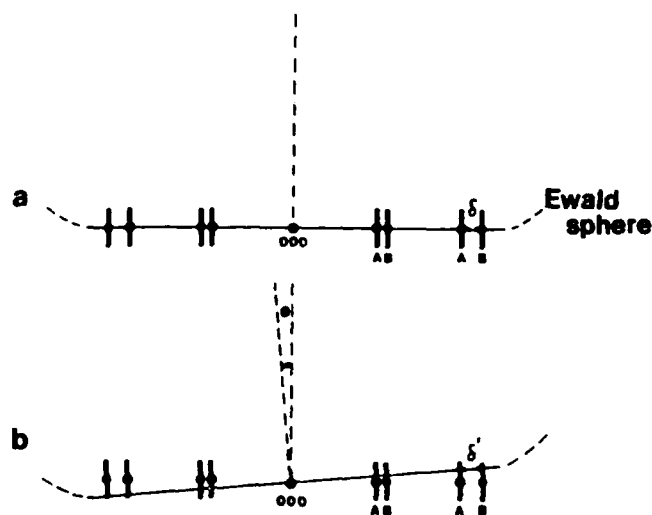
Fig. 4. Effect of specimen tilt on diffraction spot separation: (a) on zone, spot separation δ; (b) tilted by angle ϕ, spot separation δ'.

boundary. The axis of rotation is the [100] (viewing direction). Figure 5(c) is the corresponding diffraction pattern net: the degree of tetragonality and angle of rotation have been exaggerated for clarity. It can be seen that the most pronounced spot splitting is predicted to occur for the (0kk) reflections lying along the diagonal OP, and that the direction of the splitting is approximately perpendicular to this. A comparison with Fig. 5(d) shows that this is what was observed. It was also determined that the trace of the boundary was parallel to the [011] direction, thus providing additional confirmation that the boundary was a conventional 90° a-a domain wall.

Figure 6 shows the corresponding analysis for a conventional 90° a-c boundary. Note that this boundary is geometrically identical with the conventional 90° a-a boundary, except viewed from a different direction. Fringe contrast is observed because the boundary is inclined at 45° to the plane of the foil. For this type of boundary the line of intersection of the boundary with the foil surface lies along the [010] direction. Also the direction of spot splitting is along the cube axis [001]$_A$, and this is seen clearly in Fig. 6(d).

Kikuchi pattern analysis was also used to determine the domain boundary nature. Figure 7 shows a set of Kikuchi patterns obtained
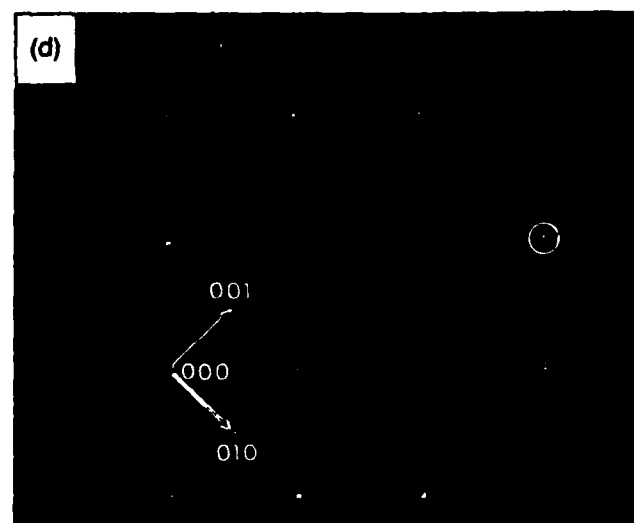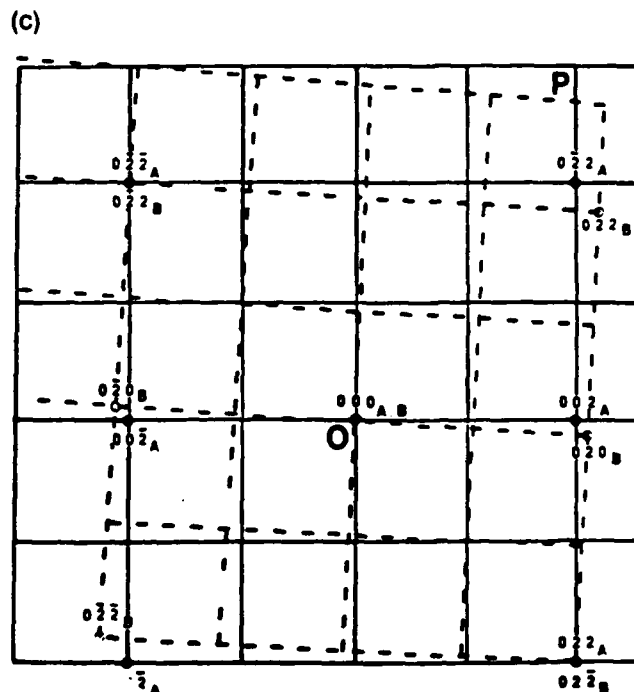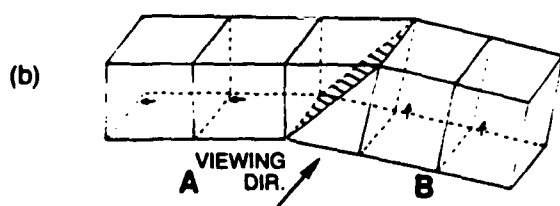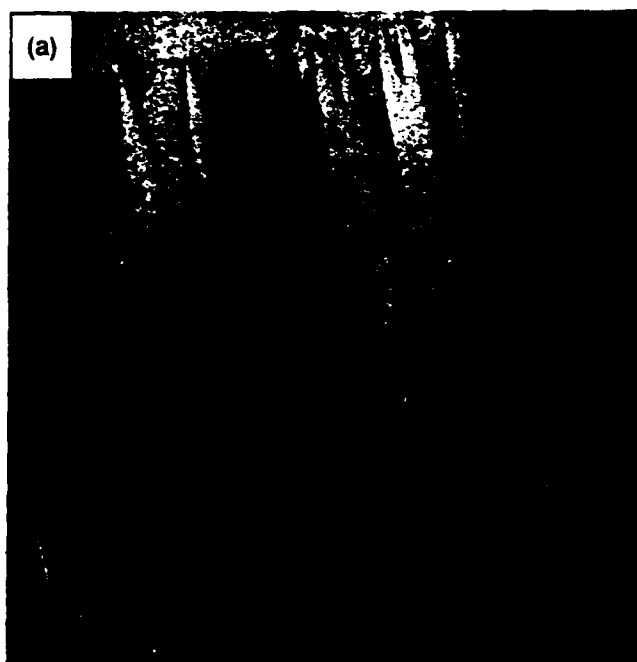

Fig. 5. 90° a-a domain boundaries: (a) TEM BF image (Ca-doped), (b) schematic representation of domain boundary, (c) [100] diffraction pattern net, (d) [100] SADP.
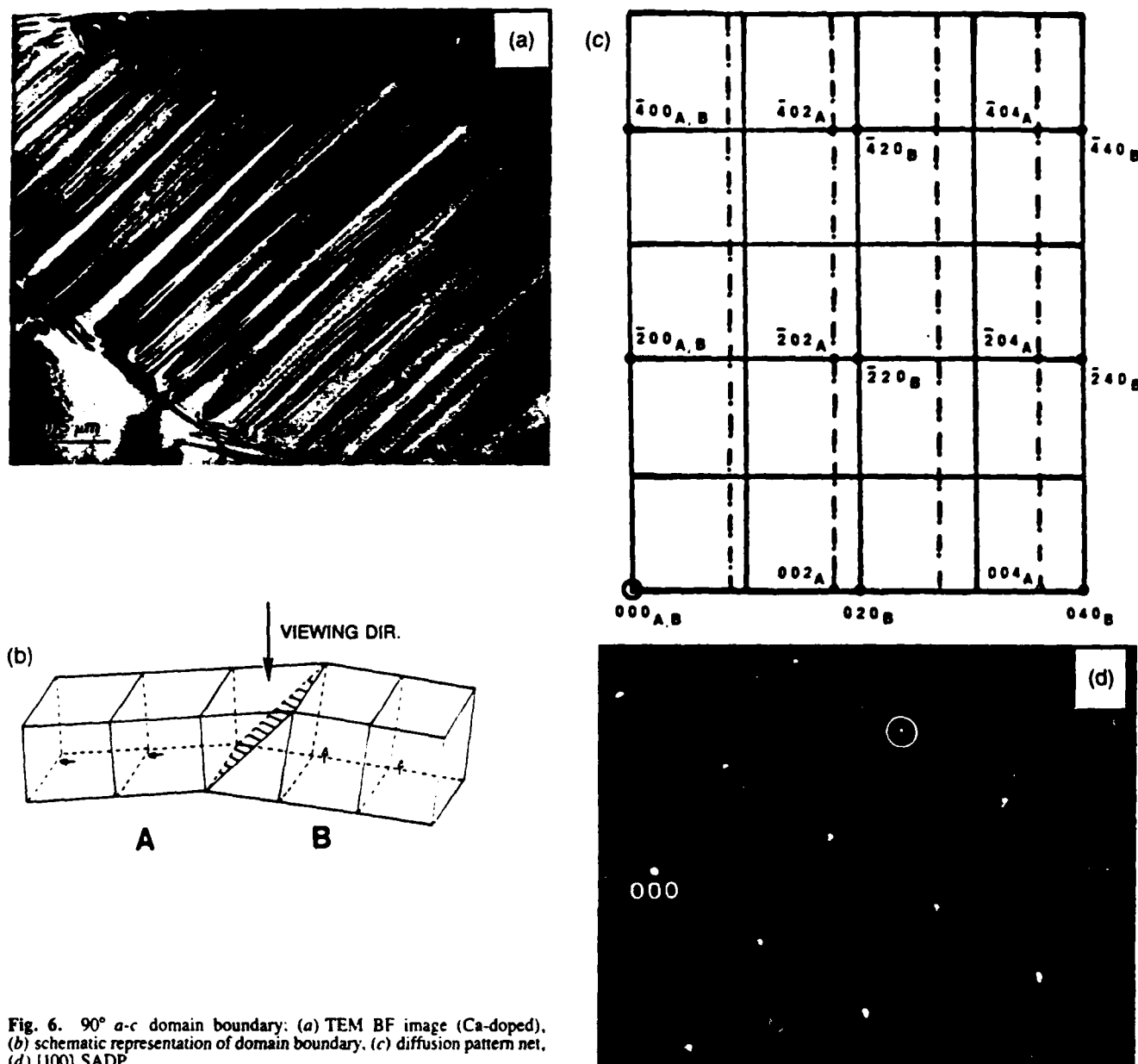
Fig. 6. 90° *a-c* domain boundary: (*a*) TEM BF image (Ca-doped), (*b*) schematic representation of domain boundary, (*c*) diffusion pattern net, (*d*) [100] SADP.

from domains on either side of a conventional 90° *a-a* wall. The Kikuchi line separation is directly related to the lattice spacing and, unlike the separation of diffraction spots, is not sensitive to any deviation from the exact Bragg condition. For this reason, the relative magnitudes of the (001) and (010) lattice parameters for the two domains were readily determined. Comparing the lattice spacings of corresponding parallel planes for the two domains it was found that

$$d_{(001)M} > d_s$$

and

$$d_{(010)M} < d_s$$

as expected for a conventional 90° *a-a* boundary.

(3) SEM and TEM of Unconventional 90° Domain Boundaries

In the course of this study, SEM and TEM evidence was obtained for an unconventional 90° domain boundary. This new type of boundary was observed in both the Nb-doped and Ca-doped samples. The first indications of the possibility of a new domain

configuration came from the SEM results shown in Fig. 8(*a*). This figure is of interest because not only does it show the new type of boundary (region *A*), but also region *B* can be interpreted as the area of intersection of two orthogonal, 90° *a-a* domain colonies. It is thought that the domain contrast in area *B* is due to slight preferential etching of the *a-a* boundaries. One feasible representation of the domain structure in *A* is shown in Fig. 8(*b*); the unconventional boundary is shown as the fine dashed line. The new domain configuration is postulated to be as shown in Fig. 9(*a*). Comparison with Fig. 5(*b*) will confirm that this proposed arrangement is geometrically different from the conventional 90° boundary. In order to obtain conclusive evidence for the existence of this new type of boundary, detailed TEM analysis was carried out on a large number of domain structures.

The predicted diffraction pattern for this boundary when viewed edge-on along a cube axis direction is shown in Fig. 9(*b*). The important difference between this net and Fig. 5(*c*) is that the extent of splitting for reflections along the two cube axis directions is different; i.e., the diffraction pattern is not symmetrical about the [$\bar{1}$10] direction. Careful examination of Fig. 10(*b*) will show that the observed pattern corresponds to the above predictions, thus
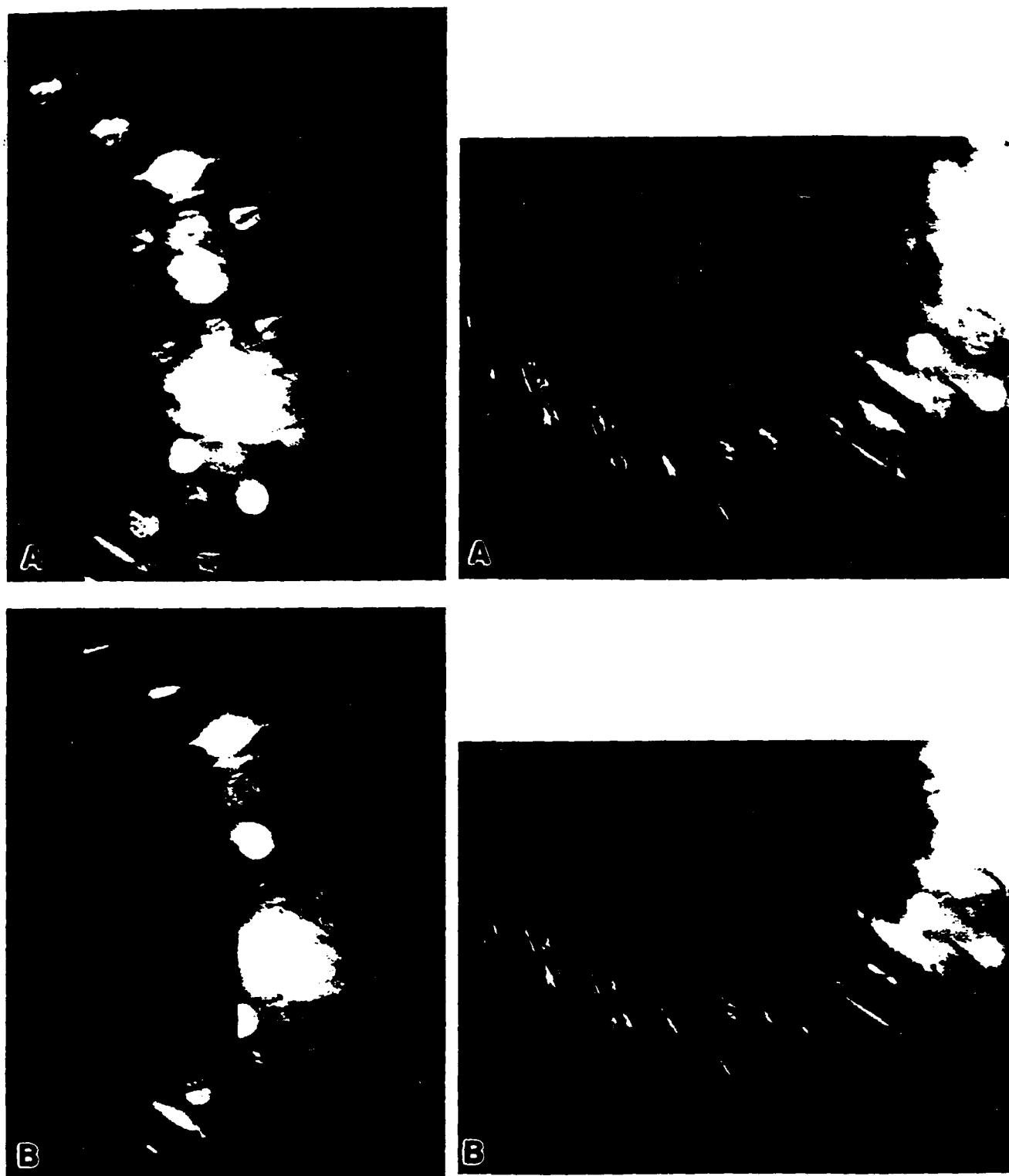
Fig. 7. Kikuchi line patterns from domains A and B on either side of a 90° a-a boundary.

proving that the domains shown in Fig. 10(a) are of the new type. It should be noted that although Fig. 10(b) is not a zone axis diffraction pattern, the angle of tilt about both cube axes is equal; thus any effect of tilt on the spot separation (however slight) would be the same. Kikuchi line measurements showed that for one set of cube planes the lattice spacings were the same in both domains, but for the orthogonal set, the lattice spacings were different. This is consistent with the proposed configuration of the new boundary

and provides additional evidence for its existence. Note that it was also determined that the trace of the boundary was parallel to the (110) direction; thus it cannot be argued that we have been mistakenly studying a 90° a-c boundary (which would show similar Kikuchi pattern characteristics). A further example of an unconventional 90° domain structure is given in Fig. 11. It is interesting to note the transition from the unconventional boundary to the conventional 90° a-c wall.

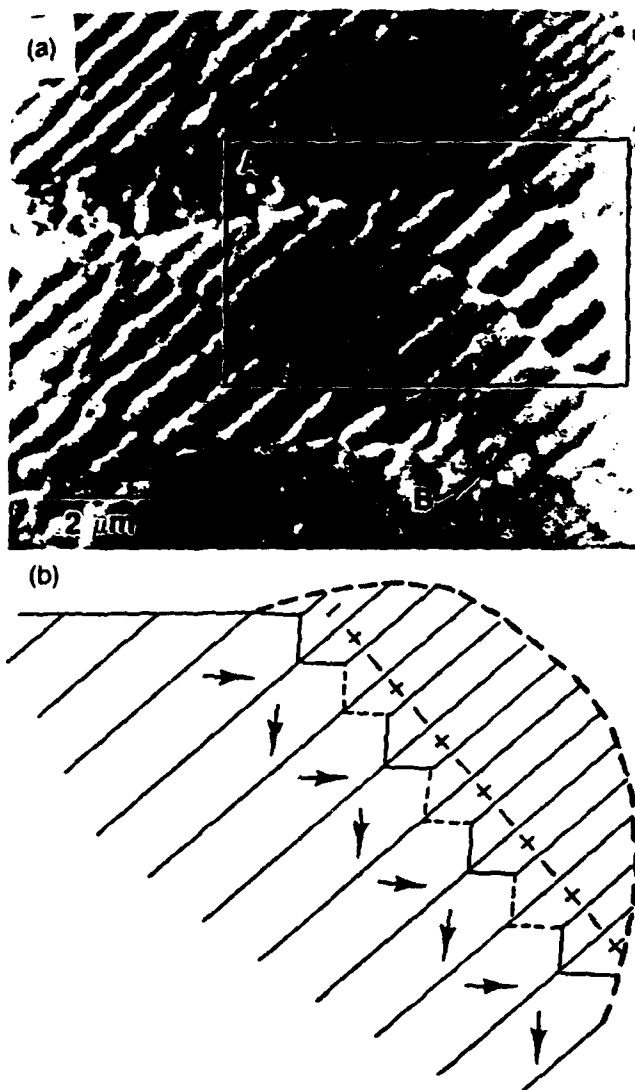Fig. 8. (a) SEM micrograph: (A) unconventional domain configuration, (B) region of intersection of two orthogonal 90° a-a domain colonies. (b) Postulated domain structure in A.
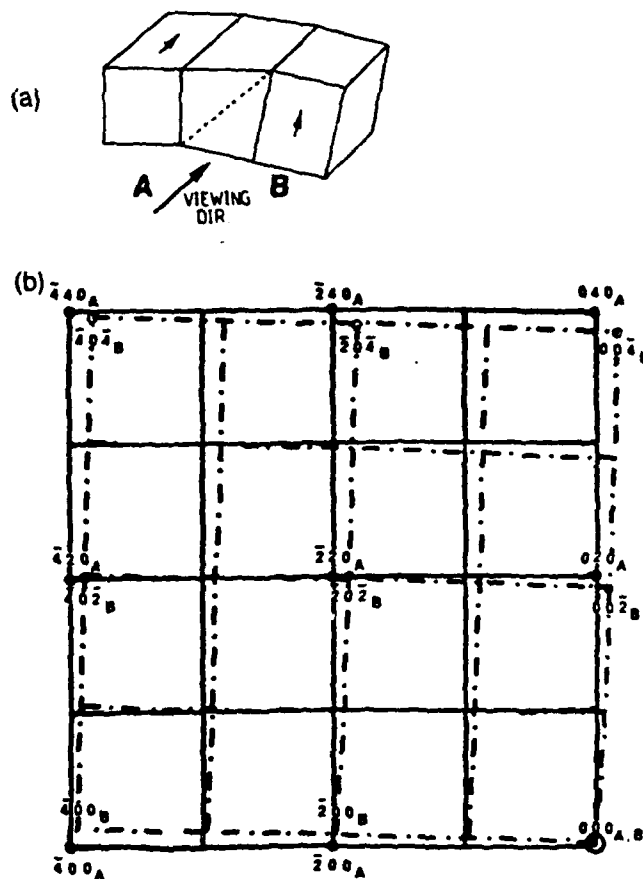

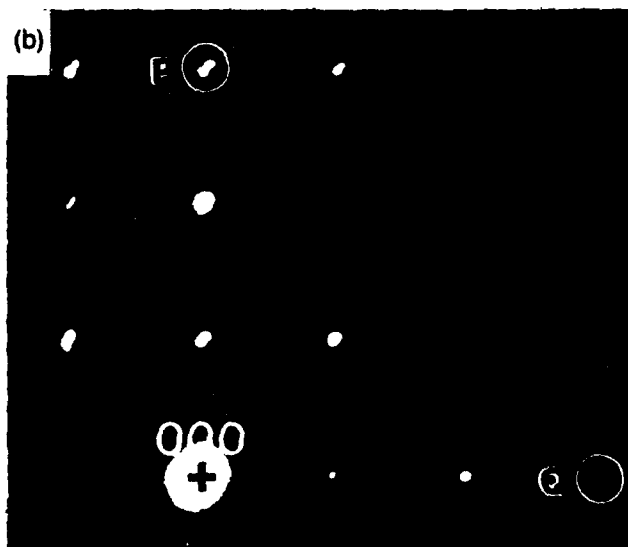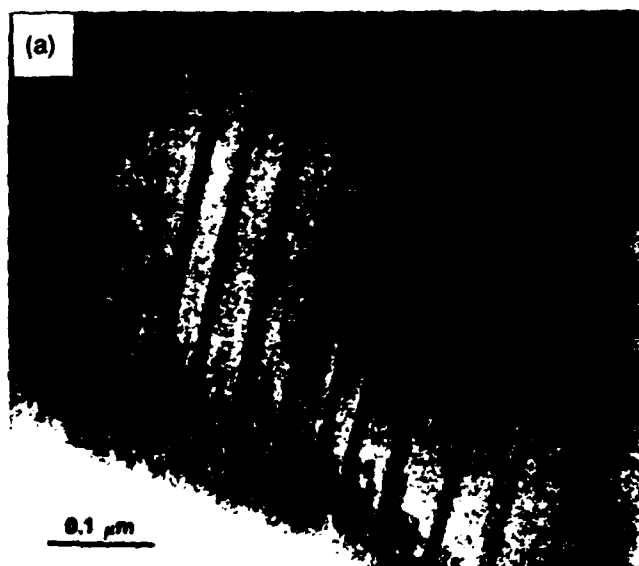Fig. 9. (a) Schematic representation of new domain boundary. (b) Diffraction pattern net.

Fig. 10. (a) TEM BF micrograph of unconventional domain structure (Ca-doped). (b) Corresponding [100] SADP. Note difference in extent of spot splitting for reflections marked P and Q.

Fig. 11. (a) TEM BF micrograph of unconventional domain structure (Nb-doped). (b) Proposed domain configuration. AB: Conventional a-c boundary. BC: Unconventional boundary.
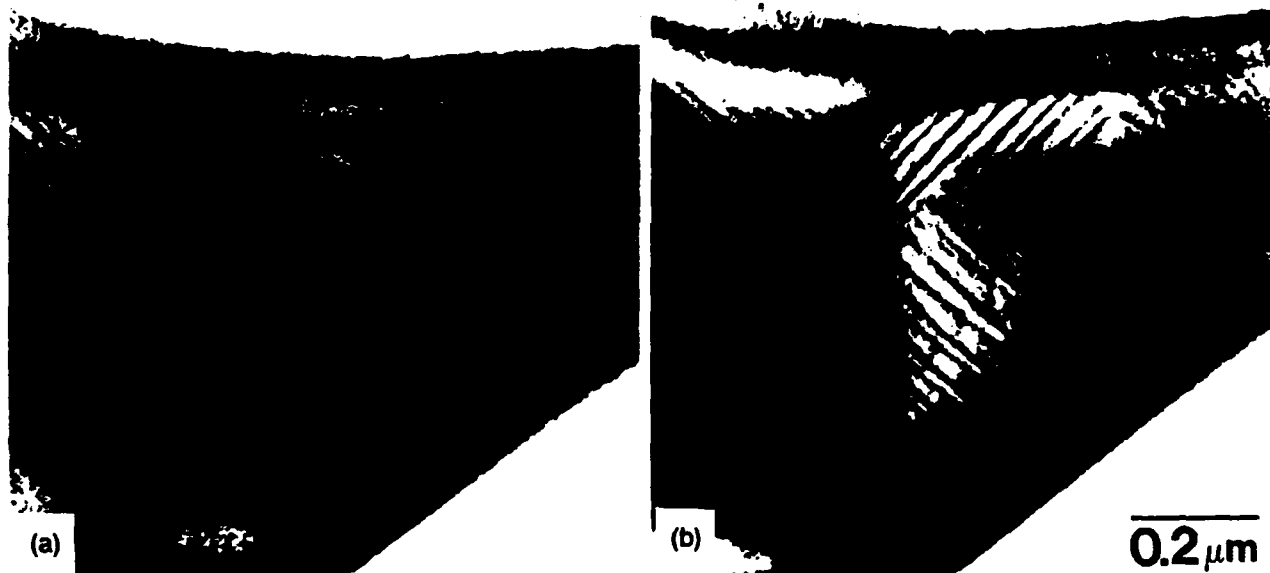

Fig. 12. (a) Region containing unconventional domain configuration. (b) The same region after a short period of time — the new domains are the conventional type.

The reasons for the existence of this new type of domain wall are not well understood, particularly as there are several factors which would seem to strongly favor the formation of conventional 90° boundaries. Firstly, the unconventional boundary will have a higher energy than a conventional domain wall because of the greater degree of distortion; thus the conventional domain structure would presumably be more stable. This conclusion is supported by the following observation. Figure 12(a) shows a region of the specimen containing the new domain structure. After a short period of time had elapsed however, conventional domains (as determined by SAD) were observed to nucleate and grow in place of the new domains. Another factor which points to a relatively higher value for the unconventional boundary energy is the fact that because of the nature of the domain configuration, there must be a net charge at the boundary (see Fig. 13). Despite these arguments, strong evidence has been obtained for the existence of these domains.
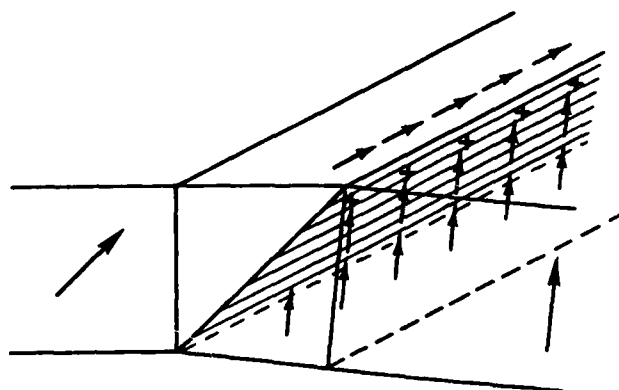

Fig. 13. Diagram showing net positive charge at unconventional boundary surface (all other charges cancel because of head-to-tail arrangement).

Journal of the American Ceramic Society–Hu et al.

Why then do they form? One explanation is that this type of domain configuration occurs in regions where its formation compensates for existing, complex stresses. Thus the existence of new domains would be favored in small-grained. polycrystalline material (such as the samples studied), as here, very complicated stresses can develop below the Curie temperature because of the constrictions of surrounding grains. Another reason which helps to explain the presence of the unconventional boundaries is the reduced distortion at the boundary due to the dopant concentration. It has been found that the addition of Ca^{37} and Nb^{38} has the effect of lowering the c/a ratio in $BaTiO_3$; thus the boundary energy may be reduced. Clearly further work is necessary to fully understand the nature of this unconventional domain boundary. Future study will explore more fully the role of factors such as dopant type and concentration and grain size on the incidence of these new domains.

IV. Summary

This study has shown that unambiguous identification of domain structures can be carried out using the SEM and TEM. Evidence was obtained for the existence of an unconventional 90° domain configuration which has not previously been reported.

References

[1]K. W. Plessner, "Ageing of the Dielectric Properties of Barium Titanate Ceramics," *Proc. Phys. Soc.. London*, 69, 1261–68 (1956).
[2]Z. Pajak and J. Stankowskie. "Polarization Changes During the Process of Aging in Ferroelectrics of the $BaTiO_3$-type," *Proc. Phys. Soc.. London*, 72, 1144–46 (1958)
[3]J. Stankowska and J. Stankowski, "Ageing Process in Triglycine Sulphate," *Proc. Phys. Soc.. London*, 75, 455–56 (1960).
[4]S. Ikegami and I. Ueda, "Mechanism of Ageing in Polycrystalline $BaTiO_3$," *J. Phys. Soc. Jpn.*, 22, 725–34 (1967).
[5]W. P. Mason, "Ageing of the Properties of Barium Titanate and Related Ferroelectric Ceramics," *J. Acoust. Soc. Am.*, 27. 73–85 (1955)
[6]L. E. Cross, "Dielectric, Piezoelectric, and Ferroelectric Components," *Am. Ceram. Soc. Bull.*, 63 [4] 586–90 (1984).
[7]H. F. Kay and P. Vousden. "Symmetry Changes in Barium Titanate at Low Temperatures and Their Relation to Its Ferroelectric Properties," *Philos. Mag.*, 40, 1019–39 (1949).
[8]H. D. Megaw. "Temperature Changes in the Crystal Structure of Barium Titanium Oxide." *Proc. Phys. Soc.. London. Sect. A.* A189. 261–83 (1947).
[9]H. D. Megaw, "Refinement of the Structure of $BaTiO_3$ and Other Ferroelectrics," *Acta Crystallogr.*, 15, 972–73 (1962).
[10]J. P. Remeika. "A Method for Growing Barium Titanate Single Crystals," *J. Am. Chem. Soc.*, 76, 940–41 (1954).
[11]R. C. Bradt and G. S. Ansell, "Aging in Tetragonal Ferroelectric Barium Titanate." *J. Am. Ceram. Soc.*, 52 [4] 192–99 (1969).
[12]B. Matthias and A. von Hippel, "Domain Structure and Dielectric Response of Barium Titanate Single Crystals," *Phys. Rev.*, 73. 1378–84 (1948).
[13]R. C. DeVries and J. E. Burke. "Microstructure of Barium Titanate Ceramics," *J. Am. Ceram. Soc.*, 40 [6] 200–206 (1957).
[14]E. A. Little, "Dynamic Behavior of Domain Walls in Barium Titanate." *Phys. Rev.*, 158, 478–84 (1955).
[15]H. Blattner, W. Kanzig, W. Merz. and H. Sutter, "The Domain Structure of $BaTiO_3$ Crystals," *Helv. Phys. Acta.* 21, 207–209 (1948).
[16]B. Matthias and A. von Hippel, "Structure, Electrical, and Optical Properties of Barium Titanate," *Phys. Rev.*, 73, 268–69 (1948).
[17]W. J. Merz, "Domain Properties in Barium Titanate," *Phys. Rev.*, 88, 421–22 (1952).
[18]J. A. Hooton and W. J. Merz, "Etch Patterns and Ferroelectric Domains in $BaTiO_3$ Single Crystals," *Phys. Rev.*, 98, 409–13 (1955).
[19]G. Y. Robinson and R. M. White. "Scanning Electron Microscopy of Ferroelectric Domains in Barium Titanate," *Appl. Phys. Lett.*, 10, 320–23 (1967).
[20]K. N. Maffitt, "Interpretation of Electron-Mirror Micrographs of Ferroelectric and Dielectric Surfaces," *J. Appl. Phys.*, 39. 3878–82 (1968).
[21]V. V. Aristov, L. S. Kokhanchik, K. P. Meyer, and H. Blumtritt, "Scanning Electron Microscopic Investigations of Peculiarities of the $BaTiO_3$ Ferroelectric Domain Contrast," *Phys. Status Solidi A*, 78A. 229–36 (1983).
[22]R. LeBihan, J. L. Chartier, and L. Jean. "Measurement of Surface Potential Between Ferroelectric Domains with a Quantitative Electron Mirror Microscope." *Ferroelectrics*, 17, 429–31 (1977).
[23]A. Sawada and R. Abe, "New Decoration Techniques for Revealing Antiparallel 180° Domains in $BaTiO_3$," *Jpn. J. Appl. Phys.*, 5, 401–404 (1966).
[24]M. Tanaka and G. Honjo. "Electron Optical Studies of Barium Titanate Single Crystal Films," *J. Phys. Soc. Jpn.*, 19. 954–70 (1964).
[25]M. Tanaka, M. Kitamuran, and G. Honjo. "Electron Optical Studies of Barium Titanate Single Crystal Films," *J. Phys. Soc. Jpn.*, 17, 1197–98 (1962).
[26]V. V. Shakmanov and G. V. Spivak. "A Microdiffraction Investigation of the Domain Structure in Barium Titanate Films." *Sov. Phys.—Solid State (Engl Transl.)*, 10, 802–806 (1968).
[27]T. Malis and H. Gleiter, "Investigation of the Structure of Ferroelectric Domain Boundaries by Transmission Electron Microscopy." *J. Appl. Phys.*, 47, 5195–200 (1976).
[28]H. Blank and S. Amelinckx, "Direct Observation of Ferroelectric Domains in Barium Titanate," *Appl. Phys. Lett.*, 2. 140–42 (1963).
[29]R. Gevers, P. Delavignette, H. Blank. J. Van Landuyt, and S. Amelinckx, "Electron Microscope Transmission Images of Coherent Domain Boundaries II. Observations," *Phys. Status Solidi*, 5, 595–633 (1964).
[30]G. Remaut, R. Gevers, and S. Amelinckx. "Wavy Fringes at Domain Boundaries in Barium Titanate Observed in the Electron Microscope." *Phys. Status Solidi*, 20. 613–21 (1967).
[31]M. D. Dennis, "Transmission Electron Microscopy of Ferroelectric Domains in Barium Titanate"; Ph.D. Thesis. The Pennsylvania State University, University Park, PA, 1972.
[32]R. Gevers, P. Delavignette, H. Blank. and S. Amelinckx. "Electron Microscope Transmission Images of Coherent Domain Boundaries." *Phys. Status Solidi*, 4. 383–410 (1964).
[33]G. Remaut, R. Gevers, A. Lagasse. and S. Amelinckx. "Dynamical Theory of the Images of Microtwins as Observed in the Electron Microscope. III. Observations and Results of Numerical Calculations." *Phys. Status Solidi*, 13, 125–40 (1966)
[34]R. Gevers, H. Blank, and S. Amelinckx. "Extension of the Howie-Whelan Equations for Electron Diffraction to Non-Centro Symmetrical Crystals." *Phys. Status Solidi*, 13, 449–65 (1966).
[35]N. H. Chan, R. K. Sharma, and D. M. Smyth. "Nonstoichiometry in $SrTiO_3$." *J. Electrochem. Soc.*, 128, 1762–69 (1981).
[36]D. B. Williams, "Practical Analytical Electron Microscopy in Materials Science"; p. 126. Philips Electron Optics Publishing. Mahwah, NJ. 1984.
[37]T. Mitsui and W. B. Westphal. "Dielectric and X-ray Studies of $Ca_xBa_{1-x}TiO_3$ and $Ca_xSr_{1-x}TiO_3$," *Phys. Rev.*, 124. 1354–59 (1961).
[38]W. R. Buessem and M. Kahn. "Effects of Grain Growth on the Distribution of Nb in $BaTiO_3$ Ceramics," *J. Am. Ceram. Soc.*, 54 [9] 458–61 (1971).
[39]B. Jaffe, W. R. Cook, and H. Jaffe. "Piezoelectric Ceramics"; pp. 64–71. Academic Press, New York, 1971.

Scanning Electron Microscopy and Transmission Electron Microscopy Study of Ferroelectric Domains in Doped BaTiO₃

YUNG H. HU,* HELEN M. CHAN,* ZHANG XIAO WEN,* and MARTIN P. HARMER*

Department of Metallurgy and Materials Engineering and Materials Research Center, Lehigh University, Bethlehem,
Pennsylvania 18015

This paper describes the results of detailed studies carried out on Ca-doped and Nb-doped BaTiO₃ using scanning electron microscopy and transmission electron microscopy. The techniques used were topographical contrast, selected-area diffraction, and microdiffraction Kikuchi pattern analysis. By these methods it was possible to unambiguously identify the different types of domain boundaries. Also, evidence was obtained for the existence of an unconventional 90° domain boundary which has not previously been reported.

I. Introduction

MANY of the properties of ferroelectric ceramics such as dielectric constant, aging, dielectric loss, etc., are related to the motion of domain boundaries.[1-5] It is therefore of great importance to be able to examine and accurately interpret ferroelectric domain structures. The domain structure of BaTiO₃ is of particular interest because of its extensive applications in electronic components.[6]

Between 1460° and 130°C, BaTiO₃ adopts a cubic perovskite structure and is paraelectric. On cooling below 130°C, it undergoes a phase transition accompanied by an elongation along one cube axis (c axis), and a contraction along the other two (a) axes. The result is a tetragonal unit cell with a c/a ratio of ≈ 1.01.[7-9] The tetragonal phase is ferroelectric, the direction of spontaneous po-

larization being parallel to the elongated c axis. This phase is stable down to 5°C, where a transformation to an orthorhombic structure takes place.

Our present knowledge of ferroelectric domains in tetragonal BaTiO₃ can be summarized as follows:

(i) In an individual domain, the direction of polarization occurs along the c axis and parallel to any one of the three original [100] cube axes.

(ii) There are two types of domain boundary, 90° and 180° The angles refer to the angle between the domain polarization vectors on either side of the boundary.

(iii) 90° boundary walls lie on (110) planes and tend to be straight. The energy of 180° boundary walls, however, is less sensitive to crystallographic orientation; thus 180° boundaries are usually "wavy."

(iv) The polarization vectors adopt a "head-to-tail" arrangement across a 90° boundary in order to minimize the charge at the domain wall.

Much of the nomenclature in domain studies derives from early work carried out on Remeika[10] single crystals using a polarization optical microscope.[11-16] Remeika crystals are right-angled triangular plate-shaped crystals. The plane of the crystal is the (001) plane, and the orthogonal crystal edges lie along the [100] and [010] directions.

Domains are designated as either "a" or "c" domains, depending on which axis of the unit cell lies parallel to the viewing direction. The resulting nomenclature for the types of domain boundaries observed can be somewhat confusing because there are (i) 90° a-a boundaries, (ii) 180° a-a boundaries, (iii) c-c boundaries (180° only), and (iv) a-c boundaries (90° only). It should be noted however that (i) and (iv) are structurally identical boundaries, as are (ii) and (iii), the only difference being the direction of viewing. The above boundaries are shown schematically in Fig. 1. Under normal viewing conditions, the optical microscope is unable
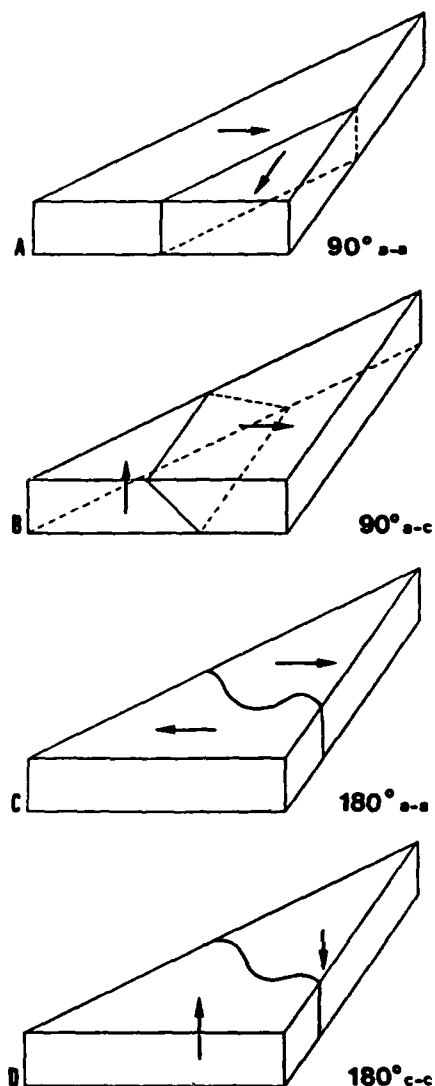
Fig. 1. (A) 90° *a-a* domain boundary. (B) 90° *a-c* domain boundary. (C) 180° *a-a* domain boundary. (D) 180° *c-c* domain boundary.

Gevers and his co-workers[32,33] have applied the dynamical theory of image contrast to calculate the image characteristics of δ boundaries, examples of which are 90° domain walls in BaTiO₃. Delta (δ) boundaries are defined as boundaries where there is a slight difference in lattice parameter across the boundary; thus the value of s (the deviation from the Bragg condition) is different in the two domains for a given reflection. Gevers *et al.*[39] were able to confirm the results of their calculations by studying the fringe contrast at inclined domain walls for carefully chosen imaging conditions. This technique was also used by Malis and Gleiter,[27] who noted that there was residual contrast when domain walls were imaged using reflections common to both domains. They concluded from this that there is a slight net displacement of the (001) planes which occurs continuously across the domain wall width as a result of the gradual rotation of the polarization vector. In general, fringe contrast analysis is experimentally difficult, and the results can be complicated by thickness effects and multiple diffraction. Shakmanov and Spivak[26] adopted a much simpler approach to domain wall analysis. They derived the selected-area diffraction patterns (SADP) which would be produced for several simple domain configurations. By observing the splitting of high-order diffracted spots, it is possible to determine the domain wall type. The details of this technique will become clear in Section III(2). These workers did not point out, however, that the extent of spot splitting is sensitive to deviations about the zone axis, a problem which is addressed later in this study.

The contrast from 90° domains is diffraction contrast; contrast from 180°C domains, however, is more difficult to understand because there is no difference in the lattice parameters. Despite this, 180° domains can give rise to faint contrast in the TEM for the following reason. The tetragonal unit cell of BaTiO₃ is noncentrosymmetric because of the displacement of the Ti^{4+} ion. For centrosymmetric crystals, Friedel's law (which states that the intensities of the hkl and $\overline{hkl}$ reflections are always equal) is obeyed. Gevers *et al.*[34] have shown that for noncentrosymmetric crystals, Friedel's law holds for the transmitted beam, but not the diffracted beam. Thus it is possible to see contrast between 180° domains using dark-field imaging only. This effect can also give rise to weak fringe contrast for inclined 180° boundaries.

The purpose of this study was to use state-of-the-art SEM and TEM techniques both to image ferroelectric domains in calcium- and niobium-doped BaTiO₃, and to unambiguously identify the boundary types. A very interesting outcome of this work was the observation of a new type of 90° domain wall which has not been previously reported. Furthermore, the domain structures of Nb-doped and Ca-doped high-purity polycrystalline BaTiO₃ have not previously been reported.

II. Experimental Procedure

(1) Sample Preparation

Powders of precisely determined chemical composition were made by the liquid mix process.[35] These were then pressed into pellet form and sintered in air at 1450°C for 5 h. The compositions studied were (i) $Ba_{0.95}Ca_{0.05}TiO_3$ and (ii) $BaNb_{0.0025}Ti_{0.9975}O_3$.

(2) SEM

Polished pellets were etched using a solution made up of the following mixture: 35 cm³ of H_2O, 5 cm³ of concentrated HCl, and 5 drops of concentrated HF. The samples were then cleaned ultrasonically in methanol and examined in the ETEC SEM at 20 kV.

(3) TEM

Samples were polished down to ≈20 μm using 600 grit SiC, followed by 6-μm diamond paste. Thin foil specimens were then prepared by ion beam thinning at 6 kV, and examined in an electron microscope[*] at 120 kV. Domain structures were studied using the following techniques:

to discern 180° walls. If, however, an electric field is applied perpendicular to the wall, the boundary becomes visible in polarized light because the polarization vector is tilted in opposing directions in the two adjacent domains.[17]

Apart from polarizing light microscopy, several techniques can be used to study ferroelectric domain structures. These include potential contrast,[20-22] decoration techniques,[23] SEM, and TEM. Only studies utilizing electron microscopical techniques will be discussed in detail here.

(1) Scanning Electron Microscopy (SEM)

Hooton and Merz[18] discovered that ferroelectric BaTiO₃ single crystals show a differential etch rate when etched in hydrochloric acid.

During the etching process, the positive ends of the domain etch at the highest rate, whereas the negative ends etch at the slowest rate. The etch rate of domains where the polarization vector is parallel to the surface is intermediate. The difference in etch rates gives rise to topographical contrast which can be used to identify the domain configurations.[19]

(2) Transmission Electron Microscopy (TEM)

Transmission electron microscopy has been used by several groups to study ferroelectric domain structures in BaTiO₃.[24-31]
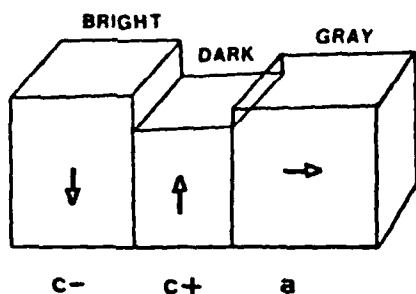
Fig. 2. Topographical contrast caused by differential etch rates.

(A) *Selected-Area Diffraction (SAD):* Diffraction patterns were obtained by placing the SA aperature over individual domain walls for specific grain orientations.

(B) *Microdiffraction Kikuchi Line Measurement:* By focusing the electron beam to a fine spot size ($<0.1 \mu m^2$), we obtained microdiffraction patterns from individual domains. Because of the convergent nature of the beam, and the small volume of material sampled, a clearly defined Kikuchi line pattern was readily obtained.[36] Great care was taken to ensure that no specimen drift took place during the recording of the diffraction patterns.

III. Results and Discussion

Similar features were observed in the domain structures of both the Ca-doped and Nb-doped $BaTiO_3$; thus the results from these samples will be discussed together.

(1) SEM of Conventional 90° and 180° Domain Boundaries

It can be seen from Fig. 2 that in the SEM $c-$ domains will appear bright, $c+$ domains will appear dark, and a domains will appear gray. The different types of domain are, therefore, clearly discernible from the etched microstructure. In Fig. 3(a), a region of a sample is shown encircled. The significant point about this region is that the observed domain boundaries intersect each other at either 45° or 90°; thus it can be deduced that this grain has been sectioned parallel to a cube (100) plane. Given this fact, it is possible to assign polarization vectors to each domain, and obtain a domain configuration fully consistent with the SEM image as shown in Fig. 3(b). Note that although there is no topographical contrast at 90° a-a and 180° a-a boundaries (shown as dotted lines), their presence can be inferred from the nature of the surrounding domains. Also all of the domain boundary lines in this region are straight; some consist of 180° domain walls, some are all 90°, and others consist of alternating 90° and 180° segments. What is clear and should be learned from this figure is that straight domain boundaries do not always qualify as 90° domain boundaries as has been suggested in the past.[39]

Another possible method for determining the grain orientation is electron channeling. Although this technique was not used in this study, it can be noted that channeling would be more suited to the Ca-doped material, because of its larger grain size.

(2) TEM of Conventional 90° Domain Boundaries

To carry out identification of the domains in the TEM, it is necessary to tilt the grain to a (100) orientation. By comparing the observed SAD patterns with those predicted by superimposing the diffraction patterns of the individual domains, boundary identification can be carried out. Before we present our results however, it is worthwhile discussing a point raised earlier, i.e., that the extent of spot splitting is affected by the foil orientation. The reason for this can be seen from Fig. 4. If the beam direction does not lie exactly on the [100] zone axis, the Ewald sphere is effectively tilted about the 000 transmitted spot so that the spot separation changes from δ to δ'. In order to ensure the correct interpretation of the SADP's obtained in this study (especially
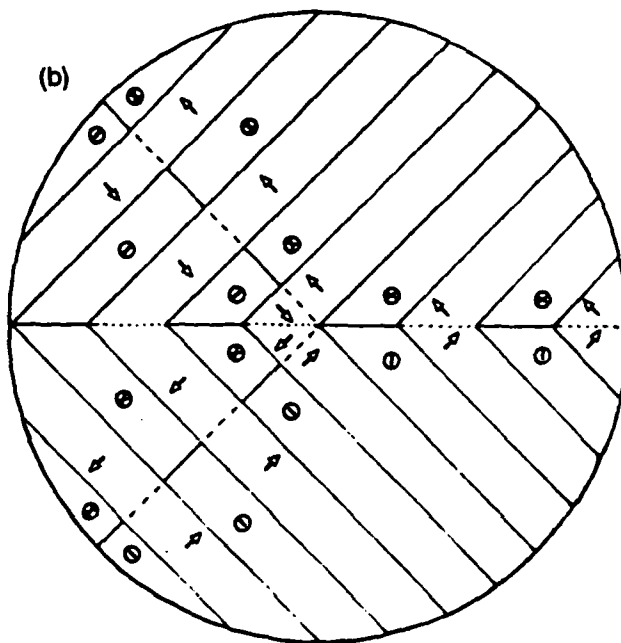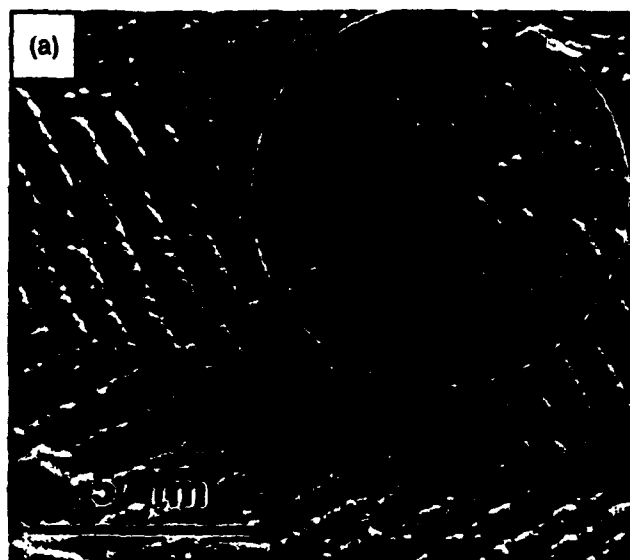
Fig. 3. (a) SEM micrograph of etched microstructure showing topographical contrast at domain boundaries. The encircled region shows an area of the specimen where the surface is parallel to (100) plane. (b) Domain configuration consistent with Fig. 3(a).

with regard to the distinction between conventional and unconventional 90° domain boundaries), it was necessary to determine quantitatively the extent of this effect. The maximum value of ϕ (the angle of tilt) for the [100] spot pattern to be still clearly visible is $\approx 15°$. The value of δ/δ' is given by $\cos \phi$, hence

$$\delta/\delta' = 0.96 \quad \text{for } \phi_{max}$$

This analysis predicts therefore that the extent of spot splitting does not change significantly with orientation. Tilting away from the zone axis is however advantageous, as it enables the higher orders of reflection (which show greater splitting) to be observed.

The procedure for domain boundary analysis by SAD is illustrated in Fig. 5. Figure 5(a) is the bright-field (BF) image of the domain arrangement, and Fig. 5(b) shows a schematic sketch of the postulated conventional 90° domain structure viewed parallel to the beam direction. Note that because of the tetragonality of the unit cell, a slight rotation (0.57°) of the lattice planes occurs at the
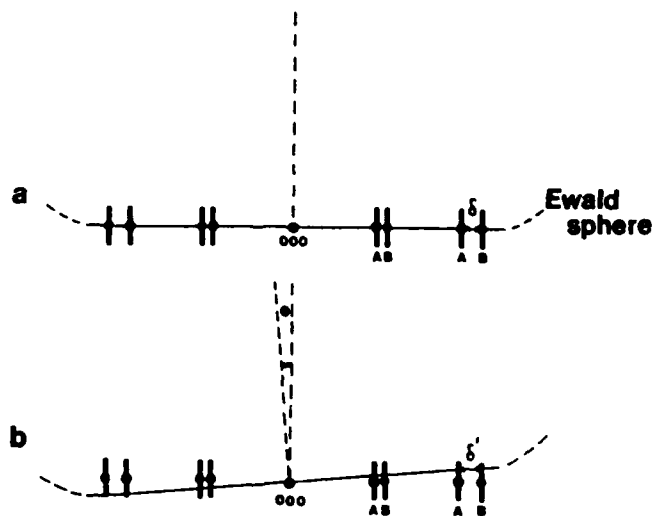
Fig. 4. Effect of specimen tilt on diffraction spot separation: (a) on zone, spot separation δ; (b) tilted by angle ϕ, spot separation δ'.

boundary. The axis of rotation is the [100] (viewing direction). Figure 5(c) is the corresponding diffraction pattern net; the degree of tetragonality and angle of rotation have been exaggerated for clarity. It can be seen that the most pronounced spot splitting is predicted to occur for the (0kk) reflections lying along the diagonal *OP*, and that the direction of the splitting is approximately perpendicular to this. A comparison with Fig. 5(d) shows that this is what was observed. It was also determined that the trace of the boundary was parallel to the [011] direction, thus providing additional confirmation that the boundary was a conventional 90° *a-a* domain wall.

Figure 6 shows the corresponding analysis for a conventional 90° *a-c* boundary. Note that this boundary is geometrically identical with the conventional 90° *a-a* boundary, except viewed from a different direction. Fringe contrast is observed because the boundary is inclined at 45° to the plane of the foil. For this type of boundary the line of intersection of the boundary with the foil surface lies along the [010] direction. Also the direction of spot splitting is along the cube axis [001]₄, and this is seen clearly in Fig. 6(d).

Kikuchi pattern analysis was also used to determine the domain boundary nature. Figure 7 shows a set of Kikuchi patterns obtained
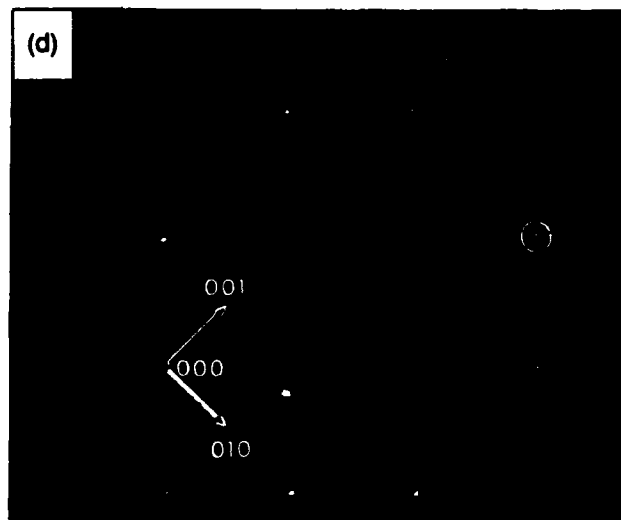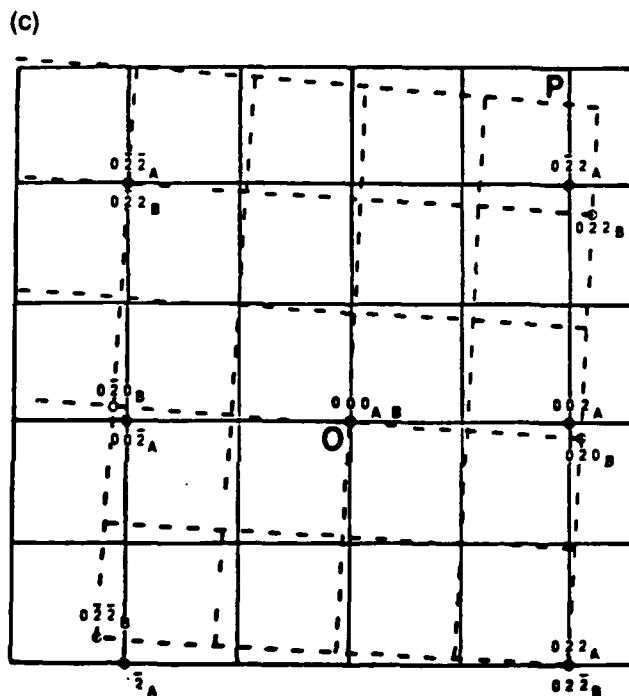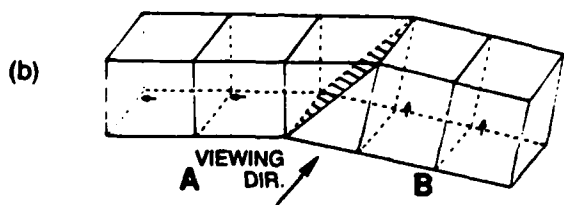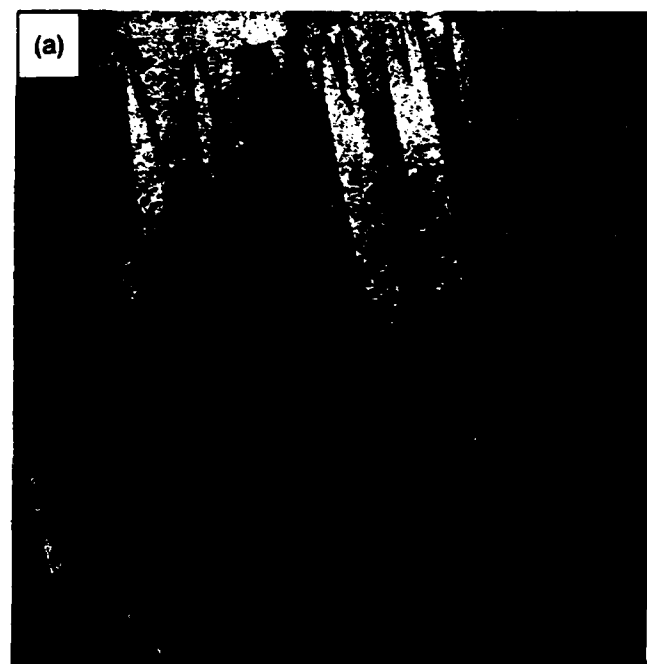

Fig. 5. 90° *a-a* domain boundaries: (a) TEM BF image (Ca-doped), (b) schematic representation of domain boundary, (c) [100] diffraction pattern net, (d) [100] SADP.
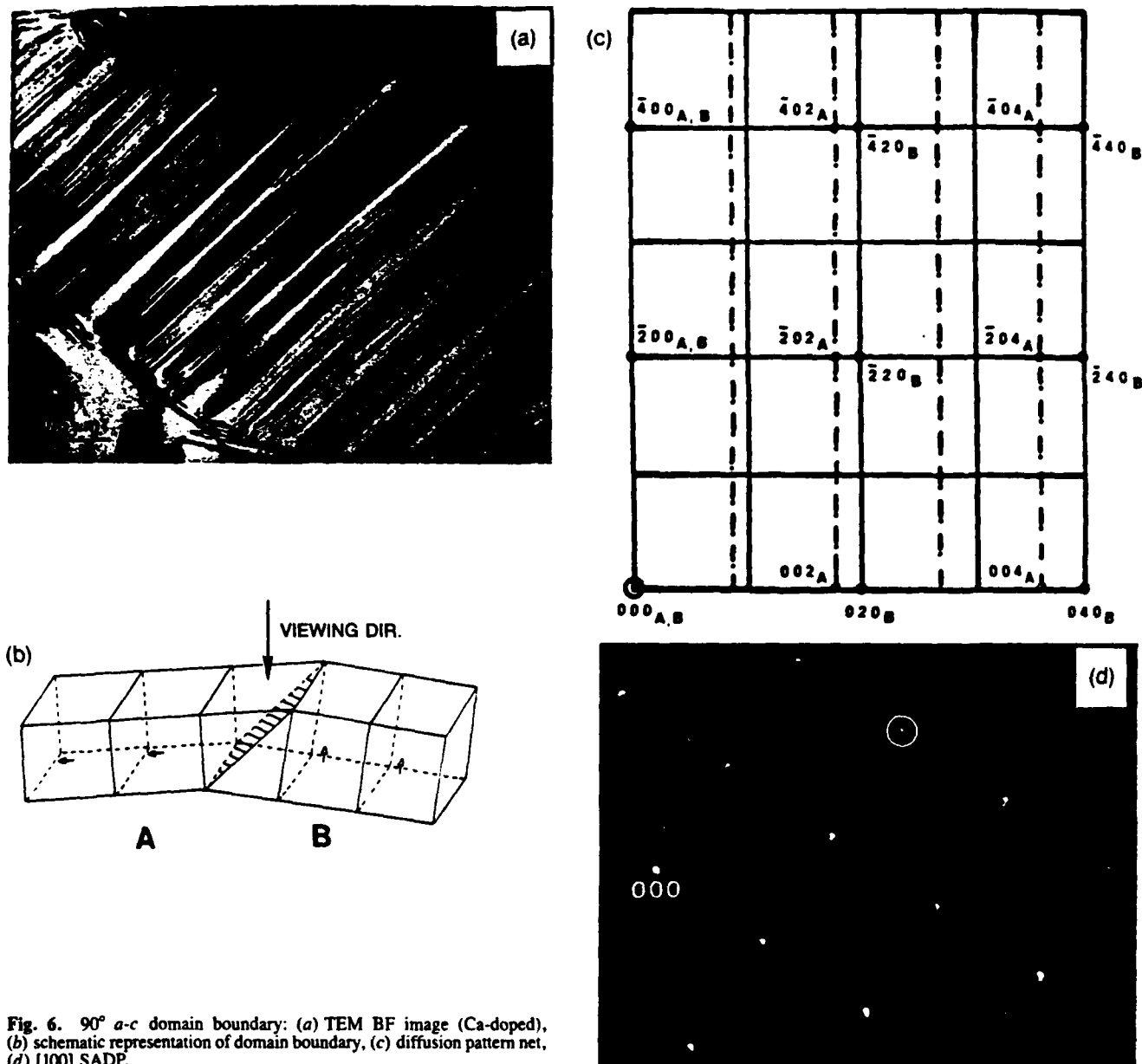
Fig. 6. 90° *a-c* domain boundary: (*a*) TEM BF image (Ca-doped), (*b*) schematic representation of domain boundary, (*c*) diffusion pattern net, (*d*) [100] SADP.

from domains on either side of a conventional 90° *a-a* wall. The Kikuchi line separation is directly related to the lattice spacing and, unlike the separation of diffraction spots, is not sensitive to any deviation from the exact Bragg condition. For this reason, the relative magnitudes of the (001) and (010) lattice parameters for the two domains were readily determined. Comparing the lattice spacings of corresponding parallel planes for the two domains it was found that

$$d_{(001)A} > d_B$$

and

$$d_{(010)A} < d_B$$

as expected for a conventional 90° *a-a* boundary.

(3) SEM and TEM of Unconventional 90° Domain Boundaries

In the course of this study, SEM and TEM evidence was obtained for an unconventional 90° domain boundary. This new type of boundary was observed in both the Nb-doped and Ca-doped samples. The first indications of the possibility of a new domain

configuration came from the SEM results shown in Fig. 8(*a*). This figure is of interest because not only does it show the new type of boundary (region *A*), but also region *B* can be interpreted as the area of intersection of two orthogonal, 90° *a-a* domain colonies. It is thought that the domain contrast in area *B* is due to slight preferential etching of the *a-a* boundaries. One feasible representation of the domain structure in *A* is shown in Fig. 8(*b*); the unconventional boundary is shown as the fine dashed line. The new domain configuration is postulated to be as shown in Fig. 9(*a*). Comparison with Fig. 5(*b*) will confirm that this proposed arrangement is geometrically different from the conventional 90° boundary. In order to obtain conclusive evidence for the existence of this new type of boundary, detailed TEM analysis was carried out on a large number of domain structures.

The predicted diffraction pattern for this boundary when viewed edge-on along a cube axis direction is shown in Fig. 9(*b*). The important difference between this net and Fig. 5(*c*) is that the extent of splitting for reflections along the two cube axis directions is different; i.e., the diffraction pattern is not symmetrical about the [$\bar{1}$10] direction. Careful examination of Fig. 10(*b*) will show that the observed pattern corresponds to the above predictions, thus
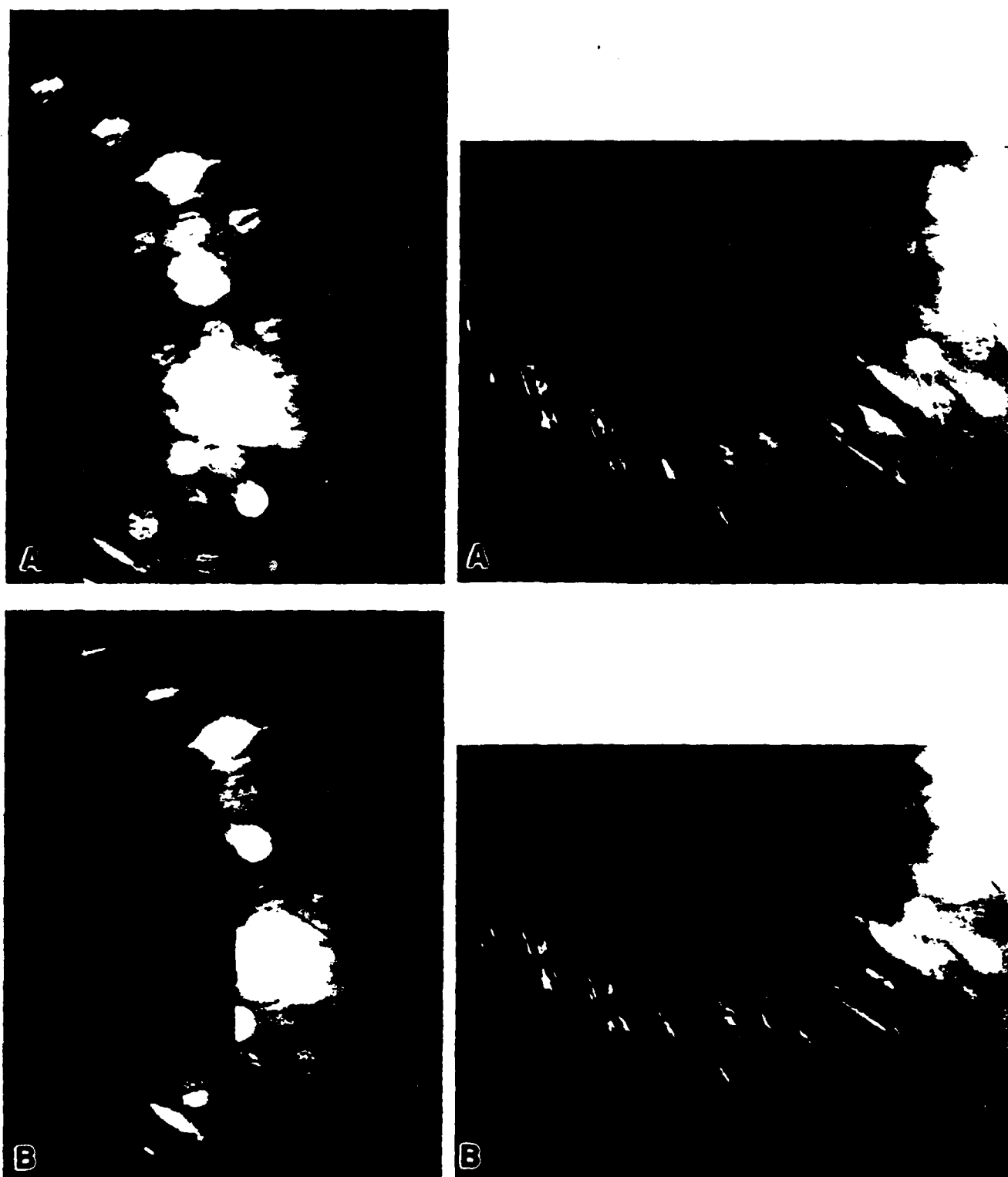
Fig. 7. Kikuchi line patterns from domains *A* and *B* on either side of a 90° *a-a* boundary.

proving that the domains shown in Fig. 10(*a*) are of the new type. It should be noted that although Fig. 10(*b*) is not a zone axis diffraction pattern, the angle of tilt about both cube axes is equal; thus any effect of tilt on the spot separation (however slight) would be the same. Kikuchi line measurements showed that for one set of cube planes the lattice spacings were the same in both domains, but for the orthogonal set, the lattice spacings were different. This is consistent with the proposed configuration of the new boundary and provides additional evidence for its existence. Note that it was also determined that the trace of the boundary was parallel to the (110) direction; thus it cannot be argued that we have been mistakenly studying a 90° *a-c* boundary (which would show similar Kikuchi pattern characteristics). A further example of an unconventional 90° domain structure is given in Fig. 11. It is interesting to note the transition from the unconventional boundary to the conventional 90° *a-c* wall.
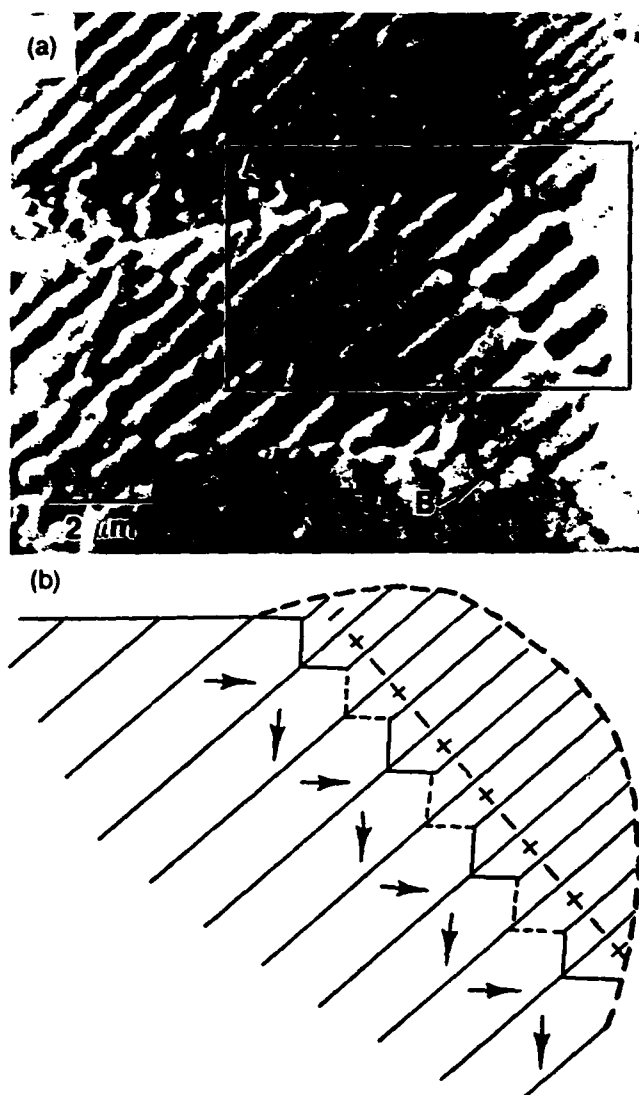
Fig. 9. (*a*) Schematic representation of new domain boundary. (*b*) Diffraction pattern net.

Fig. 8. (*a*) SEM micrograph: (*A*) unconventional domain configuration. (*B*) region of intersection of two orthogonal 90° *a-a* domain colonies. (*b*) Postulated domain structure in *A*.
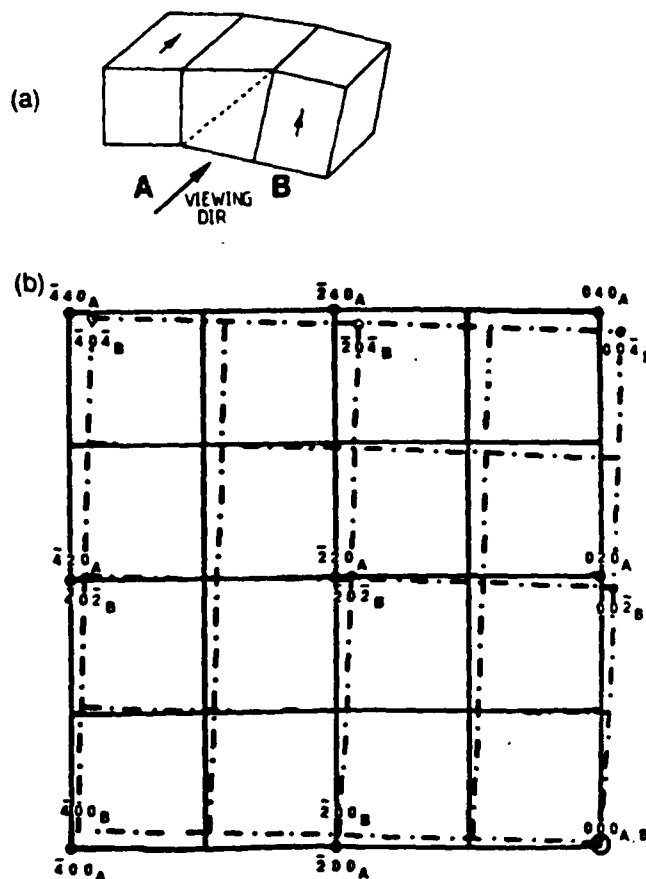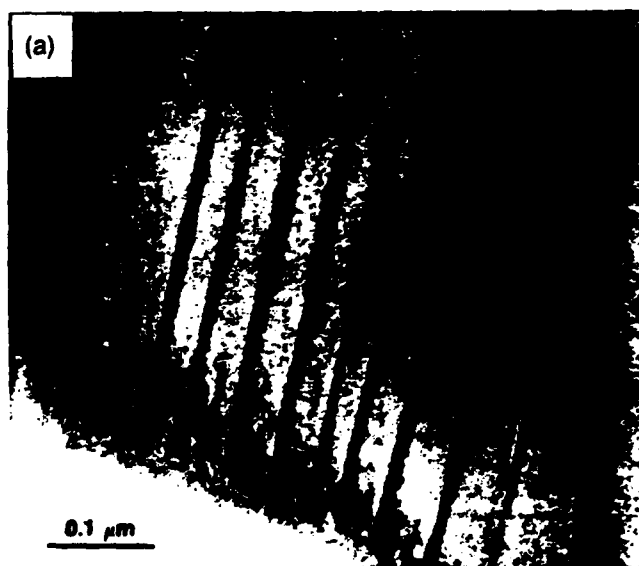

Fig. 10. (*a*) TEM BF micrograph of unconventional domain structure (Ca-doped). (*b*) Corresponding |100| SADP. Note difference in extent of spot splitting for reflections marked *P* and *Q*.

Fig. 11. (a) TEM BF micrograph of unconventional domain structure (Nb-doped). (b) Proposed domain configuration. *AB*: Conventional *a-c* boundary. *BC*: Unconventional boundary.
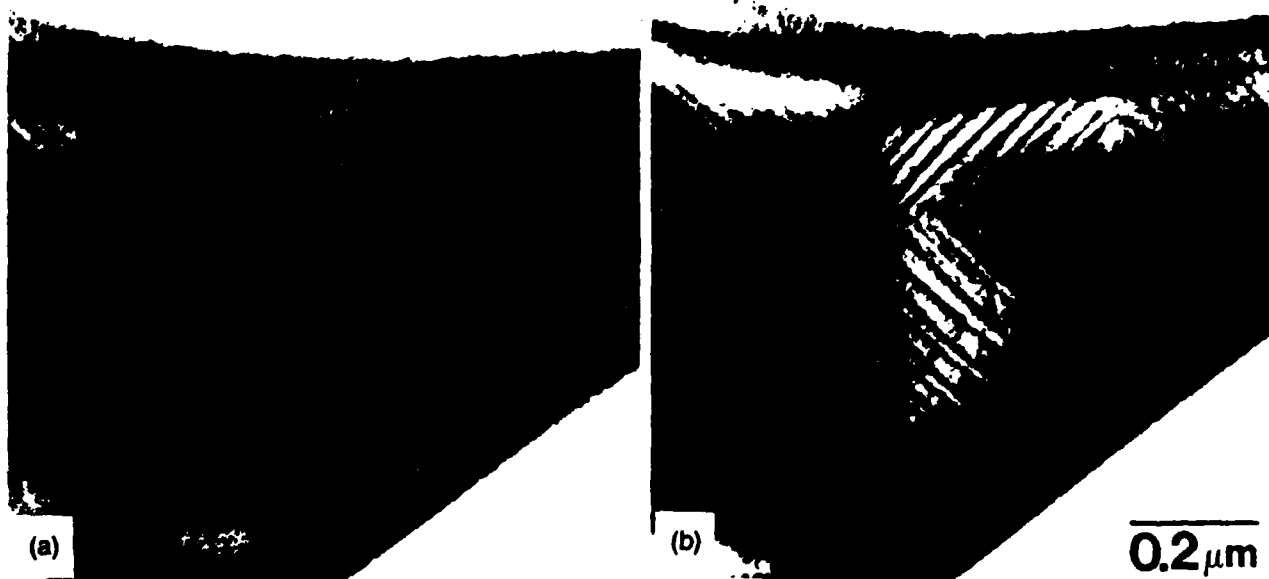

Fig. 12. (a) Region containing unconventional domain configuration. (b) The same region after a short period of time—the new domains are the conventional type.

The reasons for the existence of this new type of domain wall are not well understood, particularly as there are several factors which would seem to strongly favor the formation of conventional 90° boundaries. Firstly, the unconventional boundary will have a higher energy than a conventional domain wall because of the greater degree of distortion; thus the conventional domain structure would presumably be more stable. This conclusion is supported by the following observation. Figure 12(a) shows a region of the specimen containing the new domain structure. After a short period of time had elapsed however, conventional domains (as determined by SAD) were observed to nucleate and grow in place of the new domains. Another factor which points to a relatively higher value for the unconventional boundary energy is the fact that because of the nature of the domain configuration, there must be a net charge at the boundary (see Fig. 13). Despite these arguments, strong evidence has been obtained for the existence of these domains.
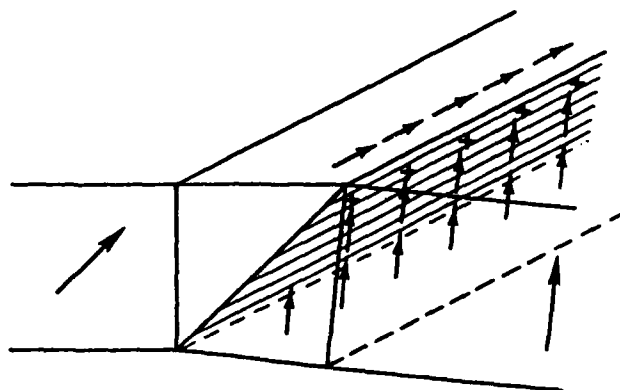

Fig. 13. Diagram showing net positive charge at unconventional boundary surface (all other charges cancel because of head-to-tail arrangement).

Why then do they form? One explanation is that this type of domain configuration occurs in regions where its formation compensates for existing, complex stresses. Thus the existence of new domains would be favored in small-grained, polycrystalline material (such as the samples studied), as here, very complicated stresses can develop below the Curie temperature because of the constrictions of surrounding grains. Another reason which helps to explain the presence of the unconventional boundaries is the reduced distortion at the boundary due to the dopant concentration. It has been found that the addition of Ca[37] and Nb[38] has the effect of lowering the c/a ratio in $BaTiO_3$; thus the boundary energy may be reduced. Clearly further work is necessary to fully understand the nature of this unconventional domain boundary. Future study will explore more fully the role of factors such as dopant type and concentration and grain size on the incidence of these new domains.

IV. Summary

This study has shown that unambiguous identification of domain structures can be carried out using the SEM and TEM. Evidence was obtained for the existence of an unconventional 90° domain configuration which has not previously been reported.

References

[1]K. W. Plessner, "Ageing of the Dielectric Properties of Barium Titanate Ceramics," *Proc. Phys. Soc., London*, **69**, 1261–68 (1956).
[2]Z. Pajak and J. Stankowskie, "Polarization Changes During the Process of Aging in Ferroelectrics of the BaTiO₃-type," *Proc. Phys. Soc., London*, **72**, 1144–46 (1958).
[3]J. Stankowska and J. Stankowski, "Ageing Process in Triglycine Sulphate," *Proc. Phys. Soc., London*, **75**, 455–56 (1960).
[4]S. Ikegami and I. Ueda, "Mechanism of Ageing in Polycrystalline BaTiO₃," *J. Phys. Soc. Jpn.*, **22**, 725–34 (1967).
[5]W. P. Mason, "Ageing of the Properties of Barium Titanate and Related Ferroelectric Ceramics," *J. Acoust. Soc. Am.*, **27**, 73–85 (1955).
[6]L. E. Cross, "Dielectric, Piezoelectric, and Ferroelectric Components," *Am. Ceram. Soc. Bull.*, **63** [4] 586–90 (1984).
[7]H. F. Kay and P. Vousden, "Symmetry Changes in Barium Titanate at Low Temperatures and Their Relation to Its Ferroelectric Properties," *Philos. Mag.*, **40**, 1019–39 (1949).
[8]H. D. Megaw, "Temperature Changes in the Crystal Structure of Barium Titanium Oxide," *Proc. Phys. Soc., London, Sect. A*, **A189**, 261–83 (1947).
[9]H. D. Megaw, "Refinement of the Structure of BaTiO₃ and Other Ferroelectrics," *Acta Crystallogr.*, **15**, 972–73 (1962).
[10]J. P. Remeika, "A Method for Growing Barium Titanate Single Crystals," *J. Am. Chem. Soc.*, **76**, 940–41 (1954).
[11]R. C. Bradt and G. S. Ansell, "Aging in Tetragonal Ferroelectric Barium Titanate," *J. Am. Ceram. Soc.*, **52** [4] 192–99 (1969).
[12]B. Matthias and A. von Hippel, "Domain Structure and Dielectric Response of Barium Titanate Single Crystals," *Phys. Rev.*, **73**, 1378–84 (1948).

[13]R. C. DeVries and J. E. Burke, "Microstructure of Barium Titanate Ceramics," *J. Am. Ceram. Soc.*, **40** [6] 200–206 (1957).
[14]E. A. Little, "Dynamic Behavior of Domain Walls in Barium Titanate," *Phys. Rev.*, **158**, 478–84 (1955).
[15]H. Blattner, W. Kanzig, W. Merz, and H. Sutter, "The Domain Structure of BaTiO₃ Crystals," *Helv. Phys. Acta*, **21**, 207–209 (1948).
[16]B. Matthias and A. von Hippel, "Structure, Electrical, and Optical Properties of Barium Titanate," *Phys. Rev.*, **73**, 268–69 (1948).
[17]W. J. Merz, "Domain Properties in Barium Titanate," *Phys. Rev.*, **88**, 421–22 (1952).
[18]J. A. Hooton and W. J. Merz, "Etch Patterns and Ferroelectric Domains in BaTiO₃ Single Crystals," *Phys. Rev.*, **98**, 409–13 (1955).
[19]G. Y. Robinson and R. M. White, "Scanning Electron Microscopy of Ferroelectric Domains in Barium Titanate," *Appl. Phys. Lett.*, **10**, 320–23 (1967).
[20]K. N. Maffitt, "Interpretation of Electron-Mirror Micrographs of Ferroelectric and Dielectric Surfaces," *J. Appl. Phys.*, **39**, 3878–82 (1968).
[21]V. V. Aristov, L. S. Kokhanchik, K. P. Meyer, and H. Blumtritt, "Scanning Electron Microscopic Investigations of Peculiarities of the BaTiO₃ Ferroelectric Domain Contrast," *Phys. Status Solidi A*, **78A**, 229–36 (1983).
[22]R. LeBihan, J. L. Chartier, and L. Jean, "Measurement of Surface Potential Between Ferroelectric Domains with a Quantitative Electron Mirror Microscope," *Ferroelectrics*, **17**, 429–31 (1977).
[23]A. Sawada and R. Abe, "New Decoration Techniques for Revealing Antiparallel 180° Domains in BaTiO₃," *Jpn. J. Appl. Phys.*, **5**, 401–404 (1966).
[24]M. Tanaka and G. Honjo, "Electron Optical Studies of Barium Titanate Single Crystal Films," *J. Phys. Soc. Jpn.*, **19**, 954–70 (1964).
[25]M. Tanaka, M. Kitamuran, and G. Honjo, "Electron Optical Studies of Barium Titanate Single Crystal Films," *J. Phys. Soc. Jpn.*, **17**, 1197–98 (1962).
[26]V. V. Shakmanov and G. V. Spivak, "A Microdiffraction Investigation of the Domain Structure in Barium Titanate Films," *Sov. Phys.—Solid State (Engl. Transl.)*, **10**, 802–806 (1968).
[27]T. Malis and H. Gleiter, "Investigation of the Structure of Ferroelectric Domain Boundaries by Transmission Electron Microscopy," *J. Appl. Phys.*, **47**, 5195–200 (1976).
[28]H. Blank and S. Amelinckx, "Direct Observation of Ferroelectric Domains in Barium Titanate," *Appl. Phys. Lett.*, **2**, 140–42 (1963).
[29]R. Gevers, P. Delavignette, H. Blank, J. Van Landuyt, and S. Amelinckx, "Electron Microscope Transmission Images of Coherent Domain Boundaries II Observations," *Phys. Status Solidi*, **5**, 595–633 (1964).
[30]G. Remaut, R. Gevers, and S. Amelinckx, "Wavy Fringes at Domain Boundaries in Barium Titanate Observed in the Electron Microscope," *Phys. Status Solidi*, **20**, 613–21 (1967).
[31]M. D. Dennis, "Transmission Electron Microscopy of Ferroelectric Domains in Barium Titanate"; Ph.D. Thesis. The Pennsylvania State University, University Park, PA, 1972.
[32]R. Gevers, P. Delavignette, H. Blank, and S. Amelinckx, "Electron Microscope Transmission Images of Coherent Domain Boundaries," *Phys. Status Solidi*, **4**, 383–410 (1964).
[33]G. Remaut, R. Gevers, A. Lagasse, and S. Amelinckx, "Dynamical Theory of the Images of Microtwins as Observed in the Electron Microscope III Observations and Results of Numerical Calculations," *Phys. Status Solidi*, **13**, 125–40 (1966).
[34]R. Gevers, H. Blank, and S. Amelinckx, "Extension of the Howie-Whelan Equations for Electron Diffraction to Non-Centro Symmetrical Crystals," *Phys. Status Solidi*, **13**, 449–65 (1966).
[35]N. H. Chan, R. K. Sharma, and D. M. Smyth, "Nonstoichiometry in SrTiO₃," *J. Electrochem. Soc.*, **128**, 1762–69 (1981).
[36]D. B. Williams, "Practical Analytical Electron Microscopy in Materials Science"; p. 126. Philips Electron Optics Publishing. Mahwah, NJ, 1984.
[37]T. Mitsui and W. B. Westphal, "Dielectric and X-ray Studies of Ca,Ba TiO₃ and Ca,Sr₁₋ₓTiO₃," *Phys. Rev.*, **124**, 1354–59 (1961).
[38]W. R. Buessem and M. Kahn, "Effects of Grain Growth on the Distribution of Nb in BaTiO₃ Ceramics," *J. Am. Ceram. Soc.*, **54** [9] 458–61 (1971).
[39]B. Jaffe, W. R. Cook, and H. Jaffe, "Piezoelectric Ceramics"; pp. 64–71. Academic Press, New York, 1971.

THE EFFECT OF OCTAHEDRALLY-COORDINATED CALCIUM
ON THE FERROELECTRIC TRANSITION OF BaTiO$_3$

Z.Q. Zhuang, M.P. Harmer and D.M. Smyth
Materials Research Center
Lehigh University
Bethlehem, PA 18015

R.E. Newnham
Materials Research Laboratory
The Pennsylvania State University
University Park, PA 16802

ABSTRACT

The effect of the B-site calcium ion on the ferroelectric
transition of BaTiO$_3$ ceramics was investigated by X-ray dif-
fraction, TEM, SEM, and by measurements of dielectric properties
and equilibrium electric conductivity. It was found that the
c/a ratio at room temperature decreases continuously to near unity
with increasing amount of Ca ion on the B site up to 5%, and that
the broadened and diffused Curie peak moves to room temperature for
the composition with 5% of Ca ion on the B site and 6% on the A
site. A thermodynamic model has been developed to explain this
effect.

MATERIALS INDEX: ferroelectrics, barium, titanates

Introduction

Several previous investigations have been carried out on the structure
and dielectric properties of Ca-doped barium titanate. In 1952, Berlincourt
and Kulesar (1) found that Ca addition to BaTiO$_3$ caused only negligible
changes in the Curie point. Two years later, McQuarrie and Behnke (2)
reported that Ca-doped BaTiO$_3$ showed a slight decrease of the Curie point.
In 1961 Mitsui and Westphal (3) through the dielectric and X-ray studies of
Ba$_{1-x}$Ca$_x$TiO$_3$ demonstrated that the Curie point of Ba$_{1-x}$Ca$_x$TiO$_3$ increases from
130.7°C for pure BaTiO$_3$ up to 136.1°C for x=0.08 and then decreases slightly
for continuously increasing Ca concentration up to 25%. A similar statement
on the Ca-doped BaTiO$_3$ appears in the book by Jaffe, Cook and Jaffe (4).
Wakino, Minai and Sakabe (5) have investigated Ca-doped BaTiO$_3$ multilayer
ceramic capacitors for use with base metal electrodes, which can be sintered
in a reducing atmosphere.

The present investigation centers on the dielectric properties, defect
chemistry, and microstructure of acceptor-doped barium titanate. Micro-
structure examination was carried out to elucidate the ferroelectric behavior,
together with a 4-point DC technique for the measurement of the equilibrium
electric conductivity, and the measurement of dielectric properties. It is

speculated that the broadened Curie peak shifting effect is caused by the
lattice distortion caused by replacing Ti with the larger Ca ion, acting in
the same manner as a hydrostatic pressure (6).

Experimental Procedure

Samples were prepared by the liquid mixing technique which is a modifica-
tion of the process developed by Pechini (7). The starting chemicals were
titanium tetra-isoproxide, barium carbonate, and calcium carbonate. After
polymerization with the addition of citric acid, and calcination at 900°C for
5 hours, the calcined powder was ground, cold pressed into pellets, and
sintered in air in an electric furnace, to form dense ceramic samples of
$Ba_{1-x}Ti_{1-y}Ca_{x+y}O_{3-y}$ with x ranging from 0-6% and y from 0-5%. Dielectric
measurements were carried out on circular disks 0.04 cm thick and 1 cm in
diameter. Sputtered gold or platinum electrodes were employed. An automated
capacitance bridge was used in the determination of dielectric constant.
X-ray diffraction analysis was carried out on a Philips APD3600 Automated X-ray
Powder Diffractometer with CuKa radiation, using crushed powder from freshly
sintered ceramic disks. Lattice parameters were determined using the $400a_1$
and $00\text{-}a_1$ diffraction peaks. Electrical conductivity measurements were
performed using a 4-point DC technique described elsewhere (8). For SEM
examination, the specimens were thermally etched at 1000°C to 1200°C for 30
minutes. For TEM examination, the specimens were thinned on an Argon Ionic
Thinner until a specimen with a thickness of about 1000 Å was obtained .

Results and Discussion

Figure 1 shows the changes in Curie point of barium titanate ceramics of
composition $Ba_{1-x}Ti_{1-y}Ca_{x+y}O_{3-y}$ with x (0-5%) and y (0-5%). It can be seen
that the transition temperature T_c depends on the concentration of Ca on the
B site and that T_c is 126.7°C for pure barium titanate. T_c lies near room
temperature for ceramics containing 6% Ca on the A site and 5% Ca on the B
site. The change of Curie point with the concentration of Ca on the B site,
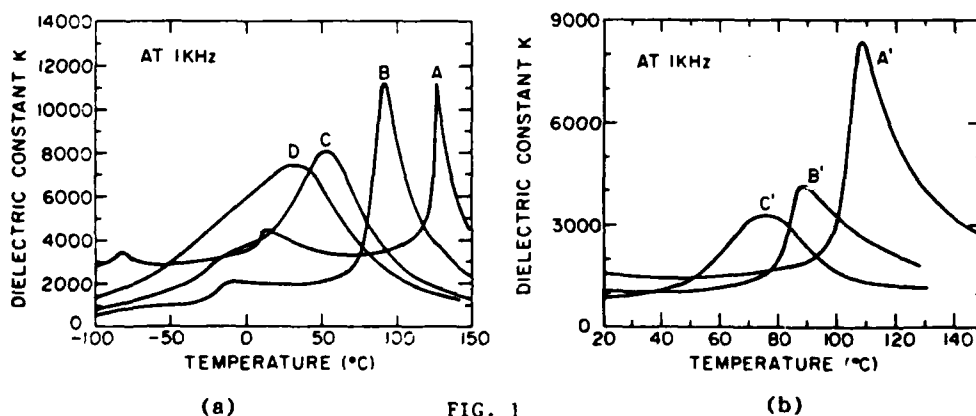

| (a) | FIG. 1 | (b) |

The temperature dependence of dielectric constant K of barium titanate
ceramics with compositions of (a) $Ba_{0.95}Ti_{1-x}Ca_{0.05+x}O_{3-x}$: (A) pure,
(B) x=0.01, (C) x=0.02 and (D) x=0.04: and of (b): (A') $BaTi_{0.99}Ca_{0.01}O_{2.99}$,
(B') $BaTi_{0.98}Ca_{0.02}O_{2.98}$ and (C') $BaTi_{0.97}Ca_{0.03}O_{2.97}$. All measured at
1000Hz.

and also on both the A and B sites, is shown schematically in Figure 2.

Based on high angle X-ray diffraction patterns, values of c, a, c/a and the unit cell volume of Ba$_{0.95}$Ti$_{1-x}$Ca$_{0.05+x}$O$_{3-x}$ ceramics in the tetragonal phase of room temperature are presented in Table 1. From Table 1, we conclude that the c/a ratio decreases with increasing amount of Ca on the B site; the tetragonality at room temperature approaches a cubic unit cell for the composition Ba$_{0.94}$Ti$_{0.95}$Ca$_{0.11}$O$_{2.95}$. We interpret these results as an internal lattice distortion of the materials, caused by the substitution of Ca for Ti (Fig. 3). In Figure 3, the arrows indicate the directions of the internal stresses p.
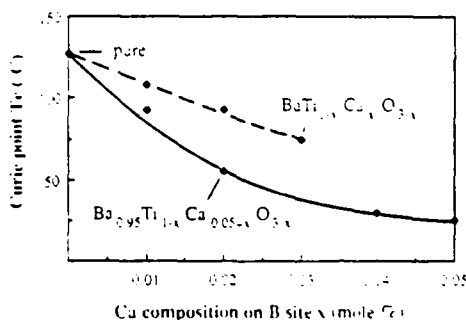

FIG. 2

The lowering of Curie point T$_c$ with the concentration of Ca ion (on the B site and on both the A site and the B site).
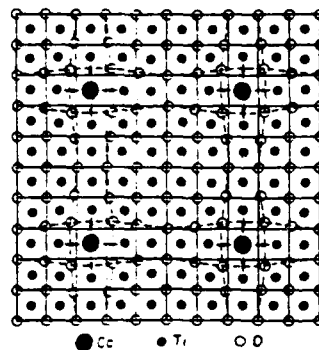

FIG. 3

A two dimensional view of the structure of Ca-doped BaTiO$_3$, showing the localized expansion of the unit cell caused by the substitution of Ca for Ti in the octahedral sites of the perovskite structure.

TABLE 1

Lattice Parameters of Ba$_{0.95}$Ti$_{1-x}$Ca$_{0.05+x}$O$_{3-x}$ Ceramics at Room Temperature

	undoped	x				
		0	0.01	0.02	0.03	0.04
c (Å)	4.0400	4.0356	4.0270	4.0192	4.012	4.012
a (Å)	3.9964	3.9904	3.9980	4.0056	-----	-----
c/a	1.0109	1.0113	1.0073	1.0030	-----	-----
V (Å^3)	64.52	64.16	64.368	64.487	-----	64.58

Additional evidence comes from changes in domain configurations with Ca concentration on the B site (Fig. 4). Domains can easily be seen in pure barium titanate, and in Ca-A-site-doped barium titanate ceramics (Fig. 4(a) and (b)). But it is very difficult to examine the domain structure under TEM in heavily-doped barium titanate ceramics (Fig. 4(e) and (f)), because of the c/a ratio decreasing with the increasing of Ca concentration on the B site.
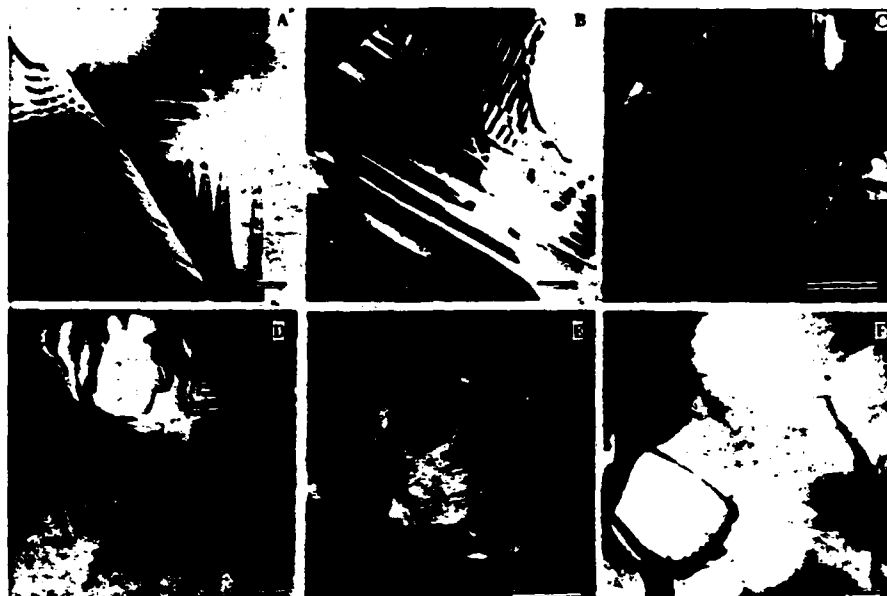
FIG. 4

The variation of the domain configuration of Ca-doped barium titanate ceramics with the increase of the concentration of Ca on the B sites: (a) pure, (b) $Ba_{0.95}Ca_{0.05}TiO_3$, (c) $Ba_{0.95}Ti_{0.98}Ca_{0.07}O_{2.98}$, (d) $Ba_{0.95}Ti_{0.97}Ca_{0.08}O_{2.97}$, (e) and (f) $Ba_{0.95}Ti_{0.96}Ca_{0.09}O_{2.96}$. In the pure and slightly doped ceramics, the domains can be easily seen because of their larger size. With increasing Ca concentration on the B site, the domains become vanishingly small. The observed domain sizes vary from 0.3 μm to 0.06 μm. The scale bar is 0.5 μm in every picture.

Measurement of the equilibrium electric conductivity demonstrated acceptor-doped behavior in Ca-B-site-doped barium titanate ceramics (Fig. 5). In the case of Ca substitution for Ba and Ti ions, the reaction is

$$2CaO \longrightarrow Ca_{Ba} + Ca_{Ti}'' + 2O_o + V_o^{\cdot\cdot} \tag{1}$$
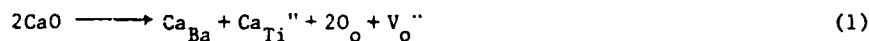
in which a Ca ion substitution for a Ti ion creates an oxygen vacancy $V_o^{\cdot\cdot}$. At the minimum of the equilibrium electric conductivity curve,

$$[V_o^{\cdot\cdot}] = [Ca_{Ti}''] \gg n \text{ and } p \tag{2}$$

When combined with the oxidation and reduction reactions, we have

$$d \log Po_2^o / d \log [Ca_{Ti}''] = -2 \tag{3}$$

where, Po_2^o stands for the oxygen pressure at the minimum in equilibrium electric conductivity. It is obvious from equation (3) that the position of the minimum should move two orders of magnitude toward lower oxygen pressure for each order of increase in the content of Ca on the B site. Figure 5 shows qualitative agreement with this prediction. In other words, the shift in
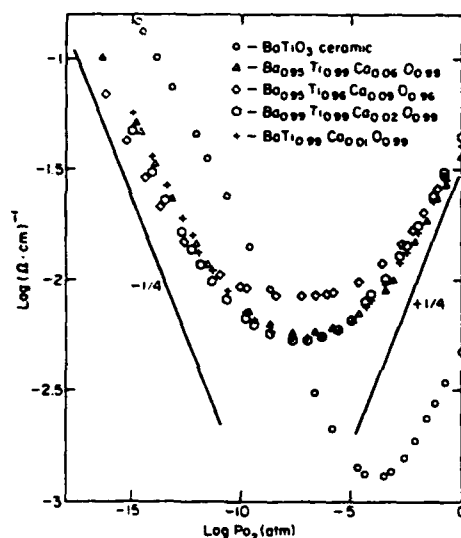
FIG. 5

Equilibrium electric conductivity of 1000°C of barium
titanate ceramics undoped and Ca-doped.

position of the minima toward lower oxygen pressure indicates the occupancy
of Ca on the B site in the Ca-doped barium titanate ceramics.

According to Goswami and Cross (9), the elastic Gibbs free energy for
barium titanate ceramic can be written in the form

$$G_1 - G_{1o} = A(P_x^2 + P_y^2 + P_z^2) + B(P_x^4 + P_y^4 + P_z^4) + C(P_x^6 + P_y^6 + P_z^6)$$

$$+ D(P_x^2 P_y^2 + P_y^2 P_z^2 + P_z^2 P_x^2) + G(P_x^2 P_y^4$$

$$+ P_x^4 P_y^2 + P_y^2 P_z^4 + P_y^4 P_z^2 + P_z^2 P_x^4 + P_z^4 P_x^2)$$

$$- 1/2\, s_{11}(X_x^2 + Y_y^2 + Z_z^2) - s_{12}(X_x Y_y + Y_y Z_z + Z_z X_x)$$

$$- 1/2\, s_{44}(X_y^2 + Y_z^2 + Z_x^2) + (Q_{11} X_x + Q_{12} Y_y + Q_{12} Z_z)P_x^2$$

$$+ (Q_{12} X_x + Q_{11} Y_y + Q_{12} Z_z)P_y^2 + (Q_{12} X_x + Q_{12} Y_y$$

$$+ Q_{11} Z_z)P_z^2 + Q_{44}(X_y P_x P_y + Y_z P_y P_z + Z_x P_z P_x) \tag{4}$$

where, X_x, Y_y, Z_z are the normal stress components.

X_y, Y_z, Z_x the shear stress components.

S_{11}, S_{12}, S_{44} the elastic compliance constants.

P_x, P_y, P_z the components of polarization.

Q_{11}, Q_{12}, Q_{44} the electrostrictive coefficients.

A, B, C, D, G the coefficients of the free energy function and G_{lo} the free energy of the unstressed, unpoled state.

For hydrostatic stress $-p$ (N/m^2)

$$X_x = Y_y = Z_z = -p$$

$$Y_z = X_y = Z_x = 0$$

The Curie Weiss law in the paraelectric phase under stress can be written as

$$K = C/(T - T_\theta) \tag{5}$$

where, $T_\theta = \{T_o - 2\varepsilon_o p (Q_{11} + 2Q_{12})_o C_o\} / \{1 + 2\varepsilon_o \alpha \, p (Q_{11} + 2Q_{12})_o C_o\}$ (6)

In this expression, $Q_{11} + 2Q_{12})_o$ is the value of the electrostrictive coefficients at zero temperature, C_o and T_o the unstressed Curie Weiss constant and Curie Weiss temperature, T_θ the ferroelectric Curie Weiss temperature in the stressed state. Therefore, we can consider the transition temperature under stress to be a function of stress p and proportional to it. It is obvious from eq. (6) that the transition temperature decreases linearly with the increase of hydrostatic stress p.

As mentioned in the previous section, the Ca occupancy of B site causes a distortion of the unit cell and a model of the distorted lattice is shown in Figure 3. As shown in Figure 3, it could be seen that the unit cell in which a Ca ion occupies the B site expands and exerts a compressive stress p on the adjacent unit cells which are compressed. The former can be treated as a tension source. Therefore, the Curie temperature of Ca-B-site-doped barium titanate ceramics will decrease with concentration of Ca on B site due to the internal stress, as described by eq. 6. And from Figure 1 and Figure 2, it is obvious that the lowering of the transition temperature for a given change in the Ca composition (0-5%) on the B site was more pronounced when there was Ca (about 5%) on the A site. When there are Ca ions on A sites more Ca ions occupy B sites and the lattice distorts more easily.

It is clear from Figure 3 that the compression of the unit cells along the tension directions is not uniform. This leads to a stress distribution along the tension direction causing the Curie peak to broaden over a range of temperatures, from T_{cm} to T_{cn}, as shown in Figure 1.

Acknowledgement

References

1. D.A. Berlincourt and F. Kulesar, J. Acoust. Soc. Am., 24, 709 (1952).

2. M.C. McQuarrie and F.W. Behnke, J. Am. Ceram. Soc., 37, 539 (1954).

3. T. Mitsui and W.B. Westphal, Phys. Rev., 124, 1354 (1961).

4. B. Jaffe, W.R. Cook and H. Jaffe, Piezoelectric Ceramics, p. 91. Academic Press, NY (1971).

5. K. Wakino, K. Minai and Y. Sakabe, High-Dielectric Constant Ceramics for Base Metal Monolithic Capacitors. Murata Manufacturing Co., Ltd., Japan.

6. W.J. Merz, Phys. Rev., 77, 52 (1950).

7. M. Pechini, U.S. Pat., 3,330,697 (1967).

8. N.-H. Chan, R.K. Sharma and D.M. Smyth, J. Am. Ceram. Soc., 65, 167 (1982).

9. A.K. Goswami and L.E. Cross, Phys. Rev., 171, 549 (1968).

Section III

SECOND PHASE DISTRIBUTION IN RELAXOR FERROELECTRICS

Effect of Powder Purity and Second Phases on the Dielectric

Properties of Lead Magnesium Niobate Ceramics

Jie Chen, Andrew Gorton, Helen M. Chan[*] and Martin P. Harmer[*+]

Department of Materials Science and Engineering

and the Materials Research Center, Lehigh University,

Bethlehem, Pennsylvania, USA.

ABSTRACT

The dielectric properties of PMN ceramics have been studied as a function of powder purity and microstructure. Starting powder purity was shown to have a pronounced effect on the resultant dielectric properties. Values of K_{max} as high as 20,000 were obtained using starting powders of exceptionally high purity (99.999%), despite the formation of a pyrochlore phase. The pyrochlore phase formed as large isolated grains in the microstructure. It was found to be a cubic type pyrochlore with a composition of $Pb_2Nb_{1.75}Mg_{0.25}O_{6.62}$. Much lower dielectric constants were obtained with samples of lower reagent grade purity. This was partially explained by the presence of an intergranular second phase. Other factors such as lattice impurities and grain boundary chemistry were also argued to be important.

[*] Member, American Ceramic Society

[+] Presented at the Annual Meeting of the American Ceramic Society, Chicago, April 28, 1986, paper number 12-E-86.

Chen 6/6/

1. Introduction

Lead magnesium niobate $Pb(Mg_{1/3}Nb_{2/3})O_3$ (herein after referred to as PMN) is an important relaxor ferroelectric material with a high dielectric constant and a high electrostrictive strain coefficient (1). The dielectric properties of polycrystalline PMN are, however, strongly influenced by ceramic processing conditions, particularly by the order in which the single oxide components are combined during calcining (2,3). Improper processing results in the formation of a pyrochlore type second phase and lower values of the dielectric constant. Steps that can be taken in order to minimize the amount of pyrochlore phase formed include (a) prereacting two of the single oxide components (either Nb_2O_5 + MgO to form $MgNb_2O_6$ or PbO + Nb_2O_5 to form $Pb_3Nb_2O_8$) during the calcination step (3,4) (b) adding excess MgO (3,4,5) and (c) using excess PbO and an optimum sintering cycle (2). In this paper we report on the further benefits to be gained from using ultra high purity starting powders. We have observed that processing with ultra high purity powders produces PMN ceramics with highly superior dielectric properties, even when a pyrochlore second phase was found to be present. A comparison of the dielectric properties of ultra high and lower grade purity was made. The effect of the pyrochlore phase and other secondary phases on the dielectric properties of PMN are discussed.

2. Experimental

Reagent grade[a] and ultra high purity grade[b] starting powders of PbO, Nb_2O_5 and MgO were processed into PMN ceramics using the precalcine procedure developed by Swartz et. al. (3). The MgO and Nb_2O_5 were mixed by ball milling in acetone for 24 hours followed by drying and calcining in a covered alumina crucible at 1000°C for 2 hours (hours and 5). The calcined product, $MgNb_2O_6$, was then ball milled with 3PbO and subsequently calcined at 850°C for 2 hours and 5 hours for

1

the high and low purity samples, respectively, to form PMN. One weight % of
PVA binder was added to the powders which were then pressed and sintered at
1200°C and 1100°C for the (low) and (high) purity samples, respectively, for 2
hours inside covered alumina boats. The samples were buried in powder of the
same composition to minimize material loss during firing. Compositions so
prepared were stiochiometric PMN of ultra high purity (PMN-U), stoichiometric
PMN of lower reagent grade purity (PMN-A) and reagent grade PMN containing 2
mole% excess MgO (PMN-B). Polished sections were examined by scanning electron
microscopy and by wavelength dispersive spectroscopy (WDS) in an electron
microprobe[c]. Thin foil specimens for transmission electron microscopy were
prepared by ion-beam milling and examined in an electron microscope[d] equipped
with an energy-dispersive X-ray analyzer. Powders and discs were examined
using a powder diffractometer[e] operating at 45kV, 30mA and 0.01°/s scan rate
with CuKα radiation. Samples for dielectric measurements were prepared from
sintered pellets by polishing the faces flat and parallel and by firing on
silver electrodes at 500°C. Dielectric measurements were carried out on an
automated system, whereby a temperature-control system[f] and an LCR meter[g] were
controlled by a desk-top computer[h]. Dielectric constant and dissipation
factors were measured to within ±5% pseudocontinuously at various frequencies
between 100 Hz and 100 KHz. A minimum of two samples were measured for each
composition. Density measurements were made by the archimedes method.

3. Results

The sintered grain size and density for each composition (PMN-U, PMN-A
and PMN-B) was found to be similar ($\approx$ 2μm matrix grain size and $\approx$ 97-98%
theoretical density). Large ($\leq$ 10 μm) angular grains of a second phase were
observed in polished sections of sintered samples and in the calcined starting

powders. The greatest amount of second phase was observed in sample PMN-A. X-ray mapping showed that the large second phase grains were rich in niobium and deficient in magnesium (figure 1). The precise chemical composition of the particles was determined by WDS using the microprobe standard ZAF correction technique (6). Pure Pb, Nb and Mg were used as standards and the matrix phase (PMN) was also analyzed to provide a final correction factor in the calibration. More than twenty grains were analyzed to obtain good statistics. The composition of the second phase was determined to be

$Pb_{2.00\pm0.10}(Mg_{0.25\pm0.01}Nb_{1.75\pm0.10})O_{6.62\pm0.36}$ in each material.

A bright field TEM image of a second phase particle in PMN-A is shown in figure 2 along with its' selected area diffraction (SAD) pattern. The SAD pattern indexed as a $[1\bar{2}\bar{3}]$ zone axis orientation for a cubic pyrochlore phase having a space group Fd3m with a lattice parameter of $\approx$ 1.06nm (7). A fraction of the grain boundaries ($\approx$10-20% in PMN-A and PMN-B ~~and < 10% in PMN-C~~) were observed to also contain a continuous grain boundary phase $\approx$2-5nm in width as shown in figure 3. The intergranular phase was scattered in patches throughout the microstructure, the majority of the grain boundaries looking clean. STEM analysis of the intergranular phase in PMN-A indicated that it was rich in lead and contained a significant amount of phosphorus impurity. The magnesia-rich composition (PMN-B) was also found to contain a small number of small ($\leq$ 0.1μm) precipitates mostly at the triple points and also within the grains. These precipitates were found to be rich in magnesia and contained significant amounts of alumina and phosphorus.

X-ray diffraction was used to determine the amount of pyrochlore phase present in each sample from the relative intensities of the (222) pyrochlore peak I_{pyro} and the (110) perovskite PMN peak I_{PMN} using the formula:

$$\% \text{ pyrochlore} = \frac{I_{pyro}}{I_{pyro} + I_{PMN}} \times 100 \qquad (1)$$

From this it was determined that PMN-U, PMN-A and PMN-B contained 3%, 5% and 1% pyrochlore phase, respectively.

The dielectric properties of PMN-U, PMN-A and PMN-B are shown in figure 4. The peak in the dielectric constant measured at 100 Hz was, on average, 19,000 for PMN-U, 13,000 for PMN-B and 7,000 for PMN-A. The peak temperatures were -12°C for PMN-U and -20°C for PMN-A and PMN-B.

4. Discussion

The most interesting finding in the present study was that powder purity has a very pronounced effect on the dielectric constant of PMN. The maximum value for the dielectric constant that we obtained for the ultra high purity PMN ($\approx$ 20,000 at 100Hz, figure 4a) is believed to be the highest figure ever reported for polycrystalline PMN, falling close to the maximum obtainable single crystal value. It is also interesting to note that the high purity PMN-U had high K values despite the presence (3%) of a pyrochlore phase. Pyrochlore has previously been considered to be very detrimental to the dielectric properties of PMN ceramics. The lower purity PMN-B material studied here, however, contained less (1%) pyrochlore than PMN-U, yet it had a much lower dielectric constant (13,000). This implies that the pyrochlore phase is not, directly at least, all that detrimental to the dielectric constant. The pyrochlore was observed to be distributed as an isolated second phase in all samples studied. Under these conditions it would not be expected to have a very significant effect on the dielectric constant. Its effect on the dielectric properties can be predicted using a mixture rule developed by Wiener for a diphasic solid containing an isolated spheroidal minor phase of much lower

4

dielectric constant (8):

$$\bar{K} = \frac{2 \; K_{PMN} \; (1-V_{PYR})}{(2 + V_{PYR})} \qquad (2)$$

Here $\bar{K}$ is the dielectric constant of the mixture, K_{PMN} is the dielectric constant of pure PMN (taken to be 20,000) and V_{PYR} is the volume fraction of pyrochlore phase. Figure 5 shows the dielectric constant of the mixture plotted as a function of the percent pyrochlore present. The dielectric constants of PMN-U, PMN-A and PMN-B are superimposed on the figure showing that PMN-U fits the model well whereas PMN-A and PMN-B do not. The figure demonstrates that, as expected, a few percent pyrochlore phase has only a minimal effect on the dielectric constant. This was verified by the results we obtained for the high purity sample PMN-U. Something other than the pyrochlore phase itself, therefore, must be causing the lower purity samples PMN-A and PMN-B to have such relatively low dielectric constants. One possible explanation is that intergranular phases are responsible. To investigate this further we have calculated the dielectric constant as a function of grain boundary phase thickness using two mixture models. The first is a simple series model given by (8):

$$\frac{1}{\bar{K}} = \frac{V_{PMN}}{K_{PMN}} + \frac{V_{gb}}{K_{gb}} \qquad (3)$$

The second is a logarithmic mixture model given by (8):

$$\log \bar{K} = V_{PMN} \log K_{PMN} + V_{gb} \log K_{gb} \qquad (4)$$

The grain boundary thickness was calculated for a 2μm grain size material

assuming cubic grains and a uniformly distributed intergranular phase with a dielectric constant (K_{gb}) of 150 and 20. Figure 6 shows the predicted variation in dielectric constant with film thickness for each model. The figure demonstrates the potentionally strong influence that low dielectric constant intergranular phases can have on the dielectric constant of PMN ceramics. The series model provides an extreme indication of the influence of the intergranular phase, while the logarithmic rule probably gives a more realistic estimate. Taking the series model and the lower estimate for the dielectric constant of the intergranular phase $(K_{gb}=20)$, a uniform grain boundary thickness of 5nm would be required in order to give the low K value (7,000) observed for PMN-A. We did observe an intergranular phase in PMN-A that was 5nm thick in places, however, it was only found in isolated regions of the sample (on $\approx$ 10-20% of the total grain boundary area) and, therefore, this does not satisfactorily account for the low K value we observed. Even assuming that the apparantly clean grain boundaries did in fact contain a very thin intergranular phase (1-2nm), undetected by TEM, the amount of second phase involved would still be insufficient. We believe, therefore, that there must be at least one other important factor involved, such as a change in stoichiometry or impurity content near the grain boundary causing the dielectric constant to be reduced. The effect of lattice impurities on the dielectric constant of PMN is also a factor that warrants further consideration. Further systematic work is clearly needed in order to separate out the relative contributions of the various possible mechanisms.

4. Conclusions

The purity of the starting powders used to prepare PMN ceramics has a pronounced effect on the resultant dielectric properties. Values of K_{max} as

high as 20,000 were obtained using starting powders of exceptionally high purity, despite the formation of a pyrochlore phase. The pyrochlore phase formed as large isolated grains in the microstructure. It was found to be cubic with a composition of $Pb_2Nb_{1.75}Mg_{0.25}O_{6.62}$. The lower dielectric constants obtained with samples of lower reagent grade purity could be partially explained by the presence of an intergranular second phase. Other factors such as lattice impurities may also be important.

References

1. Kenji Uchino. " Electrostrictive Actuators: Materials and Applications." Bull. Am. Ceram. Soc., 65, [4], 647-652 (1986)

2. Martine Lejeune and J.P.Boilot. " Optimization of Dielectric Properties of Lead-Magnesium Niobate Ceramics. " Bull. Am. Ceram. Soc., 65, [4], 679-82 (1986)

3. S.L.Swartz, T.R.Shrout, W.A.Schulze and L.E.Cross. "Dielectric Properties of Lead-Magnesium Niobate Ceramics". J. Am. Ceram. Soc., 67, [5], 311-15 (1984).

4. J.P.Guha. Comment on "Dielectric Properties of Lead-Magnesium Niobate Ceramics." J. Am. Ceram. Soc., 68, [3], c-86-C-87 (1985)

5. S.L.Swartz, T.R.Shrout, W.A.Schulze and L.E.Cross. Reply to above J. Am.

7

Ceram. Soc., 68, [3], C-87-88 (1985)

6. J.I.Goldstein et.al., Scanning Electron Microscopy and X-Ray Microanalysis; Ch.7. Plenum Press, New York (1981).

7. T.R.Shrout and S.L.Swartz. "Dielectric Properties of Pyrochlore Lead Magnesium Niobate" Mat. Res. Bull., 18, 663-667, (1983).

8. D.A.Payne and L.E.Cross. "Microstructure-Property Relations for Dielectric Ceramics: I. Mixing of Isotropic Homogeneous Linear Dielectrics", pp. 584-597 in Ceramic Microstructures '76, Edited by R. M. Fulrath and J. A. Park, Westview Press, Colorado (1977).

Superscripts

a   Hammond Lead Products Inc. IN grade 1004 PbO (99.9%),
Fisher reagent grade MgO (98.95%), Fansteel, Chicago
IL, Nb_2O_5 (99.5%)

b   JMC Puratronic MgO (99.999%), PbO (99.9999%) and Nb_2O_5
(99.9999%)

c   733 Superprobe, JEOL U.S.A. Inc., Medford, MA

d   400T, Philips Electronic Instruments, Inc., Mount Vernon,
N.Y.

e   ADP 3600, Philips Electronic Instruments

f   Model 2300, Delta Design Inc., San Diego, CA

g   Model 4274 LCR Meter, Hewlett-Packard Inc., Palo Alto, CA

h   Model 9000-216, Hewlett-Packard Inc.

Figure Captions

Figure 1. Large pyrochlore grains in PMN-A (a) backscattered electron image showing the pyrochlore grains in dark contrast (b) magnesium x-ray map (c) niobium x-ray map.

Figure 2 (a) Bright field transmission electron image of a pyrochlore grain in PMN-A, (b) selected area diffraction pattern of grain in (a); it indexes as a cubic pyrochlore phase in a [$1\bar{2}\bar{3}$] zone orientation.

Figure 3. Bright field transmission electron micrograph of PMN-A showing a non typical region containing an intergranular phase.

Figure 4 (a) Dielectric constant and dissipation factor as a function of temperature and frequency for PMN-U (highest values) (b) dielectric constant and dissipation factor at 1 KHz fo PMN-U, PMN-A and PMN-B (average values).

Figure 5. Dielectric constant as a function of percent pyrochlore phase calculated by Wiener mixing theory (appropriate for an isolated spheroidal second phase with a much lower dielectric constant than the host.)

Figure 6. Dielectric constant as a function of grain boundary phase thickness for series mixing and log mixing.
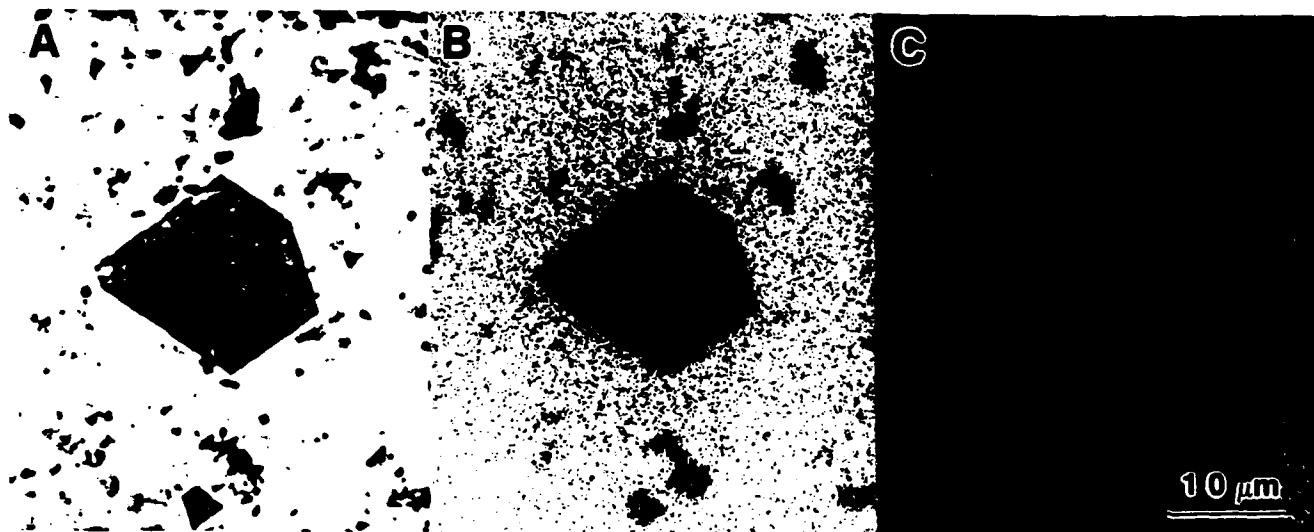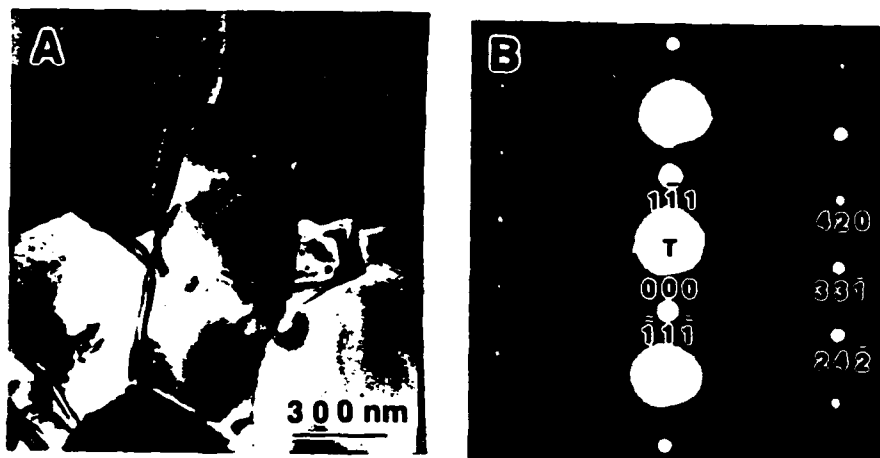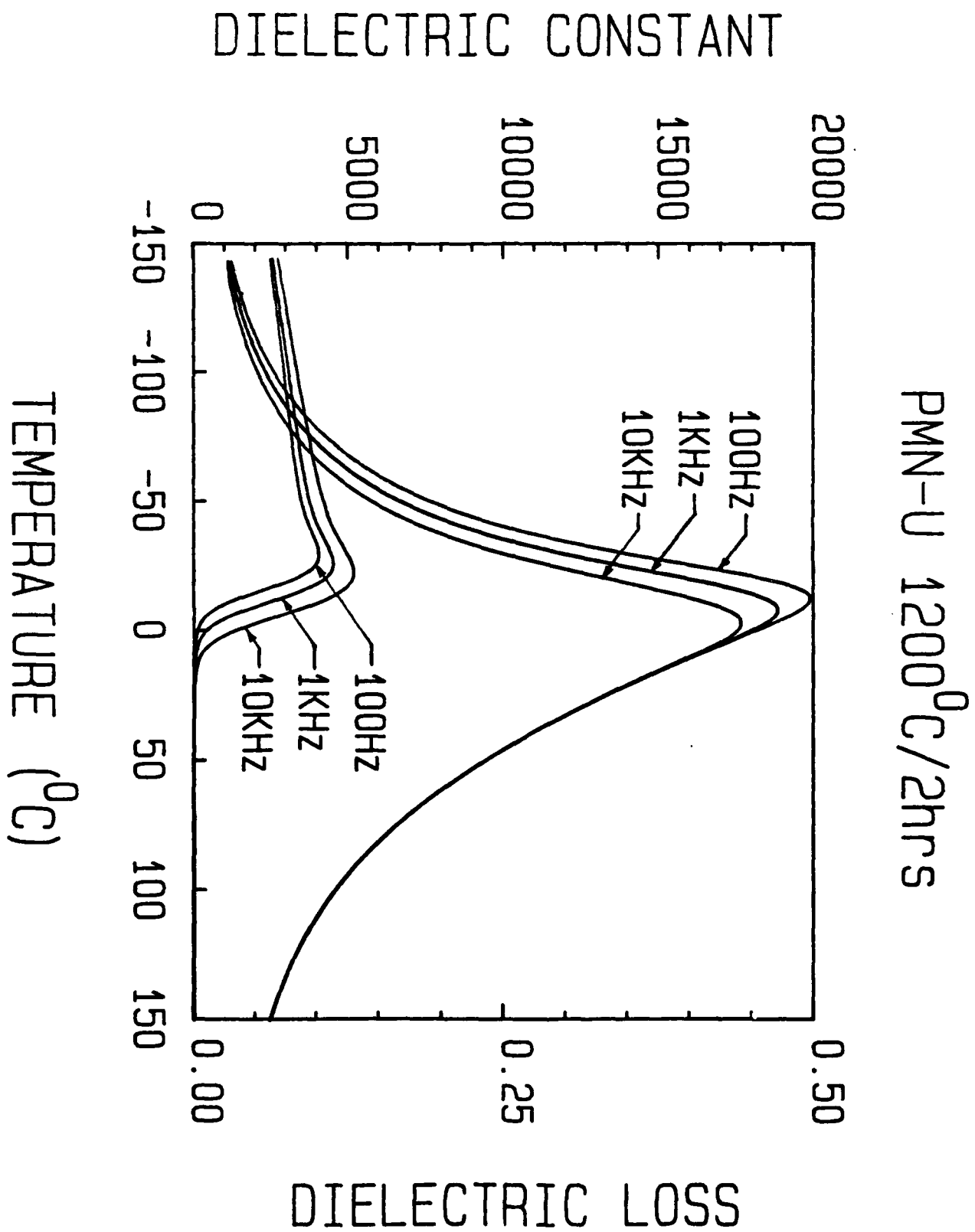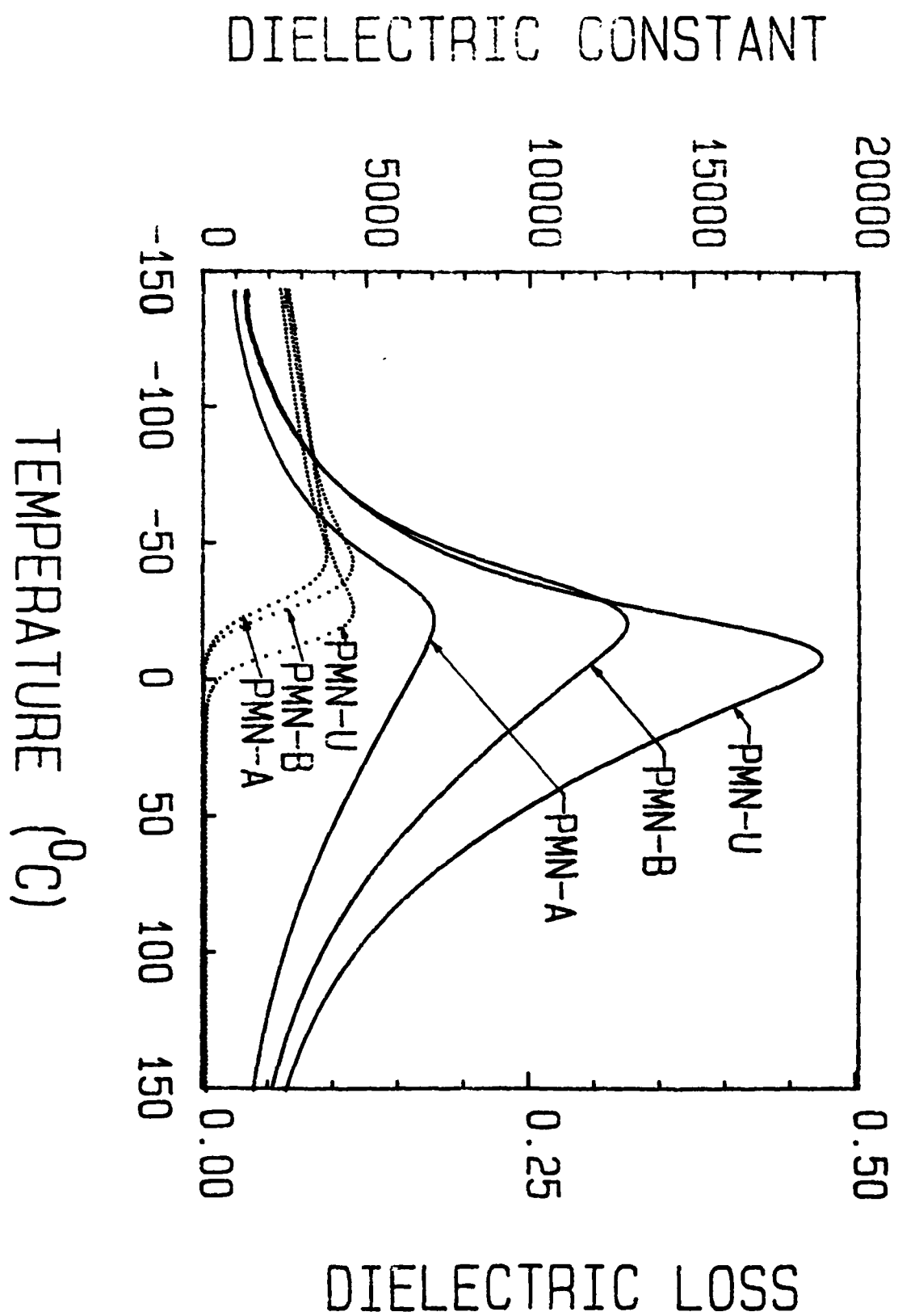
Fig 1

Fig 2

Fig 3

10 µm

A

B

C

A

B

300 nm

$1\bar{1}1$

T

000

$\bar{1}1\bar{1}$

420

331

202

100 nm

11

Fig 4a

DIELECTRIC CONSTANT

DIELECTRIC LOSS

TEMPERATURE (°C)

PMN-U 1200°C/2hrs

12

Fig 46

13

Fig 5

Fig 6